



THE HONG KONG  
POLYTECHNIC UNIVERSITY

香港理工大學

Pao Yue-kong Library

包玉剛圖書館

---

## Copyright Undertaking

This thesis is protected by copyright, with all rights reserved.

**By reading and using the thesis, the reader understands and agrees to the following terms:**

1. The reader will abide by the rules and legal ordinances governing copyright regarding the use of the thesis.
2. The reader will use the thesis for the purpose of research or private study only and not for distribution or further reproduction or any other purpose.
3. The reader agrees to indemnify and hold the University harmless from and against any loss, damage, cost, liability or expenses arising from copyright infringement or unauthorized usage.

### IMPORTANT

If you have reasons to believe that any materials in this thesis are deemed not suitable to be distributed in this form, or a copyright owner having difficulty with the material being included in our database, please contact [lbsys@polyu.edu.hk](mailto:lbsys@polyu.edu.hk) providing details. The Library will look into your claim and consider taking remedial action upon receipt of the written requests.

QUANTITATIVE MEASUREMENT OF ACIDIC  
ULTRAFINE PARTICLES AND OBSERVATIONS OF  
NEW PARTICLE FORMATION IN THE ATMOSPHERE  
OF HONG KONG

WANG DAWEI

Ph.D

The Hong Kong Polytechnic University

2015

The Hong Kong Polytechnic University  
Department of Civil and Environmental Engineering

**Quantitative Measurement of Acidic Ultrafine Particles  
and Observations of New Particle Formation in the  
Atmosphere of Hong Kong**

WANG DAWEI

A thesis submitted in partial fulfillment of  
the requirements for the degree of  
Doctor of Philosophy

December 2014

## **CERTIFICATE OF ORIGINALITY**

I hereby declare that this thesis is my own work and that, to the best of my knowledge and belief, it reproduces no material previously published or written, nor material that has been accepted for the award of any other degree or diploma, except where due acknowledgement has been made in the text.

\_\_\_\_\_ (Signed)

WANG DAWEI (Name of student)

## ABSTRACT

The number concentration and size-resolved properties of acidic ultrafine particles (AUFPs) have been observed to more closely associate with adverse health effects than do indices of total particulate mass. However, no reliable measurement techniques are currently available to quantify the number concentration and the size distribution of ambient AUFPs. In this study, a method with the use of iron nanofilm detectors for enumeration and size measurement of acid aerosols was developed and refined. An electrostatic precipitator (ESP) was improved and a diffusion sampler (DS) was designed as short-term and long-term collection system respectively with iron nanofilm detectors to measure the number concentration and size distribution of airborne AUFPs. Field campaigns were undertaken in rural and urban environments in Hong Kong to validate the method. Then the number concentration and size distributions of airborne AUFPs were quantified, the formation and growth processes of airborne AUFPs at these two different sites were investigated. The main contents and results are summarized as follows:

(1) A method with the use of iron nanofilm detectors for enumeration and size measurement of acid aerosols was developed and refined. Standard sulfuric acid ( $\text{H}_2\text{SO}_4$ ) or ammonium hydrogen sulfate ( $\text{NH}_4\text{HSO}_4$ ) droplets and sulfuric acid – coated particles were generated and deposited on the detectors causing reaction spots. The dimensions of the reaction spots were examined with Atomic Force Microscopy (AFM) to establish the correlations between the diameter of the particle and the size of the reaction spot. To validate this method, a field measurement was conducted from 06 September to 30 November, 2010 at Mt. Tai Mo Shan, a rural site in Hong Kong. Scanning

mobility particle sizer (SMPS) and electrostatic precipitator (ESP) were utilized as the collection system. A commercially available online measurement system, i.e., SMPS+CPC (condensation particle counter) was simultaneously used in the field measurement. The results indicated that the particle number (PN) concentrations obtained from the AFM scanning of the exposed detectors via SMPS+ESP collection system were comparable to those derived from the SMPS + CPC measurements ( $p > 0.05$ ). The average geometric mean diameter of particles measured by the SMPS + CPC and the detectors scanned by the AFM was  $52.3 \pm 6.9$  nm and  $51.9 \pm 3.1$  nm, respectively, showing good agreement. It is suggested that the iron nanofilm detectors could be a reliable tool for the measurement and analysis of acidic particles in the atmosphere.

(2) Besides the ESP, a diffusion sampler (DS) with iron nanofilm detectors was designed for long-term collection of airborne AUFPs. The developed DS was made of stainless steel with a flat and rectangular channel with 1.0 mm height, 50 mm width and 500 mm length. The iron nanofilm detectors were deployed on rectangular recesses inside the sampler at three different locations along the length of the channel to collect the ultrafine particles. The exposed detectors were then scanned using an AFM to numerate and distinguish the AUFPs from the non-acidic UFPs. Prior to sampling, the semi-empirical equations for the diffusive deposition efficiency of particles at the different detector locations in the sampler were obtained based on theoretical diffusive mechanism and modified by the experimental data. After calibration, the DS + AFM method and SMPS+CPC system were simultaneously used in a one-month field measurement conducted from 22 December 2010 to 20 January

2011 at an urban site. Both methods showed very good agreement in terms of total PN concentration and size. Therefore, it is reasonable to assume that the number concentration and size distribution of acidic particles estimated by the DS+AFM method were reliable.

(3) At the rural site, the potential formation and growth processes of new particles were investigated. New particle formation (NPF) events were found on 12 out of 35 days with the estimated formation rate  $J_{5.5}$  from 0.97 to 10.2  $\text{cm}^{-3} \text{s}^{-1}$ , and the average growth rates from 1.5 to 8.4  $\text{nm h}^{-1}$ . The events usually began at 10:00~11:00 local time characterized by the occurrence of a nucleation mode with a peak diameter of 6~10 nm. Solar radiation, wind speed, sulfur dioxide ( $\text{SO}_2$ ) and ozone ( $\text{O}_3$ ) concentrations were on average higher, whereas temperature, relative humidity and nitrogen oxide ( $\text{NO}_x$ ) concentration were lower on NPF days than on non-NPF days. Back trajectory analysis suggested that in majority of the NPF event days, the air masses originated from the northwest to northeast directions. The observed associations of the estimated formation rate  $J_{5.5}$  and the growth rate  $\text{GR}_{5.5-25}$  with gaseous sulfuric acid and volatile organic compounds (VOCs) suggested the critical roles of sulfuric acid and biogenic VOCs (e.g.,  $\alpha$  - pinene and  $\beta$  - pinene) in the new particle formation.

(4) At the urban site, the potential causes and factors influencing acidic particle number concentrations were investigated. Northeastern monsoon prevailed during the sampling period. Apart from PN peaks appeared in traffic rush hours (i.e., 08:00 - 09:00 and 17:00 - 18:00), a distinct peak of PN concentrations in the afternoon (11:00 - 16:00) was observed during the sampling period. Concurrent measurement data of PSD,  $\text{O}_3$  and SA

concentrations revealed that the afternoon peaks observed were likely due to NPF via photochemical reactions. These NPF events were frequently observed under clean and dry weather in Hong Kong. Besides the NPF events, we also found four nucleation mode particle burst events, typically with increased number concentrations of nucleation mode particles ( $N_{\text{nuc}}$ ) without growth to larger size particles. These burst events were generally accompanied by high-level primary air pollutants, i.e., sulfur dioxide ( $\text{SO}_2$ ), nitrogen oxide ( $\text{NO}_x$ ) and carbon monoxide (CO), low SR and high CS conditions. The very different characteristics of the burst events from those of the NPF events indicated that these nucleation mode particle burst events were not caused by the photochemical reactions, but by the primary emission from the local combustion source(s).

Overall, this study developed a novel method to quantify the number concentration of acidic ultrafine particles in the air, and improved the understanding of the sources and formation of acidic ultrafine particles in the rural and urban environments. These results, besides their scientific values, will have direct implications for the local and regional control efforts for reducing acidic particle pollution.

## **THE NOVELTY OF THIS STUDY**

Although a number of studies indicate the close association between the acidity of ultrafine particles and adverse health effects, no reliable measurement techniques are available so far to obtain the number concentrations of acidic ultrafine particles (AUFPs) due to the fact that determination of number concentration and size distribution of AUFPs is an extremely difficult task. In this study, an iron nanofilm detector method was for the first time developed for the estimation of number concentration and size distribution of acidic particles in ambient air of Hong Kong. This method overcame the limitation of traditional instruments that can only be used to measure the total number concentration of particles in the atmosphere, and was able to distinguish acidic particles from non-acidic ones.

In the above method, the ambient particles were size-selected by differential mobility analyzer (DMA) and deposited onto the nanofilm detectors using an electrostatic precipitator (ESP). The AUFPs deposited on the iron nanofilm detectors, on which reaction spots were formed, were then counted and sized using an atomic force microscope (AFM). However, this method has limitations for the assessment of long-term exposure to AUFPs due to the fact that (1) the detector will be saturated after only several hours of sampling by the ESP, and it will be highly time-consuming if using this approach to assess long-term exposure because numerous short-term samples for AFM analysis are needed; and (2) the cost is high for the operation and maintenance. Hence, another highlight of this study is the development of a relatively inexpensive diffusion sampler (DS) that overcame the above problems and was still

appropriate to the AFM analysis method. This newly-developed DS was verified by field measurement of AUFPs at a rural site and an urban site. The results indicate that the diffusion sampler is effective for the quantification of ambient acidic ultrafine particles.

At last but not least, the number concentrations and size distributions of ambient AUFPs in Hong Kong were for the first time determined due to the development of the nano-film detectors and the diffusion sampler. The potential sources and formation processes of the acidic particles in the study periods were investigated in-depth and well associated with the new particle formation events.

## PUBLICATIONS

1. **Wang, D.W.**, Guo, H.\*, Chan, C.K., Measuring ambient acidic ultrafine particles using iron nanofilm detectors: Method development. *Aerosol Science and Technology*, 46:5, 521-532, 2012.
2. **Wang, D.W.**, Guo, H.\*, Chan, C.K., Diffusion sampler for Measurement of Acidic Ultrafine Particles in the Atmosphere. *Aerosol Science and Technology* 48:12, 1236-1246, 2014.
3. Guo, H.\*, **Wang, D.W.**, Ling, Z.H., Chan, C.K., and Yao, X.H., Observation of aerosol size distribution and new particle formation at a mountain site in subtropical Hong Kong. *Atmospheric Chemistry and Physics* 12, 9923 – 9939, 2012.
4. **Wang, D.W.**, Guo, H.\*, Cheung, K., Gan, F.X., Observation of nucleation mode particle burst and new particle formation events at an urban site in Hong Kong. *Atmospheric Environment* 99, 196-205, 2014.
5. Liu, B., **Wang, D.W.**, Guo, H.\*, Ling, Z.H., Cheung, K., Metallic corrosion in the polluted urban atmosphere of Hong Kong. *Journal of Environmental Monitoring and Assessment* 187:4112, 2015.
6. Guo, H.\*, Ling, Z.H., Cheung, K., **Wang, D.W.**, Simpson, I.J., Blake, D.R., Acetone in the atmosphere of Hong Kong: Abundance, sources and photochemical precursors. *Atmospheric Environment* 65, 80-88, 2012.
7. Guo, H.\*, Ling, Z.H., Cheung, K., Jiang, F., **Wang, D.W.**, Simpson, I.J., Barletta, B., Meinardi, S., Wang, T.J., Wang, X.M., Saunders SM, Blake DR, Characterization of photochemical pollution at different elevations in mountainous areas in Hong Kong. *Atmospheric Chemistry and Physics* 13, 3881 – 3898, 2013.
8. Guo, H.\*, Ling, Z.H., Simpson, I.J., Blake, D.R., **Wang, D.W.**, Observations of isoprene, methacrolein (MAC) and methyl vinyl ketone (MVK) at a mountain site in Hong Kong. *Journal of Geophysical Research - atmospheres*, VOL. 117, D19303, 2012.

## **ACKNOWLEDGEMENTS**

I would like to express my deepest gratitude to my supervisor Dr. GUO Hai for his constant encouragement, guidance, and providing me with an excellent atmosphere for doing research. I appreciate his vast knowledge and skill in many areas, and his assistance in writing thesis.

I must thank my friends, particularly Cheng Hairong, Cheung Kalam, Ling Zhenghao, Liu Bo, Wang Yu, Wang Nan, Ou Jiamin, Huang Yu, Gao Yuan, Nie Wei, Wang Zhe, Xu Likun, Guo Jia, Xu Zheng and Zhou Shenzhen, for their support and care which helped me overcome setbacks and stay focused on my graduate study.

I would also like to thank my family for their support through my entire life and in particular, I must acknowledge my parents. Without their love and encouragement, I would not have finished this thesis.

Finally, This work was supported by the Environment and Conservation Fund (ECF) of the Hong Kong Special Administrative Region (No. 20/2008 and No. 7/2009), the joint scheme of National Natural Science Foundation of China (NSFC) and Research Grant Council (RGC) (N\_PolyU545/09), and the National Natural Science Foundation of China (NSFC) (41275122).

## CONTENTS

CERTIFICATE OF ORIGINALITY .....	I
ABSTRACT .....	II
THE NOVELTY OF THIS STUDY .....	VI
PUBLICATIONS .....	VIII
ACKNOWLEDGEMENTS.....	IX
CONTENTS.....	X
CHAPTER 1: OVERVIEW .....	1
1.1 Introduction .....	1
1.2 Aims and objectives .....	5
1.3 Structure of the thesis.....	7
CHAPTER 2: LITERATURE REVIEW .....	9
2.1 Characteristics of atmospheric ultrafine particles.....	9
2.1.1 Nucleation mode.....	10
2.1.2 Aitken and accumulation modes.....	11
2.2 Effect of acidic UFPs (AUFPs) on human health and environment .....	12
2.2.1 Health effects.....	13
2.2.2 Visibility.....	15
2.2.3 Climate.....	16
2.3 Measurements of number concentrations of UFPs .....	17
2.3.1 Real-time measurements of UFPs .....	17
2.3.2 Real-time measurements of AUFPs.....	21
2.3.3 Off-line measurements of UFPs .....	22
2.3.4 Off-line measurements of AUFPs .....	23
2.4 Formation mechanisms of UFPs in clean and polluted atmospheres .....	25
2.4.1 Remote environment .....	27
2.4.2 Urban environment .....	31
CHAPTER 3: METHODOLOGY .....	35
3.1 Preparation of iron nanofilm detectors.....	36
3.2 Generation of aerosol standards.....	37
3.2.1 Non-acidic particles.....	37
3.2.2 Acidic droplets .....	39
3.2.3 Acid-coated particles .....	40

3.3 Calibration of instruments .....	41
3.3.1 SMPS + CPC calibration .....	41
3.3.2 Collection efficiency of ESP .....	44
3.3.3 Collection efficiency of DS .....	45
3.3.4 AFM calibration .....	49
3.4 Performance tests of detector .....	52
3.4.1 Response to humidity and temperature .....	52
3.4.2 Response to gaseous pollutants .....	52
3.5 Field Measurements .....	53
3.5.1 Sampling sites .....	53
3.5.2 Sampling techniques .....	55
3.5.3 Sampling design .....	61
3.5.4 Quantification and sizing of AUFPS collected on the detectors .....	62
3.5.5 SMPS Data processing and analysis .....	63
<b>CHAPTER 4: DEVELOPMENT OF IRON NANOFILM DETECTORS .....</b>	<b>68</b>
4.1 Introduction .....	68
4.2 Results and discussion .....	69
4.2.1 Calibration of AFM .....	69
4.2.2 Nanofilm Reaction Spots from Deposited Acidic Droplet and Acid-coated Standards .....	71
4.2.3 Detector Response to Humidity, Temperature and Gaseous Pollutants .....	77
4.2.4 Validation in a Field Measurement .....	80
4.3 Summary and conclusions .....	85
<b>CHAPTER 5: DIFFUSION SAMPLER FOR MEASUREMENT OF AUFPS .....</b>	<b>88</b>
5.1 Introduction .....	88
5.2 Results and discussion .....	91
5.2.1 Collection efficiency of DS .....	91
5.2.2 Validation of the diffusion sampler .....	96
5.3 Summary and conclusions .....	104
<b>CHAPTER 6: OBSERVATION OF NEW PARTICLE FORMATION AT A RURAL SITE .....</b>	<b>106</b>
6.1 Introduction .....	106
6.2 Classification of the new particle formation and ozone pollution events .....	106
6.3 Comparison of NPF days and non-NPF days .....	112
6.3.1 Particle number concentration and diurnal variation .....	113
6.3.2 Effect of meteorological parameters on new particle formation .....	114
6.3.3 Effect of gas concentrations on new particle formation .....	118
6.4 Characteristics of new particle formation and growth .....	120

6.4.1 <i>Case study-typical new particle formation and growth event at Mt.TMS</i> .....	121
6.4.2 <i>Sulfuric acid vapor</i> .....	127
6.4.3 <i>VOCs</i> .....	133
6.5 <b>Conclusions</b> .....	136
<b>CHAPTER 7: OBSERVATION OF NUCLEATION MODE PARTICLE BURST AND NEW PARTICLE FORMATION EVENTS AT AN URBAN SITE</b> .....	137
7.1 <b>Introduction</b> .....	137
7.2 <b>General characteristics</b> .....	138
7.2.1 <i>Particle number concentration</i> .....	138
7.2.2 <i>Diurnal variations</i> .....	139
7.2.3 <i>Nucleation mode particles burst and NPF events</i> .....	141
7.3 <b>Nucleation mode particle burst events</b> .....	142
7.4 <b>NPF events</b> .....	147
7.5 <b>Comparison among burst events, NPF events and non-nucleation events</b> .....	151
7.6 <b>Summary and conclusions</b> .....	155
<b>CHAPTER 8: CONCLUSIONS AND SUGGESTIONS FOR FUTURE RESEARCH.</b> 157	
8.1 <b>Conclusions</b> .....	157
8.2 <b>Suggestions for future research</b> .....	162
8.2.1 <i>Further data analysis and validation</i> .....	162
8.2.2 <i>Further development of the method</i> .....	163
<b>REFERENCES</b> .....	165

# Chapter 1: Overview

## 1.1 Introduction

Atmospheric particulate pollution is a major public concern in Hong Kong due to the fact that particulate matters are closely related to human respiratory health, visibility reduction, eco-environmental damage and global climate (USEPA, 1996; Pope et al., 2002). The size of particles is directly linked to their potential for causing health problems. The adverse effects of particles with diameter less than or equal to 10  $\mu\text{m}$  (i.e.,  $\text{PM}_{10}$ ) and less than or equal to 2.5  $\mu\text{m}$  ( $\text{PM}_{2.5}$ ) have been widely studied and well recognized in the past decades. Recently, more and more studies have found that much smaller particles such as ultrafine particles (< 100 nm in diameter) in the air may be more important than  $\text{PM}_{2.5}$  and  $\text{PM}_{10}$  to cause adverse health effects (Pope et al., 2002; Li et al., 2003; Diapouli et al., 2007; Andersen et al., 2010), because they normally contain trace elements and toxins and can penetrate deep into the lungs (e.g., Morawska et al., 2004; Oberdorster et al., 2005; Bräuner et al., 2007; Stölzel et al., 2007) and some may get into the bloodstream (Schwartz et al., 2001; Oberdorster et al., 2004), owing to the high diffusion coefficients of the particles. Another fact is that more than 90% of all airborne particles, both outdoors and indoors, when measured by number concentration, are generally found to be ultrafine particles (e.g., USEPA 1996; Abt et al., 2000; Wichmann et al., 2000; Wallace and Howard-Reed, 2002; Sioutas et al., 2005; Zhu et al., 2008; Solomon et al., 2008; Hagler et al., 2009; Buonanno et al., 2009; Guo et al., 2008, 2010; Zhang et al., 2010; Wallace et al., 2008; Wallace and Ott, 2011). Therefore, people have high risk of exposure to these ultrafine particles

which can affect both lungs and heart. Particle pollution may occur all year as opposed to ozone, which occurs during the summer/autumn months in Hong Kong. Indeed, evidence shows that particle pollution exposure is linked to a variety of health problems, including increased respiratory symptoms, such as irritation of the airways, coughing, or difficulty breathing; decreased lung function; aggravated asthma; development of chronic bronchitis; irregular heartbeat; nonfatal heart attacks; and premature death in people with heart or lung disease.

Although growing epidemiological data indicates consistent and coherent associations between ambient ultrafine particles and health decrements such as mortality and morbidity, it is unlikely that all components of ultrafine particles are equally toxic (Utell et al., 1982; Schlesinger, 1989). In fact, sulfuric acid and ammonium bisulfate, both strongly acidic, are important components of ultrafine particles in the air. Indeed, accumulated evidence strongly suggests that the number of acid-containing ultrafine particles is more closely correlated with total mortality, morbidity and hospital admissions for respiratory diseases (Thurston et al., 1994, 2000; Wichmann et al., 2000; Cohen et al., 2000; Lippmann, 2000; Wichmann et al., 2000; Gwynn et al., 2001; Donaldson et al., 2002).

In addition, environmental effects of particle pollution include reduced visibility, environmental damage, and climate change (Kulmala et al., 2000). A better understanding of these aerosol-related effects requires a more comprehensive knowledge on the aerosol sources, and their atmospheric transformation processes. An important process controlling the number concentration of atmospheric particles is the new particle formation. This is

generally linked to nucleation of an initial cluster and subsequent growth of the cluster to a detectable diameter. Significant uncertainties arise from the dearth of understanding of the identity of the species involved in the formation (nucleation) and growth of these nuclei (Kulmala et al., 2004a). In many studies, sulfuric acid has been identified as the most important precursor contributing to atmospheric particle nucleation (Weber et al., 1999; Kulmala et al., 2004a; Jeong et al., 2004; Dunn et al., 2004; Morawska et al., 2008). A number of different mechanisms have been suggested to explain in situ nucleation in the atmosphere, such as (i) binary nucleation of sulfuric acid and water ( $\text{H}_2\text{SO}_4\text{-H}_2\text{O}$ ) (Nilsson and Kulmala, 1998; Vehkamäki et al., 2002); (ii) ternary nucleation involving a third molecule, i.e., ammonia ( $\text{NH}_3$ ) or organic vapors (Marti et al., 1997; Zhang et al., 2004a, b); (iii) ion-induced nucleation (Laakso et al., 2002) and (iv) halogen-oxide nucleation (Hoffmann et al., 2001). When sulfuric acid production is high and the existing particle number concentration is low, a large number of new nuclei mode sulfate particles can be formed (NARSTO, 2003). The new particle formation could contribute significantly to the number concentration of acidic particles. Once the new particles are thermodynamically stable, they can grow subsequently to a detectable diameter by condensation of photo-oxidized vapors and/or coagulation to sizes of 50–100 nm where they become active light scatters and cloud condensation nuclei (CCN). A number of studies concluded the oxidation products of volatile organic compounds (VOCs) dominate the particle growth to larger sizes (Zhang et al., 2004b; Laaksonen et al., 2008). In addition, acid-catalyzed heterogeneous reactions of VOCs on the acidic particle phase, for instance, have been proposed as an important mechanism

that might significantly enhance secondary organic aerosol production in the atmosphere (Jang et al., 2002; Edney et al., 2005; Gao et al., 2004; Inuma et al., 2007). Therefore, acidic particles could directly and indirectly affect climate change and visibility in terms of number concentration.

Thus, it is critical to be able to distinguish the acidic ultrafine particles from the total ultrafine particles, and to quantify the number concentrations and size distributions of acidic ultrafine particles in the air. Subsequently, effective control measures can be formulated and implemented. However, so far no effective techniques are available to systematically measure the number concentrations and size distributions of acidic ultrafine particles, and also no investigations are systematically conducted to make better understanding of the new particle formation in this region.

In Hong Kong, there have been a few studies of the acidity of aerosols (Pathak et al., 2004; Yao et al., 2007). However, the aerosol acidity was characterized by means of mass concentration, rather than by number concentration. In order to quantify the number concentration of acidic ultrafine particles, a new method needs to be developed. Based on a method reported by Horstman et al., (1967) for much larger particles, which used thin iron-coated detectors on which reaction pits were formed when the film was exposed to acidic particles, Cohen et al., (2004a) developed a method that can measure the size distribution and number concentration of acidic ambient ultrafine particles. It was found that the size-resolved number concentration of  $H^+$  to which people are exposed could be measured by iron nanofilm detectors, on which  $H_2SO_4$  droplets produce reaction sites. However, preliminary field measurements at a rural site in the United States indicated some critical

drawbacks and deficiencies of the method which caused the counts on the detectors to be relatively low for some of the sampling sessions, resulting in high statistical errors in calculations. This may suggest that the sampler is either unsuitable for an atmosphere with low levels of air pollutants, or required to be improved. Furthermore, although the iron nanofilm is promising for acidic particle analysis, questions remain to be answered: the rate of the reaction of acidic and non-acidic particles with the nanofilm; the correlation between particle acidity and the shape of the reaction site; the collection efficiency of the samplers; and the error in counting the reaction sites. Previous studies conducted in Hong Kong indicate that the pollution of particulate matters and ozone in the atmosphere is serious, suggesting that Hong Kong may be a proper location to test the detectors and to improve the sampler design (Pathak et al., 2003, 2004; Wang et al., 2005; Yao et al., 2007; So et al., 2007; Guo et al., 2008).

## **1.2 Aims and objectives**

In order to quantify the number concentration of acidic ultrafine particles in the air, a novel iron nanofilm detector method was developed in this study. The iron nanofilm detector is a thin iron-coated silicon chip (5 mm×5 mm×0.4 mm) with about 25 nm thick ironfilm. We assumed that each acidic particle would react with the iron, creating an elevated site or bump, on the film surface. The reaction sites are visualized by scanning the surface of the film using an Atomic Force Microscope (AFM). Two types of ultrafine particle samplers were used for ambient monitoring. One was a combined system in which an Electrostatic Precipitator (ESP) was preceded by scanning mobility particle sizer (SMPS) to classify particles size from the air samples for the

short term sampling. The other was an ultrafine diffusion sampler (DS), which was designed for long term sampling of ultrafine particles.

The methods for the quantification of acidic ultrafine particles were validated and established by field measurements. We tentatively chose two sites for the field measurements including a rural site at Mt. Tai Mo Shan (TMS) and an urban site at Hung Hom (HH) in Hong Kong. Field sampling was carried out respectively in a cold season at each site to validate the new methods. The results provided some information of the current contamination profile of acidic ultrafine particles in Hong Kong.

In addition, simultaneous measurements of particle number size distributions by SMPS+CPC (condensation particle counter), meteorological conditions (i.e., solar radiation, RH, temperature and wind) and trace gases (i.e., SO<sub>2</sub>, O<sub>3</sub>, NO<sub>x</sub> and CO) were performed to investigate aerosol formation (nucleation) and growth during the field measurements, and to explore the favorite weather condition and species responsible for the new particle formation in the air. The new particle formation (NPF) events were classified based on the increase of nucleation mode particle (<10 nm) number and growth of geometric mean diameter (GMD).

The major objectives of this study are therefore as follows:

- To improve a nanofilm detector for the collection of ambient acidic ultrafine particles;
- To modify and utilize an electrical precipitation sampler with the placement of the detectors which has a high collection efficiency;
- To design an ultrafine diffusion monitor with stable collection efficiency in which the nanofilm detector can be placed for long term sampling;

- To carry out field measurements at rural and urban sites in Hong Kong to assess the reliability and efficiency of the samplers;
- To determine the abundance of acidic and total ultrafine particles in Hong Kong; and
- To improve our understanding of ultrafine particle formation at rural and urban areas in Hong Kong.

### **1.3 Structure of the thesis**

The thesis comprises eight chapters as follows:

1) Chapter 1 provides the background and the major research objectives of this study.

2) Chapter 2 presents a brief literature review on characteristics of atmospheric ultrafine particles, effect of acidic UFPs (AUFPs) on the health and environment, methods for measurements of number concentrations of UFPs, and formation mechanisms of UFPs in clean and polluted areas.

3) Chapter 3 describes the methodology used in this study, including the laboratory experiments (i.e., preparation of iron nanofilm detectors, generation of aerosol standards, calibration of instruments, and performance tests of detector) and field measurements (i.e., description of sampling sites, measurement techniques, and data analysis)

4) Chapter 4 develops iron nanofilm detectors for measuring ambient acidic ultrafine particles, and presents a combined collection system SMPS + ESP utilized with iron nanofilm detectors to measure the AUFPs in the air.

5) Chapter 5 designs a new diffusion sampler for long term measurement of AUFPs in the atmosphere.

6) Chapter 6 investigates the new particle formation at a rural site in Hong Kong.

7) Chapter 7 studies nucleation mode particle burst and new particle formation events at an urban site in Hong Kong.

8) Chapter 8 highlights the major findings, the significant contributions of the study, and the suggestions for future research.

## **Chapter 2: Literature Review**

### **2.1 Characteristics of atmospheric ultrafine particles**

Air pollution caused by ultrafine particles (UFPs, with a diameter smaller than 100 nm) has become a topic of great interest in terms of air quality impairment, public health and global climate. Typically, UFPs account for about 90% of the total number concentration of particles in both outdoor (e.g., USEPA 1996; Wichmann et al., 2000; Sioutas et al., 2005; EPA 2007; Guo et al., 2008; Morawska et al., 2008; Solomon et al., 2008; Zhu et al., 2008; Hagler et al., 2009; Buonanno et al., 2009) and indoor air (e.g., Abt et al., 2000; Wallace and Howard-Reed 2002; Guo et al., 2010; Zhang et al., 2010; Wallace et al., 2008; Wallace and Ott, 2011; González et al., 2011). In aerosol science, atmospheric UFPs are discussed in terms of modes (i.e., nucleation, Aitken and accumulation). Each has distinctive sources, size range, formation mechanisms, chemical composition and deposition pathways (Hinds, 1999). Due to their high diffusion coefficients and great accumulation ability in the regional lymph nodes and the lung, ultrafine particles can enter deep into the ciliated and alveolar sections of the lung (e.g., Morawska et al., 2004; Oberdorster et al., 2005; Bräuner et al., 2007; Stölzel et al., 2007) and even bloodstream (Schwartz et al., 2001; Oberdorster et al., 2004), and contribute to negative health effects (Pope et al., 2002; Li et al., 2003; Diapouli et al., 2007; Andersen et al., 2010). As such, ambient UFPs may be more important than PM<sub>2.5</sub> (particles with diameter  $\leq 2.5\mu\text{m}$ ) and PM<sub>10</sub> (particles with diameter  $\leq 10\mu\text{m}$ ) in terms of their number-associated (Diapouli et al., 2007; Berghmans

et al., 2009; Hoek et al., 2008, 2010) and size-associated effects on human health (Ramgolam et al., 2008; Napierska et al., 2009; Sohaebuddin et al., 2010; Ulrich et al., 2011). In order to better understand the atmospheric UFPs and their impact on atmospheric chemistry, human health, visibility reduction and global climate, it is significantly important to study the sources and the physical/chemical characteristics of these nanoparticles (e.g., Kulmala et al., 2004a; Seinfeld and Pandis, 2006; Stölzel et al., 2007; Morawska et al., 2008).

### **2.1.1 Nucleation mode**

Nucleation (or nuclei) mode particles (typically defined as the <10 nm range) are predominantly a mixture of two or more mutually exclusive aerosol populations (Lingard et al., 2006). Nucleation mode particles are found in high number concentrations near sources. These are not present in primary exhaust emissions, but are thought to be formed through nucleation (gas-to-particle conversion) in the atmosphere after rapid cooling and dilution of emissions when the saturation ratio of gaseous compounds of low volatility (i.e., sulphuric acid) reaches a maximum (Charron and Harrison, 2003; Kittelson et al., 2006). Most of these particles comprise sulphates, nitrates and organic compounds (Seinfeld and Pandis, 2006). These particles are typically liquid droplets primarily composed of readily volatile components derived from unburned fuel and lubricant oil (i.e., the solvent organic fraction: *n*-alkanes, alkenes, alkyl-substituted cycloalkanes, and low molecular weight polyaromatic hydrocarbon compounds) (Lingard et al., 2006; Sakurai et al., 2003; Wehner et al., 2004). Collisions with each other and with particles in the accumulation mode are largely responsible for their relatively short

atmospheric life time. Dry deposition, rainout and/or growth through condensation are the other dominant removal mechanisms (Hinds, 1999).

Due to their nanometer-scale size and toxic compounds, the nucleation mode particles can penetrate into the ciliated and alveolar sections of the lung and even bloodstream (Oberdorster et al., 2005), contributing to negative health effects. Consequently, advancing our understanding on the formation and loss processes of these nucleated particles in the atmosphere has become critically important.

### **2.1.2 Aitken and accumulation modes**

The Aitken mode is typically defined as the 10-100 nm range. Particles in this mode arise from the growth or coagulation of nucleation mode particles as well as by production in high numbers by primary combustion sources such as vehicles (Kulmala et al., 2004b). These particles are mainly composed of a soot/ash core with a readily absorbed outer layer of volatilisable material (Lingard et al., 2006). Accumulation mode particles (typically defined as the 100-300 nm size range and sometimes referred to as the 'soot mode') are carbonaceous (soot and/or ash) agglomerates. They derive mainly from the combustion of engine fuel and lubricant oil by diesel-fuelled or direct injection petrol-fuelled vehicles (Wehner et al., 2009), as well as from the coagulation of nucleation mode particles (Hinds, 1999). Most of these particles are formed in the combustion chamber (or shortly thereafter) with associated condensed organic matter (Kittelson et al., 2006). They are mainly composed of two or more distinct components that are either co-joined or exist with one component adsorbed onto the surface of another, forming an outer layer and

inner core (Lingard et al., 2006). These particles are not removed efficiently by diffusion or settling, as they coagulate too slowly, but rainout or washout is an effective removal mechanism (Hinds, 1999). Thus, they tend to have relatively long atmospheric life times (typically days to weeks) and can travel over very long distances in the atmosphere (Anastasio and Martin, 2001). More importantly, particles in this mode are of sizes comparable with the wavelengths of visible lights, and hence account for much of the man-made visibility impairment problem in many urban areas (Seinfeld and Pandis, 2006). Particles discussed in this review are combination of all three of the above modes.

## **2.2 Effect of acidic UFPs (AUFPs) on human health and environment**

Although substantial toxicological evidence of the harmful effects of exposure to ultrafine particles exists, it is unlikely that all components of ultrafine particles are equally toxic (Utell et al., 1982; Schlesinger, 1989). Among all the chemical components, sulfuric acid ( $\text{H}_2\text{SO}_4$ ) and ammonium bisulfate ( $\text{NH}_4\text{HSO}_4$ ) are important chemicals in ultrafine particles in the atmosphere. AUFPs consists of primary particles generated directly from sources and secondary particles (such as sulfate and nitrate) formed by reactions that occur in the atmosphere. Sulfuric acid and nitric acid, for example, are produced by gas-to-particle conversion of sulfur dioxide and nitrogen dioxide, respectively, in the presence of hydroxyl radicals. Once formed, these liquid particles either condense on preexisting particles or combine with each other to form new particles. They generally exist in the ultrafine particle fraction when first

formed (Schlesinger and Cassee 2003). When sulfuric acid production is high and the existing particle number (PN) concentration is low, a large number of new nuclei mode sulfate particles can be formed, contributing significantly to the total number concentration (NARSTO, 2003). Chemical reactions in the atmosphere may lead to chemical species with low vapor pressure (e.g., sulfuric acid) at ambient temperature. These processes tend to produce new particles that are more regionally (thus homogeneously) dispersed over an urban or rural area.

### **2.2.1 Health effects**

Since early 20th century, a number of severe sulfate acid episodes have clearly demonstrated that acidic aerosol can affect human health; these included documented increases in mortality and morbidity (Lioy, 1989; Ronald, 1995). In the last decade, a number of studies indicated the close association between the acidity of ultrafine particles and adverse health effects such as the prevalence of bronchitis symptoms and lung function decrements (e.g., Cohen et al., 2000, 2004a; Lippmann, 2000; Thurston et al., 2000; Wichmann et al., 2000; Gwynn et al., 2001; Donaldson et al., 2002). Although health was clearly affected during these episodes and acidity was a candidate for the responsible agent, it has been difficult to ascertain which agents were involved. In the past several years extensive research was launched to learn the significance of acidic aerosols on human health (Lioy, 1989; Dockery et al., 1993; Thurston et al., 1994; Pope et al., 1995; Dockery et al., 1992; Wyzga and Folinsbee, 1995; Zelikoff et al., 1997; Kleinman and Phalen, 2006; Heyder et al., 2009; Van der Hagen and Järnberg, 2009). Epidemiology results

are broadening the perspective from a focus on acidity to a focus on acidic fine particulate matter number and size (Chen et al., 1992, 1995; Kimmel et al., 1997).

Chen et al., (1992) reported that acidic sulfate is the most toxicologically important sulfur oxide which exists in the ambient air. To determine if particle size influences toxic effects of sulfuric acid, they investigated the effects of sulfuric acid aerosols of two different sizes on biochemical and cellular parameters of bronchoalveolar lavage fluid from exposed guinea pigs. Guinea pigs were exposed to fine (mass median diameter = 0.3  $\mu\text{m}$ ), and ultrafine (mass median diameter = 0.04  $\mu\text{m}$ ) sulfuric acid aerosols at 300  $\mu\text{g}/\text{m}^3$  for 3 hr/day. The animals were euthanized immediately and 24 hr after 1 and 4 days of exposure and lungs were lavaged. Elevated  $\beta$ -glucuronidase, lactate dehydrogenase activities, and total protein concentration as well as decreased cell viability were observed in the lavage after a single exposure to sulfuric acid aerosols of both sizes. Chen et al., (1995) provided important evidence that the number concentration of acidic particles plays a role in cellular response. Guinea pigs were exposed to varying amounts of  $\text{H}_2\text{SO}_4$  (50 to 300  $\mu\text{g}/\text{m}^3$  layered onto  $10^8$  ultrafine carbon core particles/ $\text{cm}^3$ ) and to a constant concentration of acid (350  $\mu\text{g}/\text{m}^3$  layered onto  $10^6$ ,  $10^7$ , or  $10^8$  particles/ $\text{cm}^3$ ). All of these particles had diameters of approximately 90 nm, and the acid was adsorbed onto a carbon core. Indicators of irritant potency in macrophages harvested from the lungs of exposed animals clearly showed an increase either (1) when a constant dose of acid was divided into an increased number of particles or (2) when the acid dose was increased and the particle number concentration remained constant. Early work by Amdur and Chen (1989)

suggested that number concentration was important for H<sub>2</sub>SO<sub>4</sub> aerosol, and Hattis et al., (1987, 1990) named the concept *irritation signaling*.

However, subsequent research of Chen et al., (1995) indicated that inhaled acid-coated particles much smaller than those discussed by Hattis et al., (1987, 1990) were capable of producing lung responses. Oberdörster et al., (2000) reported that nonreactive, low-solubility ultrafine particles did not appear to cause inflammation in young healthy rats. Thus it is important to be able to distinguish between the number of acidic ultrafine particles and the total number of ultrafine particles for epidemiologic studies. The issue of particle size is more difficult to address due to the scarcity of data. Previously, no effective measurement methods were available to systematically obtain these important data. The issue of particle size is currently unclear and more research is warranted.

### **2.2.2 Visibility**

Visibility impairment is generally caused by a build-up of suspended particles in the atmosphere (Horvath, 2008). It increases with relative humidity (RH) and atmospheric pressure and decreases with temperature and wind speed (Tsai, 2005). At high (e.g., 90%) relative humidity, the light scattering cross-sectional areas of particles enlarge by uptake of water.

Atmospheric acidic aerosols tend to be more hygroscopic than their neutralized form, as indicated by the positive correlations between particle phase acidity and measured water content and between deliquescence RH of ambient particles and their NH<sub>4</sub><sup>+</sup>/SO<sub>4</sub><sup>2-</sup> ratio. Larger hygroscopicity enhances particles' ability to scatter light and to nucleate cloud droplets, and thus their

influence on visibility and climate. For an ammonium sulfate particle, the increase may be by a factor of five or more above that of the dry particle (Malm and Day, 2001). However, the relative contributions to visibility improvement from reductions in atmospheric acidic ultrafine particle concentrations and the degree to which control of their emissions are largely unknown due to lack of acidic ultrafine particle data.

### **2.2.3 Climate**

There is an obvious potential for increased anthropogenic or other emissions of SO<sub>2</sub> to produce more of the large upper troposphere nucleation events. Extensive measurements over the Pacific have shown that the small particles produced in such events age and subside to form cloud condensation nuclei (CCN) when mixed into the marine boundary layer (Clarke and Kapustin, 2002).

Particle phase acidity has also been linked to secondary aerosol formation. Acid-catalyzed heterogeneous reactions, for instance, have been proposed as an important mechanism that might significantly enhance secondary organic aerosol (SOA) production in the atmosphere (Jang et al., 2002; Edney et al., 2005; Gao et al., 2004; Iinuma et al., 2007; Li et al., 2010a). Up to several fold increases in SOA mass have been observed in chamber studies when acidic seed particles were used (e.g., Jang et al., 2002; Edney et al., 2005). Similar multifold enhancements in SOA production in the Houston area could be inferred based on the particle volume growth rates measured in industrial plumes rich in SO<sub>2</sub> and volatile organic compounds (VOCs) compared to those containing only VOCs or SO<sub>2</sub>. In addition, Chu (2004) observed

simultaneous increases of OC and  $\text{SO}_4^{2-}$  mass concentrations accompanied with a charge deficit of  $\text{NH}_4^+$  during regional high  $\text{PM}_{2.5}$  episodes in the Eastern U.S. and thus suggested a link between acidic particles and summertime SOA formation. A large number of observations have shown that atmospheric new particle formation by nucleation takes frequently place in remote environment (e.g., Kulmala et al., 2004a; Kulmala and Kerminen, 2008). Under favorable conditions, nucleated particles grow into sizes in which they are able to produce new cloud condensation nuclei (Wiedensohler et al., 2009). The freshly formed aerosols become climatically important when they are able to grow to sizes of 50 nm and larger. Particles in this size range can act as cloud condensation nuclei (CCN), significantly increasing the indirect radiative effect of clouds (e.g., McMurry et al., 2011).

## **2.3 Measurements of number concentrations of UFPs**

Instruments measuring the number concentration and size of UFPs generally have two components: one collects particles within a certain size range, and the other analyzes the selected particles.

### **2.3.1 Real-time measurements of UFPs**

Generally, atmospheric nanoparticles display a variety of shapes (e.g., tabular, irregular, aggregated or agglomerates), rather than an ideal sphere. Aerodynamic equivalent ( $D_a$ ), Stokes ( $D_s$ ) or electrical mobility equivalent ( $D_p$ ) diameters are usually used to classify particles when measuring the particle numbers in moving air. Using different operating principles, the optical analyzers (e.g., aerodynamic particle sizer, APS), aerodynamic analyzers (e.g.,

laser aerosol spectrometer, LAS) and electrical mobility analyzers (e.g., scanning mobility particle sizer, SMPS) are developed and utilized for measurement of particles in different size ranges.  $D_p$  is widely used in instruments for measurement of ultrafine particle and is defined as the diameter of a spherical particle that has the same electrical mobility as the irregular particle in question. For real-time particle number and size distribution measurements, the majority of the published studies applied electrostatic classifiers (EC) and condensation particle counters (CPC) manufactured by TSI Incorporated, with a much smaller number using other instruments, for example GRIMM, or air ion mobility spectrometers, which have enabled measurements down to 0.4 nm (Kumer et al., 2010). A review of the capabilities and limitations of most advanced commercially available instruments that are currently used for UFPs monitoring is given below.

#### **2.3.1.1 Scanning mobility particle sizer (SMPS)**

The SMPS (TSI Inc. [www.tsi.com](http://www.tsi.com)) system uses an electrical mobility detection technique to measure number and size distributions. It consists of three components, (i) a bipolar radioactive charger for charging the particles, (ii) a differential mobility analyzer (DMA) for classifying particles by electrical mobility, and (iii) a condensation particle counter (CPC) for detecting particles (Stolzenburg and McMurry, 1991; Wang and Flagan, 1989; Wiedensohler et al., 1986).

The SMPS (3034 TSI Inc.) measures  $D_p$  between 10 and 487 nm using 54 size channels (32 channels per decade) for number concentrations in the range from  $10^2$  to  $10^7$   $\text{cm}^{-3}$ . This model takes 180 s to analyze a single scan. The

later SMPS model (3934 TSI Inc.) uses up to 167 size channels (up to 64 channels per decade) to measure particle diameters between 2.5 and 1000 nm at a minimum sampling time of 30 s. Adjusting the sampling flow rate from 0.2 to 2 L min<sup>-1</sup> allows it to measure the number concentrations in the 1-10<sup>8</sup> cm<sup>-3</sup> range. The SMPS is regarded as a standard instrument by which other ultrafine particle sizers are compared, though it has its own limitations.

### **2.3.1.2 Fast mobility particle sizer (FMPS)**

The FMPS (model 3091, TSI Inc. [www.tsi.com](http://www.tsi.com)) provides particle number distribution measurements based on  $D_p$  up to a sampling frequency of 1 Hz. It can measure particles in the 5.6-560 nm range using 32 channels (16 channels per decade of size). A high sample flow rate (10 L min<sup>-1</sup>) helps to minimize particle sampling losses due to diffusion (Kumar et al., 2008) and operation at ambient pressure prevents evaporation of volatile and semi-volatile particles. It uses an electrical mobility detection technique similar to that in the SMPS. As opposed to the SMPS, which uses CPC, the FMPS uses multiple, low-noise electrometers for particle detection.

### **2.3.1.3 Ultrafine particle (UFP) monitor**

The UFP monitor (model 3031, TSI Inc., [www.tsi.com](http://www.tsi.com)) measures particle number distributions based on  $D_p$  at a time resolution of 10 min with 1 min additional zeroing time. It can measure particles in the 20-1000 nm range using 6 size channels at a 5 L min<sup>-1</sup> sample flow rate. It can measure concentrations in the 500-10<sup>6</sup> cm<sup>-3</sup> range at 20 nm and 50-10<sup>6</sup> cm<sup>-3</sup> range at 200 nm.

#### **2.3.1.4 Differential mobility spectrometer (DMS)**

The DMS500 (Cambustion, [www.cambustion.com](http://www.cambustion.com)) offers fast response measurement of particle number distributions based on  $D_p$ . It uses a differential mobility classifier that provides very fast time response (200 ms T10-90%, at a data rate of 10 Hz, T90 is the time taken for the output to reach 90% of its final value). It is capable of measuring over two size ranges, namely 5-1000 nm and 5-2500 nm. Each range requires different set-points for the instrument's internal flows, voltage and pressure. The instrument uses primary and secondary dilution stages. The primary stage is used to dilute the sample flow with compressed air at the point of sampling; this is generally suitable for ambient measurements. The secondary dilution is used for the sampling of concentrated aerosols (e.g., engine emissions) to bring concentrations within the dynamic range of the instrument (Cambustion, 2003-9). A sample flow rate of 8 L min<sup>-1</sup> is used when working in the 5-1000 nm size range, decreasing to 2.5 L min<sup>-1</sup> for the 5-2500 nm size range.

#### **2.3.1.5 GRIMM nanoparticle measuring systems**

GRIMM Aerosol Technik ([www.grimm-aerosol.com](http://www.grimm-aerosol.com)) produces a number of instruments that measure particle number concentrations and distributions using combinations of SMPS, DMA and CPC systems. The model SMPS+C includes DMA with a CPC to measure particles in the 5-1110 nm size range in 44 channels. The model WRAS (wide range aerosol spectrometer) incorporates an additional GRIMM aerosol spectrometer and can measure particles up to 32 nm with 72 channels. The model GRIMM SMPS+E is an integration of a DMA and a Faraday Cup Electrometer. It can measure

particles in the 0.8-1100 nm in 44, 88 or 176 size channels with a very fast sampling frequency (T90 response: 0.2 s). In this study, a GRIMM SMPS + CPC (model 5.400) was used to measure the particle number concentration and number-weighted size distribution.

Recent progress in measurement techniques enables us to measure atmospheric nucleation at the size (mobility diameter) of 1.5 ( $\pm 0.4$ ) nm. The detection limit has decreased from 3 to 1 nm within the past 10 years. Due to the progress in measurement techniques, the formation of new atmospheric aerosol particles and their subsequent growth have been observed frequently in various locations all over the world. The atmospheric nucleation rate (or formation rate) and growth rate (GR) are key parameters to characterize the phenomenon (see Section 2.4).

### **2.3.2 Real-time measurements of AUFPs**

Current instruments are not capable of detecting real-time number concentration of acidic particles. While, ion mass spectrometers can be used to quantitatively measure the sulfate composition of nanoparticles and gas-phase sulfuric acid in the ambient measurements. For example, the nano aerosol mass spectrometer (NAMS) is capable of single-particle analysis from 7 to 30 nm in diameter (Bzdek et al., 2012). Briefly, charged particles entering the mass spectrometer are focused aerodynamically and electro-dynamically and then are size selectively captured in an ion trap. Trapped particles are irradiated with a high-energy pulsed laser beam to reach the “complete ionization limit” where a plasma is formed. The irradiated particles are completely disintegrated into positively charged atomic ions that are mass

analyzed by time-of-flight. NAMS is currently employed to measure the nanoparticle elemental composition during NPF events to investigate the contribution of sulfate (sulfuric acid) to nanoparticle growth. In addition, thermal desorption chemical ionization mass spectrometer (TDCIMS) can analyze molecular characterization of semivolatile components (e.g., gas-phase sulfuric acid) in collected nanoparticles down to 6 nm in diameter.

### **2.3.3 Off-line measurements of UFPs**

Suitable collection methods vary according to the size and nature of the particles under investigation. An applicable method must allow the particles to be presented as a homogeneous uniform deposit, while not altering the relevant particle characteristics significantly. This analysis is limited in terms of time resolution, and its results may be biased by sampling artifacts, such as losses or gains of semi volatile components. However, it offers the advantage of collecting sufficient material for analysis of components present in small amounts. The instruments used in our study to collect particles are electrostatic precipitator (ESP) and the diffusion sampler (DS), which can be utilized to collect particles on a substrate for feature analysis. The ESP precipitates particles ranging in size from approximately 5.5 to 350 nm to obtain uniform particle deposits by charging them. The DS relies on the diffusive properties (due to Brownian motion) of ultrafine particles, whereby the particles adhere when they hit a surface (Knuston, 1999).

For off-line analysis, over the past decade, development of the resolution and analytical capabilities of the electron microscope has further increased its applicability to the study of ultrafine particles. The development of scanning

probe microscopy (SPM) such as the scanning tunneling microscope (STM) and atomic force microscope (AFM) have further added to the available instrumentation for nanometer particle analysis. All these methods can be operated in a range of environments, including atmospheric conditions, liquid immersion and vacuum. Of all the available SPM methods, AFM is perhaps the most applicable to aerosol analysis, as high-resolution imaging is possible in air, and there are relatively few limitations on the type of sample imaged. Friedbacher et al., (1995) have successfully applied AFM to the analysis of ultrafine particles collected on a polyester foil using a low pressure cascade impactor. The substrate was found to have a suitably flat surface (root mean square roughness of 1 nm over 4  $\mu\text{m}^2$ ) to allow the identification and sizing of sub-30 nm particles. The AFM-derived size distribution agreed well with that expected from the impactor stage cut-off. However, the presence of large-diameter particles with very little height in samples indicated that there was some degree of particle modification subsequent to sampling, bringing into question the direct interpretation of aerosol size distribution from the AFM data. The assumption was made that these particles were the result of droplet deposition followed by evaporation, leaving a residue. Interestingly, the ability to differentiate by height gave the analysis method an advantage over TEM imaging, where differentiation between droplet residues and solid particles is not always straightforward.

#### **2.3.4 Off-line measurements of AUFPs**

As a matter of fact, some pilot studies were carried out to quantify the number of acidic particles. For instance, in the earliest study, Gerhard and Johnstone

(1955) and Waller et al., (1963) successfully obtained reaction spots of acidic particles in gelatinous films. However, it was impossible to individually detect droplets with diameter less than 1.0  $\mu\text{m}$  at that time. By measuring changes of light transmission and resistance of thin metal films, Lodge and Havlik (1960) used the changes as indicators of atmosphere pollution. Electronic micrographs of the exposed films showed extensive surface mottling and pitting of the metal films. Hayashi et al., (1961) used metal-coated glass slides to detect and size acid aerosols which were nebulized to form holes as reaction spots on the film surface, and also related the sizes of observed reaction pits to aerosol droplet diameters. Unfortunately, the smallest size of the acidic droplets that were characterized was several microns in diameter. Horstman et al., (1967) used thin iron-coated detectors, on which reaction pits were formed when the film was exposed to acidic particles, to size acidic particles with diameter much larger than 0.1  $\mu\text{m}$  by electron microscope. For submicrometer size particles, Bigg et al., (1974) developed a method of spot reaction by applying a thin film of reagent on the surface of the sample; later Mamane (1977) modified and improved this method specifically for soluble sulfates based on the reaction of the sulfate ion on barium chloride film. Huang and Turpin (1996) had also noted the ring formation as a characteristic of  $\text{H}_2\text{SO}_4$  particles by scanning electron microscopy (SEM) on carbon film substrates. Most recently, Cohen et al., (2004a) developed iron nanofilm detectors by vapor deposition for the measurements of acidic particles in New York for the first time. The nanofilm detectors were examined with SPM for the enumeration of reaction sites formed by acidic particles. In their study, the average concentrations of ambient acidic particles ranged from approximately

100 to 1800 particles/cm<sup>3</sup> over sampling periods. And they also reported that the fraction of UFPs that were acidic varied from about 10% to 88% and most of the H<sup>+</sup> was in the size fraction with diameters between 280 and 530 nm. However, sometimes fewer or no acidic ultrafine particles were detected in their study (Cohen et al., 2004b), suggesting that the method might not be suitable for an atmosphere with low levels of air pollutants, or should be systematically improved.

## **2.4 Formation mechanisms of UFPs in clean and polluted atmospheres**

A variety of formation mechanisms have been suggested for atmospheric aerosols (Kulmala et al., 2000). Generally, the formation of nucleation mode particle requires two processes: the nucleation of stable atmospheric clusters (1-3 nm) and the growth of these clusters into observable sizes (> 3 nm). Altogether, the driving force for nucleation and the growth of freshly formed particles to Atiken mode particles is the sufficiently high concentration of condensational vapors, such as sulfuric acid and possibly other organic compounds with a low saturation vapor pressure formed by photochemical oxidation reaction. Sulfuric acid has been found to be a key compound in atmospheric nucleation in many studies (Kulmala et al., 2006; Riipinen et al., 2007; Sipilä et al., 2010). Also recent study (e.g., Kerminen et al., 2010) found that some organic acids produced from monoterpene oxidation can nucleate with sulfuric acid to form very stable clusters. However, for particle growth, observations suggest that the contribution of sulfuric acid to particle growth is typically from a few percents to some tens of percents of the observed particle

growth rate (Boy et al., 2005; Nieminen et al., 2010; Riipinen et al., 2011), while organics with a very low saturation vapor pressure (Tunved et al., 2006; Jimenez et al., 2009) can be considered as the most probable candidates of the vapors responsible for the fraction of nucleation mode growth that is not explained by sulfuric acid.

To date, numerous measurements have been conducted in different locations to study the size distribution of submicrometer particles and their formation processes, including clean areas, i.e., free troposphere (e.g., Weber et al., 2001), boreal forests (e.g., O'Dowd et al., 2002a, b; Vehkamäki et al., 2004; Tunved et al., 2006; Dal Maso et al., 2007; Asmi et al., 2011), coastal rural areas (e.g., Kulmala et al., 2004b; Lee et al., 2008), high mountain-top (e.g., Gannet et al., 2011), Antarctic/Arctic areas (e.g., Birmili and Wiedensohler, 2000; Park et al., 2004); and polluted urban areas, i.e., Atlanta (Woo et al., 2001), St. Louis (Shi et al., 2002), Pittsburgh (Stanier et al., 2004a&b), Birmingham, UK (Alam et al., 2003), Mexico City (Dunn et al., 2004), East St. Louis (Qian et al., 2007), and Brisbane (Guo et al., 2008; Cheung et al., 2011). Generally, new particle formation (NPF) events are much more frequently observed in rural/remote areas than in urban locations. In China, the field measurements for particle size distribution were carried out in several cities and regions in recent years. Short-term intensive studies on NPF were performed in Beijing (Yue et al., 2009), Pearl River Delta (PRD) (Liu et al., 2008; Guo et al., 2008), Yangtze River Delta (YRD) (Gao et al., 2009) and Hong Kong (Yao et al., 2010). Moreover, a couple of long-term continuous measurements were conducted in Beijing (e.g., Wu et al., 2008; Shen et al., 2011) and a remote mountain site, Mt. Waliguan (Kivekäs et al.,

2009). The mechanisms of particle formation (both in remote and urban environment) are further discussed as below.

#### **2.4.1 Remote environment**

Of particular importance in remote environments is the formation of new particles, of which the main mechanism is nucleation of low-volatile gas-phase compounds, followed by their growth into small particles (Kulmala et al., 2004a, 2013; Holmes, 2007; Morawska et al., 2008; Zhang et al., 2011).

In remote environments particle formation events are preceded by an increase in the atmospheric concentration of sulfuric acid, with the increase in the particle number occurring about 1–2 h after an increase in sulfuric acid was measured (Weber et al., 1997). This is followed by a relatively small particle growth rate between 1 and 2 nm h<sup>-1</sup> (Weber et al., 1997; Marti et al., 1997; Birmili and Wiedensohler, 2000). These events showed a linear relationship between the number of newly formed particles and the production rate of sulfate acid indicating the importance of sulfate acid. Sipilä et al., (2010) showed correlations between measured nucleation rates of 1.5 nm particles and sulfuric acid concentrations and suggested that freshly formed particles contain one to two sulfuric acid molecules. Field measurements have identified H<sub>2</sub>SO<sub>4</sub> as the key player in atmospheric nucleation (e.g., Weber et al., 1997; Sipilä et al., 2010). The best relation between the nucleation rate ( $J$ ) and H<sub>2</sub>SO<sub>4</sub> concentration is usually obtained when assuming  $J \sim [\text{H}_2\text{SO}_4]^n$ , where the exponent  $n$  lies in the range 1–2 in the clean areas (Weber et al., 1997; Kulmala et al., 2006; Riipinen et al., 2007; Kuang et al., 2008; Sipilä et al., 2010).

Several mechanisms have been suggested to explain in situ formation (nucleation) in the atmosphere. These include sulfuric acid–water binary nucleation (Nilsson and Kulmala, 1998; Vehkamäki et al., 2002), ternary nucleation of H<sub>2</sub>SO<sub>4</sub>–H<sub>2</sub>O involving ammonia and amines (Benson et al., 2009, 2011), nucleation of H<sub>2</sub>SO<sub>4</sub>–H<sub>2</sub>O assisted with organic acids (Marti et al., 1997; Zhang et al., 2004b, 2011), ion-induced nucleation (Laakso et al., 2002), and halogen-oxide nucleation (Hoffmann et al., 2001). Significant uncertainties arise from the lack of understanding of the identity of the species involved in the formation and growth of these nuclei (Kulmala et al., 2004a). Laboratory experiments (e.g., Sipilä et al., 2010) and field observations (Weber et al., 1999; Kulmala et al., 2004a; Riipinen et al., 2007) have shown that H<sub>2</sub>SO<sub>4</sub> is important in NPF in the atmosphere. However, field measurements (Eisele and McMurry, 1997; Weber et al., 1998, 1999; Janson et al., 2001) and model simulations (Kulmala et al., 2000; Kerminen et al., 2001; Pirjola and Kulmala, 2001; Anttila and Kerminen, 2003) also have indicated that condensation of sulfuric acid alone is often not enough to grow these nuclei to detectable sizes. To account for the growth of the fresh nuclei, condensation of organic species (Kerminen et al., 2000; Anttila and Kerminen, 2003), heterogeneous reactions (Zhang and Wexler, 2002), and ion-enhanced condensation (Laakso et al., 2002) have been suggested.

Binary nucleation (H<sub>2</sub>SO<sub>4</sub>–H<sub>2</sub>O) theory consistently predicts nucleation rates lower than measured rates in the lower troposphere (Weber et al., 1998; Kulmala et al., 2001; O’Dowd et al., 2002a, b). Other species are also needed to explain atmospherically observed formation rate. Possible species include NH<sub>3</sub> (Benson et al., 2009, 2011) 1,3,5-trimethylbenzene (Paasonen et al.,

2010), amines (Smith et al., 2010) and volatile organic compounds (VOCs) such as organic acids (O'Dowd et al., 2002b; Bonn and Moortgat, 2003; Zhang et al., 2004b). Low-volatile organic compounds are of specific interest for several reasons. First of all, large amounts of organic aerosol precursor vapors are emitted into atmosphere, and in future such emissions might even be increased as a result of climate change (Kulmala et al., 2004b; Rinne et al., 2009). Secondly, the contribution of secondary sources to the atmospheric organic aerosol load in general, and to aerosol dynamics in particular, seems to be much larger than previously thought (e.g., Jimenez et al., 2009). Thirdly, the growth of freshly-nucleated atmospheric aerosol particles cannot usually be explained without a significant contribution by vapors other than sulfuric acid (Weber et al., 1997; Birmili et al., 2003; Boy et al., 2005; Smith et al., 2008), and indirect chemical measurements indicate that organics are present in nm-sized and larger particles during atmospheric new particle formation events (O'Dowd et al., 2002b; Laaksonen et al., 2008).

In addition to organic compounds, ammonia and amines are abundant in the atmosphere and lowers the vapor pressure of H<sub>2</sub>SO<sub>4</sub> above the solution (Scott and Cattell, 1979) by stabilizing the cluster. Since recent quantum chemical calculations have shown that ammonia and amines can form neutral and ion clusters with H<sub>2</sub>SO<sub>4</sub> molecules efficiently (Kurtén et al., 2007). More evidence on the possible role of amines in NPF was found in field measurements which showed the presence of aminium ions in nanoparticles (Smith et al., 2008). The size-resolved composition of particles in the 20–1000 nm diameter range was measured during the Pittsburgh Air Quality Study (PAQS) by Zhang et al., (2004a). However, it was found that fresh particles with diameters of 20–33

nm were very acidic during the nucleation events. This observation seems to contradict the results of previous work that suggested that the presence of ammonia vapor is required for the onset of nucleation (Gaydos et al., 2005).

In forests, O'Dowd et al., (2002a) showed that particle formation can commonly occur from biogenic precursors. Tunved et al., (2006) showed a direct relation between emissions of monoterpenes and gas-to-particle formation over these regions which were substantially lacking in anthropogenic aerosol sources. Boreal forest observations in Finland also indicated a connection between nucleation mode growth and ambient concentrations of monoterpenes (Laaksonen et al., 2008). Therefore, secondary organic aerosol formation from monoterpenes is an important source in these environments. Further, the authors show that the forest provides an aerosol population of  $1-2 \times 10^3 \text{ cm}^{-3}$  of climatically active particles during the late spring to early fall period, presenting a substantial source of global importance.

In the marine environment several different particle production mechanisms are proposed such as the seawater bubble-burst process (O'Dowd et al., 2004) and the generation of coastal iodine particles from macroalgal iodocarbon emissions (Raes, 1995; Kulmala et al., 2000; O'Dowd et al., 2004; O'Dowd and Hoffmann, 2006). While iodine-containing particles are found in large numbers at Mace Head research station in Ireland, they are not likely to play an important role globally (McFiggans, 2005). Wind produced bubble-burst particles containing salt are ubiquitous in the marine environment (Ayers and Gras, 1991), but these represent less than 10% of particle numbers. The

majority of particles are much smaller than these salt particles and their origins remain only partially explained.

The above studies indicate that elevated sulfuric acid concentrations and low particle surface area in the clean environments are required for nucleation to occur and are indeed favored in the atmosphere.

#### **2.4.2 Urban environment**

In general, particles from vehicle emissions can be divided into two broad categories, depending on the location of their formation. They can be formed in the engine or tailpipe (primary particles) or they can be formed in the atmosphere after emission from the tailpipe (secondary particles). Earlier studies in urban environments claimed that nucleation mode particles are not present in primary exhaust emissions, but are formed through nucleation in the atmosphere after rapid cooling and dilution of emissions when the saturation ratio of gaseous compounds of low volatility (i.e., sulfuric acid) reaches a maximum (Charron and Harrison, 2003; Kittelson et al., 2006; Morawska et al., 2008). The majority of particle number from vehicle exhaust are in the size range 20-130 nm for diesel engines (Morawska et al., 1998a, b) and 20-60 nm for gasoline engines (Ristovski et al., 1998) Later, some studies found that nucleation mode particles can be either directly emitted from the vehicle exhaust in the particle phase with the composition of elemental carbon, metal species and a fraction of sulfuric acid ( $\text{H}_2\text{SO}_4$ ) and organic compounds (unburned oil, etc.) (Kittelson, 1998; Burtscher, 2005; Arnold et al., 2006; Rose et al., 2006; Rodríguez and Cuevas, 2007; Fernández-Camacho et al., 2010), or produced during the dilution and cooling of the exhaust emissions in

ambient air from cars (Charron and Harrison, 2003; Yao et al., 2005; Casati et al., 2007), aircrafts (Cheung et al., 2011) ships (Healy et al., 2009; González et al., 2011) and other combustion source like incineration (Karasev et al., 2004; Lipsky et al., 2006; Wright et al., 2007; Géhin et al., 2008; Chuang et al., 2011; Manoukian et al., 2013). All the studies indicate that the nucleation mode particles emitted from primary sources are often accompanied by high-level co-pollutants i.e., SO<sub>2</sub>, NO<sub>x</sub> and/or CO, typical of direct source emissions.

Fernández-Camacho et al., (2010) stated that vehicle exhaust emissions and new particle formation due to photo-chemical activity were the major sources of nucleation mode particles in urban area. Vehicle exhaust emissions result in high concentrations of nucleation mode particles during the morning rush hours. The highest nucleation mode particles number concentrations were recorded during the noon and afternoon, photochemical activity resulted in high O<sub>3</sub> levels and in new particle formation. Typically, NPF is favored under the conditions of low pre-existing aerosols, as their surface area serves as a condensation and coagulation sink of ambient vapors and small particles (Kulmala et al., 2004a; Neitola et al., 2011; Shen et al., 2011; Vakkari et al., 2011). As such, the elevated background concentration of aerosols in polluted locations appears to suppress the NPF. Nevertheless, the NPF was still observed in some polluted environments and most of the studies have related the NPF to the concentration of vapor-phase H<sub>2</sub>SO<sub>4</sub> which is mainly generated by the oxidation of SO<sub>2</sub> by the hydroxyl (•OH) radical during daytime (e.g., Weber et al., 1997, 1999; Jeong et al., 2004; Sihto et al., 2006; Riipinen et al., 2007; Kuang et al., 2008).

In a number of studies higher particle numbers were observed in the morning rush hour compared to the afternoon rush hour (Wahlin et al., 2001; Wehner et al., 2002; Molnar et al., 2002). Whilst direct emissions were responsible for the majority of particles smaller than 30 nm, Charron and Harrison (2003) observed no correlation between particles smaller than 30 nm and traffic counts and found that the highest concentrations of particles smaller than 30 nm were measured at the start of the rush hour. They postulated that the variation in particle surface area present could be responsible for the diurnal variation of particle number observed. The low particle number concentration prior to the morning rush hour did not provide sufficient surface area for low volatile gases, namely sulfuric acid, to condense and thus allowed the gases to nucleate and grow, whereas in the afternoon the high particle concentration promoted the condensation of these nucleating gases and so reduced particle formation. Furthermore, they observed a reasonable correlation ( $R^2 = 0.73$ ) between the decrease in nucleation events and increasing temperature.

Shi et al., (2001) showed that particles smaller than 10 nm contributed more than 36–44% of the total particle number concentration in an urban roadside location and particles within the size range 3–7 nm accounted for 37% of total measured particles. Shi and Harrison (1999) calculated that during the dilution of the exhaust binary nucleation could occur, with higher nucleation rates predicted at lower temperature and higher humidity (RH). However, these predicted rates were still about two orders of magnitude lower than the measured rates. Stanier et al., (2004a, b) compared nucleation events during summer and winter in Pittsburgh with predicted particle formation curves

based on the binary nucleation mechanism. During the study they observed nucleation occurred on between 30% to 50% of the days at much higher surface areas and lower sulfuric acid concentrations than predicted by the models, suggesting that additional factors were involved. These observations contradicted aerosol dynamics simulations (Pohjola et al., 2003) of the emission of pollutants from exhausts, that showed high concentration of particles in the plume acted as a highly effective condensational sink for sulfuric acid. In polluted environments, the extremely high concentrations of precursor gases (e.g., SO<sub>2</sub>, NH<sub>3</sub> and organics) potentially can overcome the nucleation barrier imposed by the high preexisting particle concentration. In particular, the involvement of vapor-phase H<sub>2</sub>SO<sub>4</sub> in the nucleation processes has been widely implicated due to its low vapor pressure (Curtius, 2006).

Wang et al. (2008) investigated correlations of the concentrations of gaseous sulfuric acid with freshly nucleated particles (N<sub>3-6</sub> nm) and formation rates (J<sub>3</sub> and J<sub>1.5</sub>). The power-law relationship between H<sub>2</sub>SO<sub>4</sub> concentration and N<sub>3-6</sub> or J was adopted to explore the nucleation mechanism. The exponents range from 1 to 5. More than half of the NPF events exhibit an exponent larger than 2.5. For these cases, the thermodynamic process works better to explain the nucleation events in urban atmosphere of Beijing than the activation or kinetic nucleation theories proposed as potential formation mechanisms in remote atmosphere.

### **Chapter 3: Methodology**

In order to quantify the number concentration of acidic ultrafine particles in the air, a novel iron nanofilm detector developed by Cohen et al (2004a) was improved and refined. The iron nanofilm detector is a thin iron-coated silicon chip (5 mm×5 mm×0.4 mm) with about 25 nm thick ironfilm. We assumed that each acidic particle would react with the iron, creating an elevated site or bump, on the film surface. The reaction sites are visualized by scanning the surface of the film using an AFM. Firstly, laboratory-generated acidic droplets and particles were generated and collected on the detectors to form reaction sites. The sizes and shapes of reaction spots of generated acidic particles on the detectors were scanned by AFM. The analysis method of AFM was calibrated with known size polystyrene latex particles, acidic droplets and acid-coated carbon nanoparticles to confirm the correlation between measured dimensions of reaction site by AFM and original generated particle mobility diameter sized by SMPS. In field measurement, four-week sampling was carried out in cold seasons respectively at the two sites in Hong Kong. The sampling sites include rural and urban areas such as a mountain site at Mt. Tai Mo Shan (TMS) and a roadside site at Hung Hom (HH). Two types of ultrafine particle samplers were used for ambient monitoring. One was a combined system in which an Electrostatic Precipitator (ESP) was preceded by SMPS to classify particle sizes from the air samples. The other was an ultrafine diffusion sampler (DS), which did not have specific size selectivity. The number concentrations of acidic particles and of total ultrafine particles collected by the SMPS+ESP and the DS were compared, and the total ultrafine

particle concentrations (of acidic and non-acidic particles) determined using the iron nanofilms in the SMPS+ESP and the DS were compared with those determined using the SMPS for purposes of comparison and quality control. A reliable method for the quantification of acidic ultrafine particles was validated and established. In addition, the spatial and temporal variations of number concentration and size distribution of acidic ultrafine particles in Hong Kong were investigated.

### **3.1 Preparation of iron nanofilm detectors**

Thermal Vacuum Evaporation (VE) and Magnetron Sputtering (MS) deposition are two methods commonly used for the coating of thin-layer of iron nanofilm on the silicon wafer. The iron nanofilm detectors tested in previous study (Cohen et al., 2004a) was silicon chips coated with iron by vapor deposition. However, the nanofilm detector needs to be modified and improved in this study. During the previous experiments and field study, we found that the iron film on the silicon chip was easy to detach from the support under high humidity and high temperature such as the case in Hong Kong. To enhance the adherence of the iron nanofilm on the substrates, in this study, two types of substrates were used to support the iron nanofilm. The first substrate was blank silicon chips (5mm × 5mm × 0.4mm), and the second substrate was blank silicon chips (5mm × 5mm × 0.4mm) coated with a 5 nm titanium (Ti) layer by Direct Current (DC)-MS system (ARC-12M, Plasma Science Inc., USA). Blank silicon chips were all ultrasonically cleaned in sulfuric acid solvent before coating. About 25 nm thick iron nanofilm was coated onto these two substrates by VE (Cooke Vacuum Products, USA) and

by DC - MS deposition of Fe (with purity of 99.99%) target (0.5 cm thick) in Ar (99.999%), respectively. The base pressure of the chamber was lower than  $1 \times 10^{-5}$  Pa before MS deposition and the total pressure for sputtering was kept at 1.0 Pa. Four batches of detectors, namely Fe-VE, Fe-MS, Fe-Ti-VE and Fe-Ti-MS, were obtained and stored in a nitrogen atmosphere to avoid oxidation of the iron nanofilm surface except during exposure. Fe-VE detector is same as the detector developed in Cohen's study, Fe-MS, Fe-Ti-VE and Fe-Ti-MS detectors are three new types of the iron nanofilm detectors we developed.

## **3.2 Generation of aerosol standards**

In order to obtain morphological information of acidic and non-acidic ultrafine particles on the designed iron nanofilm detectors and to calibrate the equipment such as scanning mobility particle sizer (SMPS) + condensation particle counter (CPC), electrostatic precipitator (ESP) and AFM, both standard acidic and non-acidic particles were generated and collected onto the detectors in this study. Due to different physical and chemical properties of the standard acidic and non-acidic particles, the generation procedures of each were different while the collection procedures were the same. In this study, test samples were prepared by depositing polystyrene latex (PSL) microspheres, sodium chloride (NaCl), and H<sub>2</sub>SO<sub>4</sub> particles of known diameters onto the iron nanofilm detectors.

### **3.2.1 Non-acidic particles**

Monodisperse non-acidic aerosols were produced by nebulizing solutions of NaCl or by dispersing PSL microspheres (i.e., 30, 46 and 102 nm) in Milli-Q water to minimize the concentration of impurities that may be present in tap

water. In principle, the generated particles were charge-neutralized, size-selected by differential mobility analyzer (DMA) and deposited onto the nanofilm detectors using an ESP. To generate the NaCl aerosol standards, an aerosol generator (Model 7.811, GRIMM, Germany) was used to produce submicron-sized NaCl aerosols. The aerosol production rate can be adjusted by the flows of the atomizer and the dryer (dilution air) and also the mass concentrations of NaCl solutions. To generate the PSL aerosol standards, one or two drops of PSL standard of each size were added into Milli-Q water to dilute the suspension. The PSL aerosols, generated by the atomizer and diluted using filtered room air in a 1.5 liter bottle, were dried by a silica gel dryer (40 cm long  $\times$  5cm diameter), and then were introduced into the DMA. The singly charged aerosol, leaving from the bottom of the DMA, was then guided directly onto the nanofilm detectors mounted in the ESP.

Due to significant diffusion loss of particles with size below 10 nm and diffusion broadening effect in the transfer function, it is important to understand the efficiency (or penetration rate) of the DMA for the accurate measurement of airborne particles. In this study, an experimental system determining the aerosol losses in the DMA was established using NaCl aerosol standards. In addition, the collection efficiency (or sampling performance) of the ESP and a diffusion sampler were evaluated using PSL standards. The ESP used in this study was a point-to-plane electrostatic precipitator. The diffusion sampler (DS) was another collection system with a flat and rectangular channel we developed to collect UFPs. Detailed descriptions on the calibration of the DMA, ESP and DS were given in Sections 3.3.1 - 3.3.3.

In principle, ambient acidic sulfates mainly exist in two forms: acid

dissolved in aqueous droplets and as a surface layer on solid particles, such as typical carbonaceous or fly ash particles (Ronald et al., 1983; Lippmann 1989; Radojević and Harrison 1992). The second type of aerosol is formed by adsorption of sulfuric acid onto particles with large surface to volume ratio (Zhang et al., 2008). The detailed descriptions about the generation of acidic particles are shown as follows.

### **3.2.2 Acidic droplets**

To generate the acidic droplet standards, an aerosol generator (Model 7.811, GRIMM, Germany) was used to produce submicron-sized acidic droplets. The aerosol production rate can be adjusted by the flows of the atomizer and the dryer (dilution air). In this study, purified air with a flow rate of 4.8 l/min was introduced into the atomizer to generate polydisperse aerosols. Dilution air was added into the system at the exit of the generator with a flow rate of 10 l/min. Six sulfuric acid solutions with different concentrations (in H<sub>2</sub>SO<sub>4</sub> (w)/H<sub>2</sub>O(v)), i.e., 0.09 g/cm<sup>3</sup>, 0.045 g/cm<sup>3</sup>, 0.009 g/cm<sup>3</sup>, 0.0018 g/cm<sup>3</sup>, 0.00036 g/cm<sup>3</sup> and 0.000072 g/cm<sup>3</sup> were prepared to condition the droplets. The H<sub>2</sub>SO<sub>4</sub> droplets were generated from each solution using the aerosol generator. For each solution, three different sizes, i.e., 32.5, 75.4 and 124.5 nm of H<sub>2</sub>SO<sub>4</sub> droplets were selected by a SMPS (Model 5.400, GRIMM, Germany) separately, and each size of H<sub>2</sub>SO<sub>4</sub> droplets was collected onto three detectors using an ESP (Model 5.561, GRIMM, Germany) with a steady voltage of 5000 v, respectively. The sampling flow rate of the ESP (0.3 l/min) was controlled by a CPC (Model 5.400, GRIMM, Germany). In this study, the sizes of the generated acidic droplets represented the electrical mobility diameter (D<sub>p</sub>) measured by the SMPS, which meant the diameter of a sphere

with the same migration velocity in a constant electric field as the particle of interest (Flagan, 2001).

### **3.2.3 Acid-coated particles**

For the generation and collection of the submicron sulfuric acid-coated standard particles, a schematic diagram of the experimental system is shown in Figure 3.1. The system consisted of a nano-carbon particles generator, an H<sub>2</sub>SO<sub>4</sub> aerosol evaporation and condensation system, a SMPS, an ESP and a CPC. Firstly, a large quantity of glucose aerosols were generated from D(+) Glucose monohydrate (Farco chemical) solution (5g/100ml H<sub>2</sub>O) by an ultrasonic nebulizer (Model No.402A1, China), and were introduced into a quartz tube furnace which was heated to 700°C (Model No.F21130-33, Barnstead Thermolyne, U.S.A). At high temperature, without sufficient oxygen supply for combustion, the glucose aerosols underwent thermal decomposition, and produced ultrafine carbon particles. These generated carbon particles were diluted by air immediately in two conical flasks and then at a flow rate of 0.5 l/min passed over the surface of highly pure H<sub>2</sub>SO<sub>4</sub> (98% w/w) heated on a wire coil heater. The mixture of carbon particles and sulfuric acid vapor then passed through a thermostated water-cooled condenser to form nearly monodisperse sulfuric acid-coated aerosol. Ultimately, the generated acid-coated aerosol was classified by the SMPS and deposited onto the detectors mounted in the ESP with a flow rate of 0.3 l/min. Excess acid-coated aerosols (0.2 l/min) were absorbed by a H<sub>2</sub>O solution through the bypass between the condenser and the SMPS. In this study, we used this H<sub>2</sub>SO<sub>4</sub> coated aerosol generation system to produce six different sizes of acid-coated nanoparticles, namely 20.7, 32.5, 51.5, 75.4, 101.4 and 153.9 nm. The coated

H<sub>2</sub>SO<sub>4</sub> amount on particles was proportional to the exposure time, vapor concentration of H<sub>2</sub>SO<sub>4</sub>, and particle surface area (or particle size) (Zhang et al., 2008). According to H<sub>2</sub>SO<sub>4</sub> condensation results in this study and the results of Zhang et al., (2008), H<sub>2</sub>SO<sub>4</sub> acid accounted for a fraction of 64.7%, 44.5%, 27.8%, 19.2%, 14.3%, and 9.5% of the mass of the six size particles, respectively. These different size acidic standards were collected on six detectors, respectively.

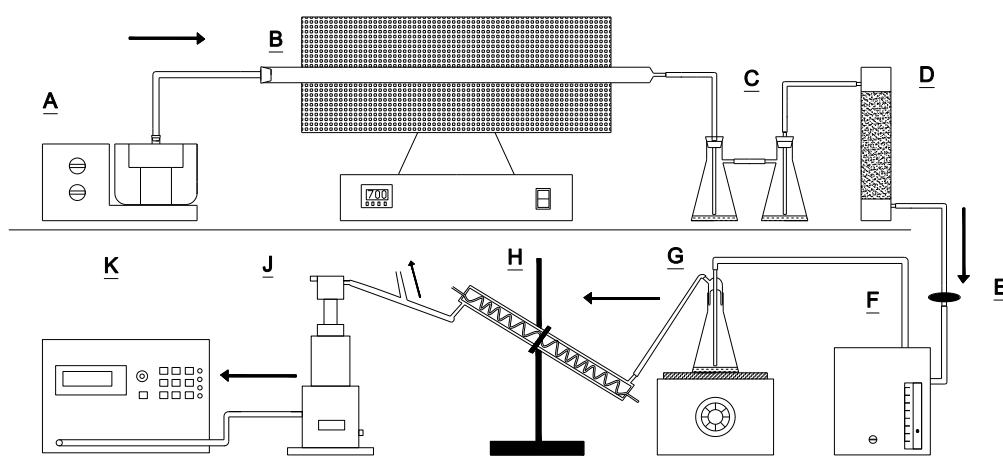


**Figure 3.1** The schematic of acid-coated nano-particles generation and collection system. Note: **A** is the ultrasonic nebulizer; **B** is the quartz tube furnace; **C** are two conical flasks with purified water for cooling gas and removing large size particles preliminarily; **D** is the silicone gel dryer to absorb the water mist; **E** is the filter to remove the particles with a size larger than 1 μm; **F** is a pump (0.5 l/min flow rate) to draw the carbon nano-particles to G; **G** is the conical flask with highly pure H<sub>2</sub>SO<sub>4</sub> for the generation of sulfuric acid vapour on a heater; **H** is the water-cooled condenser; **I** is SMPS+ESP; and **K** is CPC.

### 3.3 Calibration of instruments

#### 3.3.1 SMPS + CPC calibration

In this study, an experimental system determining the aerosol losses in the DMA was established. The efficiency of the DMA is closely related to particle

size and air flow rate. A flow rate of 0.3 l/min was fixed for the set of SMPS + CPC.

A theoretical curve between particle size and penetration rate of the SMPS system (model 5.400 GRIMM, Germany) was provided by the manufacturer (blue diamonds in Figure 3.2). To check whether it is correct, an experimental system determining the aerosol losses in the DMA was established. The polydisperse sodium chloride (NaCl) aerosol with constant size distribution and number concentration was generated and introduced into the first DMA analyzer (Model 3071, TSI, USA) to obtain classified monodisperse NaCl aerosols. The first DMA was operated at a fixed voltage for each run to obtain monodisperse aerosols with a known size. The classified monodisperse NaCl particles at each size were then measured by SMPS+CPC and only CPC, respectively. Subsequently, the number concentrations of particles with 38 different aerodynamic diameter channels at the inlet and outlet of the second DMA were measured. Based on the measured penetration rate  $P$ , the effective tube length ( $L_{eff}$ ) of the DMA was obtained by using the equations below (Sonderholm, 1979):

$$P=0.82 \times \exp(-11.5 \mu) + 0.10 \times \exp(-70.0 \mu) + 0.03 \times \exp(-180 \mu) + 0.02 \times \exp(-340 \mu) \quad (\mu \geq 0.007) \quad 3.1)$$

$$P=1-5.5 \times \mu^{2/3} + 3.77 \times \mu \quad (\mu < 0.007) \quad 3.2)$$

$$\mu=(D \times L_{eff})/q \quad 3.3)$$

where,  $D$  is the diffusion coefficient of the particle ( $\text{cm}^2/\text{sec}$ ),  $q$  is volume flow rate ( $\text{cm}^3/\text{sec}$ ), and  $\mu$  is the deposition parameter.

In this study, the penetration rate of the SMPS was determined by the ratio of the measured particle number concentrations at the outlet to the number

concentrations at the inlet for each size of particles with a range of 9-350 nm, as shown in Figure 3.2 (black dots). It can be seen that the theoretical curve overestimated the penetration rate of the SMPS for smaller particles (i.e., 5-15 nm) and underestimated for larger particles (i.e., 50–350 nm). The experimental data in this study fit the theoretical curve very well for particle sizes between 15 and 50 nm.

In a good approximation, the measured penetration rate  $P$  of aerosol with a given size is the function of diffusion constant  $D$  through a circular tube of length  $L$  at a volume flow rate  $q$ . Based on the experimental data, the effective tube length ( $L_{eff}$ ) of the DMA was calculated using the equations 3.1) – 3.3) and found to be 800 cm. Using  $L_{eff}$  as a free parameter, for the sampling flow rate  $q = 0.3$  l/min, the best fit was received in the particle size range from 10 to 350 nm when  $L_{eff} = 800$  cm (Figure 3.2). The derived effective length  $L_{eff}$  is useful to determine the particle losses for each individual particle size.

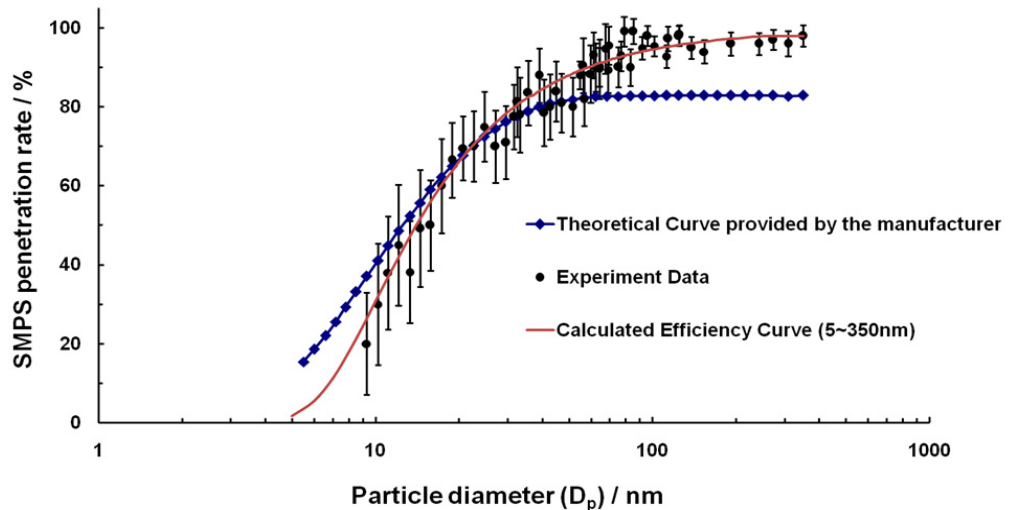


**Figure 3.2** Relationship between particle size and penetration rate of the SMPS; the error bars represent the standard deviations (SD) of the measurements

### 3.3.2 Collection efficiency of ESP

In this study, monodisperse polystyrene latex (PSL) microsphere standards with diameters of 30, 46 and 102 nm were used to evaluate the collection efficiency (or sampling performance) of the EPS. Due to the uniform particle deposition of the ESP, confirmed in previous experiments (Dixkens and Fissan, 1999), twenty areas of  $100 \mu\text{m}^2$  of each detector among those exposed detectors were randomly scanned by the AFM to size and number the three PSL microsphere standards, respectively.

The singly charged aerosol, leaving a DMA, was guided by a duct into the ESP, where perpendicular to the aerosol flow, an electrode with a flat round plate (20 mm in diameter) was fixed downstream a distance of 150 mm to the inlet. The detector i.e., silicon chip ( $5\text{mm} \times 5\text{mm} \times 0.4\text{mm}$ ) coated with iron nanofilm was mounted on the plate by double-sided tapes to collect the particles. It is noteworthy that a DMA was used prior to the ESP. This is due to the fact that DMA can charge particles using a bipolar charger (neutralizer) with radioactive sources, i.e., Am241, and the charged particles are easier than uncharged particles to migrate to and are collected on a plate with the opposite charge in the electrical field.

By comparing the average number of PSL particles deposited on the detectors with the number concentration of the PSL microspheres at the inlet of the SMPS for each of the three sizes, the deposition efficiency of the ESP was determined to be  $86 \pm 11\%$  for 100 nm PSL,  $80 \pm 16\%$  for 50 nm PSL, and  $74 \pm 19\%$  for 30 nm PSL standards.

Collection efficiency and deposition pattern obtained from numerical model and experiments are available for the slightly different original design of the

ESP (Dixkens and Fissan, 1999). For the original design, singly charged particles were deposited homogeneously in the centre of the sample plate in the ESP for particles smaller than 220 nm with a flow rate of 0.3 l/min and a voltage of 25 kV, and the collection efficiency reached 100%. Compared to the results obtained by Dixkens and Fissan (1999), the lower efficiency measured in this study was mainly caused by the count-associated uncertainties from the AFM. The statistical bias in calculations derived from the AFM counting on the detectors appeared to underestimate the collection efficiency of the ESP.

### **3.3.3 Collection efficiency of DS**

The DS was made of stainless steel with a flat and rectangular channel with 1.0 mm height, 50 mm width and 500 mm length. The size of the DS inlet was 1×50 mm (H×W), and the diameter of the outlet was 10 mm. The DS had nine rectangular recesses (L×W×H: 7×7×0.4 mm) comprising three groups, and each rectangular recess could hold one detector (L×W×H: 5 ×5 ×0.4 mm, see Figure 3.3, brown area). The locations of the three groups of rectangular recesses were at 7.0, 201.5, and 472.5 mm (midpoint of the rectangular recess) from the inlet along the length of the channel, respectively (see Figure 3.3, blue area). The L1~L2, L3~L4 and L5~L6 were the distances of left and right sides of iron nanofilm detectors from the inlet at the three locations respectively. Air was drawn through the DS by a low-flow pump. Air leakage was avoided by sealing the channel with a layer of rubber (see Figure 3.3, solid black area) and the channel was fastened with screws in the contact areas.

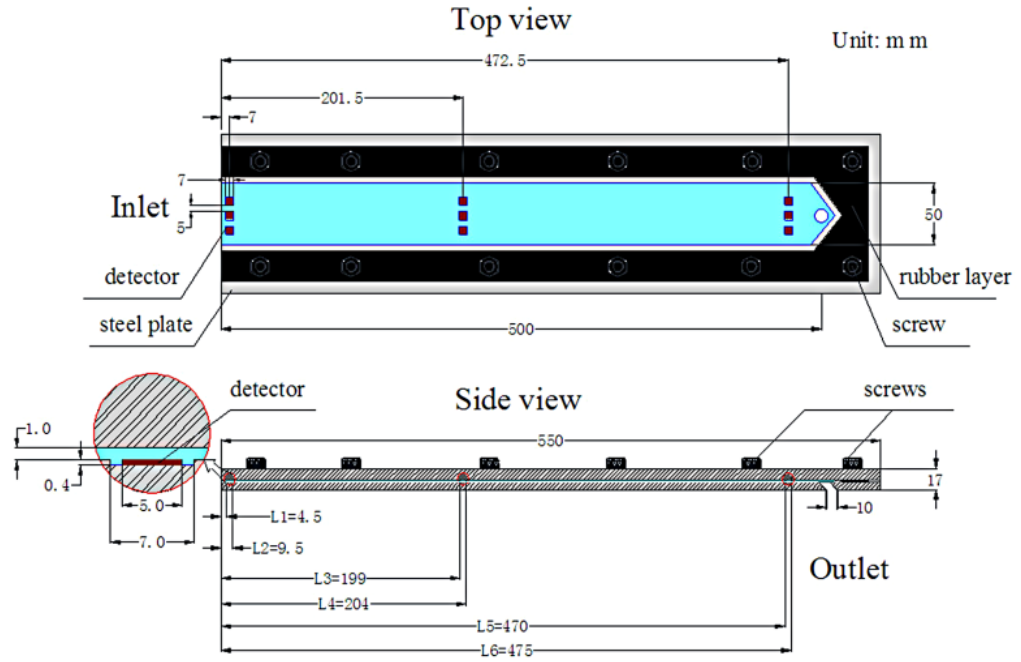


**Figure 3.3** Schematic diagram of the DS. Three sets of blank detectors were placed along the channel at different distances from the DS inlet.

The theoretical calculation and experimental calibration were conducted and combined to evaluate the deposition efficiency of particles in DS. The theoretical calculation of the deposition efficiency is dependent upon the theory of diffusion presented by Hinds (1999) for a parallel-plate diffusion battery which has rectangular channels. The theoretical deposition efficiency ( $\eta$ ) of particles through rectangular channels given by Hinds (1999) is shown as follows:

$$\eta = 2.96 \times \mu^{\frac{2}{3}} - 0.4 \times \mu \quad (\mu < 0.003) \quad 3.4)$$

$$\eta = 1 - 0.910 \times e^{-7.54\mu} - 0.0531 \times e^{-85.7\mu} - 0.0153 \times e^{-249\mu} \quad (\mu \geq 0.003) \quad 3.5)$$

$$\mu = \frac{D \times L \times W}{Q \times h} \quad 3.6)$$

$$D = \frac{k \times T \times C_c \times 10^{10}}{3\pi \times \gamma \times d_p} \quad 3.7)$$

where  $\mu$  is the deposition parameter,  $L$  is channel length (cm),  $W$  is channel width (cm),  $Q$  is flow rate (cm<sup>3</sup>/sec), and  $h$  is channel height (cm),  $D$  is the diffusion coefficient of the particle (cm<sup>2</sup>/sec) and is determined by the Stokes-Einstein equation here,  $k$  is Boltzmann's constant ( $1.38 \times 10^{-23}$ ),  $T$  is the absolute temperature,  $C_c$  is the slip correction factor,  $\gamma$  is the air viscosity ( $1.79 \times 10^{-6}$  Pa·sec), and  $d_p$  is the particle diameter ( $\mu\text{m}$ ).

Since the numbers counted on the iron nanofilm detectors at different locations in the DS were utilized to calculate the ambient particle number concentration, the deposition efficiencies of particles at three different locations (i.e., L1~L2, L3~L4 and L5~L6) firstly need to be determined. Different from the total deposition efficiencies  $\eta$ , the deposition efficiencies of particles at three different locations in DS, namely  $\Delta\eta_a$ ,  $\Delta\eta_b$  and  $\Delta\eta_c$ , were determined by stepwise calculations of  $\eta_{L2}-\eta_{L1}$ ,  $\eta_{L4}-\eta_{L3}$  and  $\eta_{L6}-\eta_{L5}$ , respectively, using the equations 3.4 – 3.7) (Figure 3.3). Here,  $\eta_{L1}$ ,  $\eta_{L2}, \dots$ , and  $\eta_{L6}$  represent the deposition efficiency along with the channel length of L1, L2..., and L6, respectively.

Furthermore, to validate and/or calibrate this theoretical calculation for DS, the deposition efficiencies of particles at each of the three different locations were experimentally determined with PSL microsphere standards with diameters of 32, 46 and 102 nm (Duke Scientific Corp., USA), respectively. The PSL aerosols were generated and introduced into an environmental chamber with controlled temperature and relative humidity (RH). Every two hours 5 ml PSL-particle aqueous solution was added into the particle generator to keep the generated aerosol at a stable level of about  $10^3$ - $10^4$ /cm<sup>3</sup>. The chamber size was 120 (H)  $\times$  110 (W)  $\times$  100 (L) cm. Three diffusion samplers

were placed in the centre of the chamber (see Figure 3.4). PSL microspheres were well mixed in the chamber using a fan and the total PSL aerosol concentration was remained at a stable level of about  $10^3$ - $10^4/\text{cm}^3$ , i.e., about  $4.0 \times 10^4/\text{cm}^3$  for 32 nm,  $1.0 \times 10^4/\text{cm}^3$  for 46 nm and  $1.0 \times 10^3/\text{cm}^3$  for 102 nm PSL particles. PSL particles were generated continuously for 8 hours each day. To achieve the sufficient particle loading in DS for statistical analysis (approximately 50-100 particles in a  $100 \mu\text{m}^2$  scanned area), total 48 or 72 hours were required for sampling of 32 and 46 nm PSL particles in the environment where the particle concentration was in an order of magnitude  $10^4$  particles/ $\text{cm}^3$ , and over 150 hours was needed for sampling of 102 nm PSL particles in the environment with the PN concentration in an order of magnitude  $10^3$  particles/ $\text{cm}^3$ . Simultaneously, a SMPS+CPC measured and recorded the PSL particle concentration from the inlet of DS ( $C_{\text{in}}$ ,  $\text{cm}^{-3}$ ) for monodisperse PSL aerosols (32nm, 46nm and 102nm) every 4 min throughout the entire sampling period. Experiments for the deposition efficiency of each size PSL particle were conducted with six different flow rates  $Q$  (i.e., 0.02, 0.03, 0.1, 0.3, 0.6 and 1.2 L/min), and each experiment was tested three times. After sampling, all detectors sampled at three different locations in the DS were scanned and counted by the AFM for three different PSL microspheres and six flow rates (total 18 different scenarios), respectively. For each detector location, the total deposited particle number  $N$  was calculated by the equation:  $N=2.5 \times 10^5 \times \sum n$ , where  $n$  is the number of particles in each counted  $100 \mu\text{m}^2$  surface area by AFM; the constant ( $2.5 \times 10^5$ ) represents that there were  $2.5 \times 10^5$  of  $100 \mu\text{m}^2$  surface areas at the location for particle collection.  $\Delta\eta'$  at the three different locations were calculated by  $N/(C_{\text{in}} \times Q \times \text{sampling time})$ .

Consequently, the experimentally determined deposition efficiency of the particles at these three locations (namely  $\Delta\eta_a'$ ,  $\Delta\eta_b'$  and  $\Delta\eta_c'$ ) were utilized to compare with the theoretical predicted values. Detailed results are provided in Chapter five.

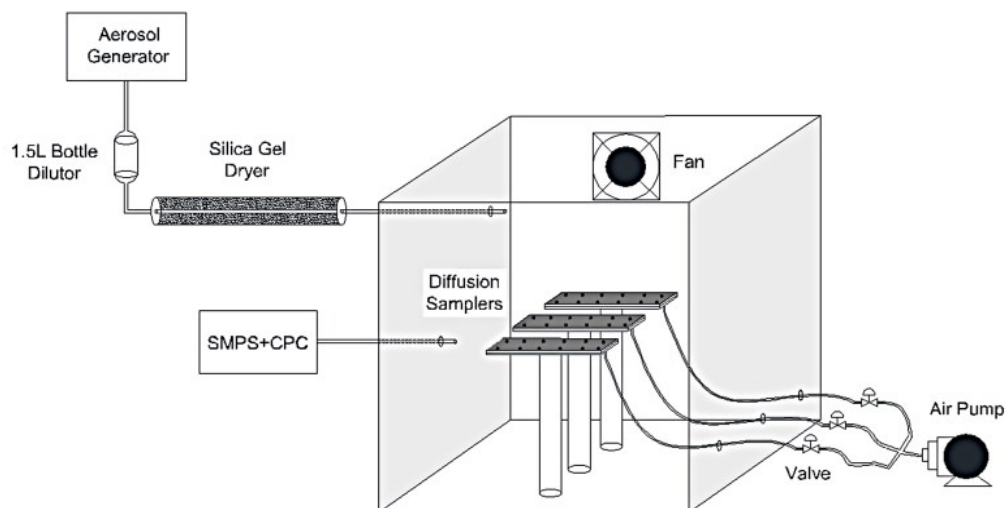


**Figure 3.4** Schematic of the experimental setup. The controlled air exchange rate, temperature and relative humidity of the chamber were around  $0.4 \text{ h}^{-1}$ ,  $20^\circ\text{C}$  and 50%, respectively.

### 3.3.4 AFM calibration

In this study, the tapping mode of an AFM (NanoScope, Version 5.31R1, Veeco Instrument Inc., USA) was used to scan the acidic ultrafine particles or droplets collected on the iron nanofilm detectors. The PSL microsphere standards, acidic droplet standards and acid-coated standard particles generated in Section 3.2 were used to calibrate the AFM. In this study, tapping mode of the AFM was used with a 5778E scanner. The oscillating probe tip in sharp pyramidal shape (ACT Series Probe) was used with a height of 14-16  $\mu\text{m}$  and the nominal radius of curvature less than 10 nm. Scan parameters were established based on scan area and the imaging resolution of particles on the

detectors.  $5\mu\text{m} \times 5\mu\text{m}$  areas on a detector at 512 sample line were selected for scanning with the parameters set as follows: scan rate: 0.6~0.8Hz; amplitude setpoint: 0.65~0.80V; integral gain: 0.2; and proportional gain: 0.5. With the use of these scan parameters, AFM was calibrated with known size PSL particles to define the AFM x, y, z-axis measurement accuracy which was mainly influenced by convolution of the pyramidal tip or the scanner sensitivity, while laboratory-generated acidic droplets and acid-coated carbon nanoparticles were used to confirm the correlation between measured dimensions of reaction sites and originally generated particle mobility diameter ( $D_p$ ) sized by the SMPS.

Actually, in the initial stage of this study, the AFM and a field emission scanning electron microscopy (FESEM) (JEOL-JSM 6335F, JEOL Ltd., Japan) were compared to verified that the AFM is more suitable and effective for the detection of acidic ultrafine aerosols due to the fact that AFM can detect ultrafine particles with high-quality three-dimensional imaging, and can be operated at ambient pressure. Figures 3.5 and 3.6 present the FESEM and AFM scanning images of the reaction spots generated by acidic droplets and  $\text{H}_2\text{SO}_4$ -coated carbon nanoparticles on the iron nanofilm detectors.

It can be seen that the images of the reaction spots from FESEM scanning were unclear for weak acidic droplets (See Figure 3.5a) and acid-coated particles with size smaller than 100 nm (See Figure 3.5b), due to the colorless contrast on the acid reaction spots to un-reacted surface. In contrast, the AFM, designed to detect angstrom scale elevations, easily visualized slight deformation of individual ultrafine acidic particles (See Figure 3.6a). Moreover, for  $\text{H}_2\text{SO}_4$ -coated carbon particles, their deposition on the detectors

created clear and recognizable reaction sites, namely a particle in the centre surrounded by elevated halos, as shown in Figure 3.6b. The results indicate that the AFM is more suitable than FESEM for the enumeration and sizing of the reaction spots formed by acidic ultrafine particles.

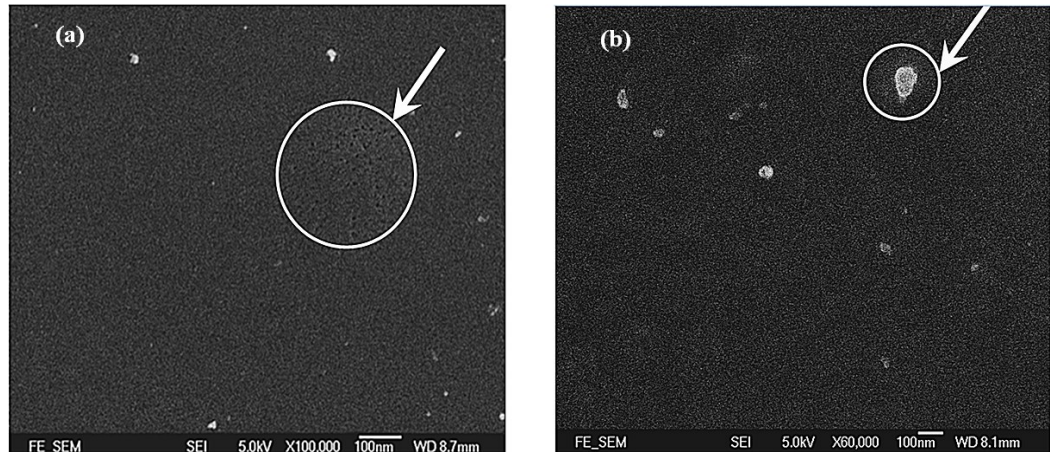


**Figure 3.5** Acidic droplets and particles on the iron nanofilm detectors scanned by FESEM; (a) A 100 nm  $(\text{NH}_4)\text{HSO}_4$  droplet; (b) A 100 nm  $\text{H}_2\text{SO}_4$ -coated carbon particle

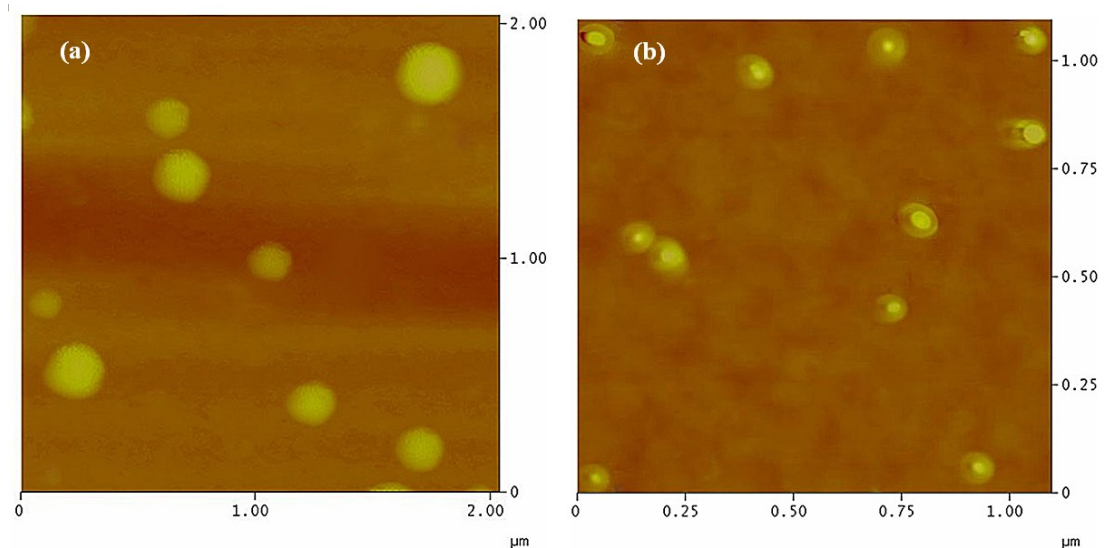


**Figure 3.6** Acidic droplets and particles on the iron nanofilm detectors scanned by AFM; (a) 100 nm  $(\text{NH}_4)\text{HSO}_4$  droplets; (b) 51.5 nm  $\text{H}_2\text{SO}_4$ -coated carbon particles

### **3.4 Performance tests of detector**

#### **3.4.1 Response to humidity and temperature**

A control experiment was conducted to investigate the stability of the iron nanofilm surface of these four types of detectors under extreme weather conditions of high relative humidity (RH) and high temperature, and to study the adhesive strength of the iron nanofilm on the substrate with and without coating Ti layer. Blank detectors and a set of detectors that were previously exposed to H<sub>2</sub>SO<sub>4</sub> standard aerosols were placed in a container (desiccator) wrapped with a rubber belt heater to control temperature and RH for 3 months. The RH and temperature were set: i) 90% and 20°C; and ii) 85% and 35°C. These two weather conditions are often observed in subtropical Hong Kong.

#### **3.4.2 Response to gaseous pollutants**

To test whether gas-phase pollutants in the atmosphere affect the surface of the iron nanofilm detectors, a set of blank detectors were placed in a sealed plastic canister (height: 5 cm; diameter: 8 cm) with an inlet installed with a high-efficiency particle filter (HEPA) (Whatman, 0.3- $\mu$ m pore size) to remove ambient particles. The diameter of the inlet and outlet was 0.5 cm. Particle-free air was pumped through the canister with a flow rate of 30 cm<sup>3</sup>/min for the duration of the sampling period at a mountain site, i.e., Mt. Tai Mo Shan (TMS) (see Section 4.4). The exposed detectors were scanned by AFM each week to check the impact of gaseous pollutants.

## **3.5 Field Measurements**

### **3.5.1 Sampling sites**

To assess the reliability and efficiency of the detectors and samplers, and to quantify the number concentrations of acidic ultrafine particles in different areas of Hong Kong, one rural site and an urban site were chosen for field measurements. The rural site was located at Mt. Tai Mo Shan (TMS) and the urban site was located at Hung Hum. The field measurement was conducted at Mt. TMS from 06 September to 30 November in 2010. Another field measurement was conducted at the HH site from 22 December 2010 to 15 January in 2011.

#### **3.5.1.1 Rural site - Mt.TMS**

Mt. TMS is claimed to be Hong Kong's most misty area due to the high daily cloud coverage. The highest point on Mt. TMS is occupied by a Hong Kong Observatory weather radar station. Our monitoring site was located at the waist of Mt. TMS near the mountain summit (22.405°N, 114.118°E, about 640 m a.s.l.) (see Figure 3.7). Surrounding the foot of the mountain are urban centers with a population of 2.23 million. The straight distances between the mountain summit and the urban centers at the foot are about 5-10 km. Farther to the south are the urban centers of the partial New Territory, Kowloon peninsula and Hong Kong Island. To the southwest is the newly-developed residential area of Tung Chung, the international airport and the South China Sea. To the west are the Tuen Mun residential areas and to the south is the South China Sea. To the north and northeast are the city clusters of the inland

Pearl River Delta (PRD) region. The prevailing north/northeast synoptic winds in October – November bring polluted air on some days and clean air on some other days from inland PRD and eastern China coast to the sampling site, depending on the weather conditions at upwind locations.

### **3.5.1.2 Urban site - Hung Hom**

This sampling site was on the rooftop of a building in the campus of Hong Kong Polytechnic University at Hung Hom, Kowloon (22.3° N, 114.177° E, about 40m a.s.l) (Figure 3.7). This site was significantly affected by heavy traffic as it was located near main roads and cross-harbor tunnel (CHT), about 50 m away from the Hong Chong Road (about 30 m wide) with four lanes in each direction. The daily average number of vehicles passing through the CHT was about 122,000 in December 2010 - January 2011, of which, about 30% were diesel-fuelled vehicles, 60% gasoline-fuelled vehicles, and 10% liquefied petroleum gas (LPG)-fuelled taxis (HKTD, 2010&2011). The traffic peaks appear at 08:00 - 09:00 in the morning and 17:00 - 18:00 in the afternoon and evening (Xia and Shao, 2005; Cheng et al., 2012). To the northeast of the sampling site, there are two funeral parlors with a distance of ~500 m. To the southwest and southeast is the Victoria Harbour. Hence, the study area could be affected by traffic emissions, incineration from the funeral parlour and marine vessel emissions (Figure 7.1 in Section 7.1).

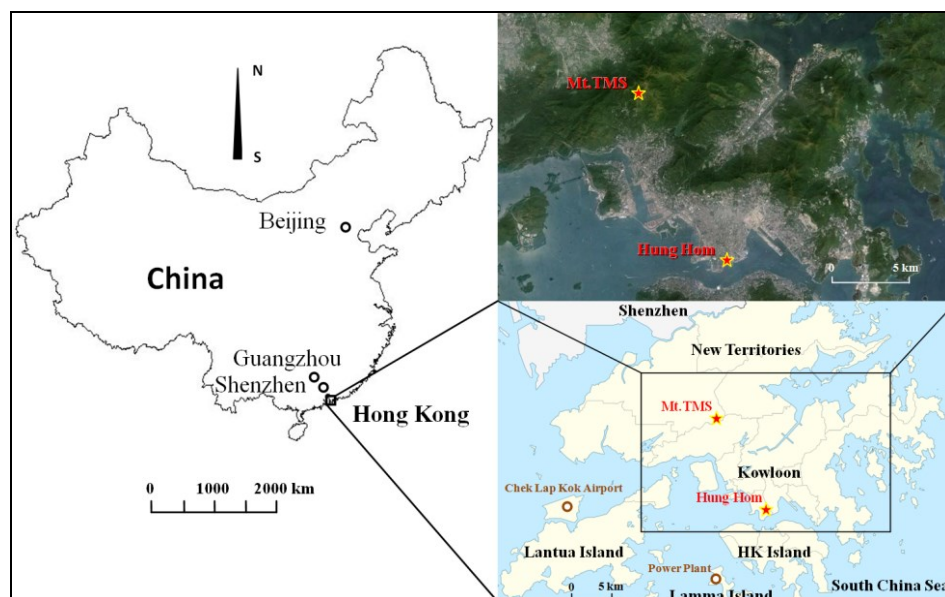


**Figure 3.7** Locations of Hong Kong and the sampling sites.

### 3.5.2 Sampling techniques

**SMPS+CPC:** Particle size distributions in the range of 5.5 to 350 nm were continuously measured by a Scanning Mobility Particle Sizer (SMPS, model 5.400, GRIMM, Germany) and a Condensation Particle Counter (CPC, model 5.400, GRIMM, Germany) system with 44 size bins at 4-min scan intervals. The SMPS was equipped with a nano-differential mobility analyzer (DMA), which separated poly-disperse particles into selected mono-disperse particles according to the electrical mobility of the particles, a function of their size. Then the CPC counted the number concentration of mono-disperse particles by laser light scattering. A sample air flow rate of 0.3 l/min was fixed for the set of SMPS + CPC with a sheath air flow rate of 3.0 l/min. In order to control the relative humidity (RH) during sampling campaign, the aerosol samples taken from ambient air have been dried with a 0.6 m long diffusion silica gel

drier (GRIMM) before entering the sampling system. Meanwhile, the sheath air in DMA was dried with a sheath-air dryer (GRIMM). To minimize the particle loss, ambient aerosols were drawn into the SMPS+CPC system through a 1 m long flexible and conductive tube with an inner diameter of 0.8 cm. Due to significant diffusion loss of particles with size below 10 nm and diffusion broadening effect in the transfer function, it is important to understand the efficiency (or penetration rate) of the DMA for the accurate measurement of airborne particles. An experimental system determining the aerosol losses in the DMA and the calibration of the SMPS was established and discussed in Section 3.3.1. In addition, since the Grimm CPC is not widely used, the discrepancy between Grimm CPC and TSI CPC reported by Schlatter (2006) was used to compare our results with other studies. The CPC counting efficiency and particle diffusion losses in the tubing were taken into account in the data analysis. During all sampling sessions, the SMPS+CPC was deployed to provide size-classified particle counts for comparison with the total ultrafine particle counts determined with the SMPS+ESP and DS. It is noteworthy that sizing by AMF is based on particle topography and is different from sizing by SMPS, which is based on electrical mobility. The relationship between particle diameters measured by SMPS and their width/height measured by AFM are calibrated prior to the comparison of size-classified particle number concentrations.

**SMPS+ESP:** Ambient particles were classified and collected on a set of four detectors using a SMPS and an ESP (ESP, model 5.561, GRIMM, Germany) with a steady high voltage of 5000v at the sampling site. The sampling flow rate of the ESP was 0.3 L/min.

**DS:** Nine iron nano-film detectors were placed inside the DSs for exposures for three or seven days (the exposure duration depended on the ambient level of ultrafine particles). The deposition efficiency depended on the distance from the inlet and the flow rate. A 0.03 L/min flow rate was used in the field sampling. The whole DS system was placed in an outdoor storage room to protect the DS and pump from rain and to decrease the influence of air turbulence on DS sampling. The storage room had a rectangular hole on the wall. The inlet of DS was horizontally placed very close to the hole. To avoid the impact of unsteady winds during the field measurement, isokinetic sampling was considered to allow the sample stream to enter without changing speed.

**AFM:** The detectors collected by DS were topographically analyzed by AFM to enumerate the acidic particles and size the acidic reaction spots. Tapping mode of the AFM was used with a 5778E scanner. The detailed description about the scale of cantilever tip, scan parameters set and  $x,y,z$ -axis calibration for AFM was provided in Section 3.3.4. For each AFM image of the substrate surface, data scale was adjusted, and the offset and contrast were modified to ensure that all scanned particles were detected. Then AFM images were analyzed using the function of section and particle analysis in AFM software to count and size the particles in the scanned area. Based on our laboratory experiments, the relationship between non-acidic particles with known diameters and their width/height measured by AFM, and the relationship between acidic particles with known diameters and the AFM measured width/height of reaction spots caused by corresponding acidic particles were obtained. For example, the width of the reaction spots formed on the iron

nanofilm detectors was approximately three times the diameter of the corresponding acidic particles, while the height of the reaction spots was about one third the diameter of the corresponding acidic particles. Based on the ratios of AFM-measured size to diameter of corresponding particles, the total and acidic airborne particles' sizes were obtained and categorized into 44 bins to match those used by SMPS. Airborne particle number size distributions of total and acidic particles were derived from the particle counts in each of the 44 size bins, according to the known deposition efficiency of particles in different sizes. Consequently, the integrated total particle number and size distribution measured by DS + AFM method were compared with continuous data obtained from SMPS + CPC to evaluate the performance of the DS.

***Trace Gases:*** Instruments were installed in a room of the building, beneath the rooftop. Ambient air samples were drawn through a 5m long perfluoroalkoxy (PFA) Teflon tube (OD: 12.7 mm; ID: 9.6 mm). The inlet of the sampling tube was located 2 m above the rooftop of the building. The other end of the sampling tube was connected to a PFA manifold with a bypass pump drawing air at a rate of 5 L min<sup>-1</sup>. The intake of the analyzers for O<sub>3</sub>, CO, SO<sub>2</sub> and NO-NO<sub>2</sub>-NO<sub>x</sub> was connected to the manifold. A detailed description of the in-situ measurements of O<sub>3</sub>, CO, SO<sub>2</sub>, and NO-NO<sub>2</sub>-NO<sub>x</sub> is given below:

Ozone (O<sub>3</sub>) was measured using a commercial UV photometric instrument (Advanced Pollution Instrumentation (API), model 400E) that had a detection limit of 0.6 ppbv. The analyzer was calibrated by a transfer standard (TEI 49PS) prior to the field studies.

Sulfur dioxide (SO<sub>2</sub>) was measured by a pulsed UV fluorescence (API, model 100E), with a detection limit of 0.4 ppbv and 2- $\sigma$  precision of 0.5% for ambient levels of 50 ppbv (2-min average).

Carbon monoxide (CO) was measured with a gas filter correlation, nondispersive infrared analyzer (API, Model 300E) with a heated catalytic scrubber (as purchased) to convert CO to carbon dioxide (CO<sub>2</sub>) for baseline determination. Zeroing was conducted every 2 h, each lasting 12 min. The 2-min data at the end of each zeroing were taken as the baseline. The detection limit was 30 ppbv for a 2-min average. The 2s precision was about 1% for a level of 500 ppbv (2- min average) and the overall uncertainty was estimated to be 10%.

Nitric oxide and NO<sub>x</sub> were detected with a chemiluminescence NO-NO<sub>2</sub>-NO<sub>x</sub> analyzer (API, Model 200E). The analyzer had a detection limit of 0.4 ppbv. The Model 200E is a single chamber, single photomultiplier tube design which cycles between the NO, NO<sub>x</sub>, and zero modes. The addition of the zero mode provides excellent long term stability and extremely low minimum detectable limits.

All the SO<sub>2</sub>, CO, and NO-NO<sub>x</sub>-NO<sub>2</sub> analyzers were calibrated daily by injecting scrubbed ambient air (TEI, Model 111) and a span gas mixture. A NIST-traceable standard (Scott-Marrin, Inc.) containing 156.5 ppmv CO ( $\pm$  2%), 15.64 ppmv SO<sub>2</sub> ( $\pm$  2%), and 15.55 ppmv NO ( $\pm$  2%) was diluted using a dynamic calibrator (EnviroNics, Inc., Model 6100). For the O<sub>3</sub>, SO<sub>2</sub>, NO and NO<sub>x</sub> analyzers, a data logger (Environmental Systems Corporation, Model 8816) was used to control the calibrations and to collect data, which were averaged to 1-min values.

***Volatile organic compounds (VOCs ) and carbonyl compounds:*** To investigate the potential associations of individual VOCs and carbonyl compounds with NPF and particle growth, non-methane hydrocarbons (NMHCs) and carbonyl samples were collected on O<sub>3</sub> episode days (O<sub>3</sub> ≥ 90 ppbv), based on the prediction of meteorological conditions and the review of the PN concentrations on previous days, which were usually related to strong solar radiation, cool and dry air, and low number concentrations of pre-existing large size particles. Ambient VOC samples were collected using cleaned and evacuated 2-L electro-polished stainless steel canisters. A flow-controlling device was used to collect 1-h integrated samples. Hourly samples were consecutively collected from 0900 to 1600 with additional samples collected at 0000, 0300, 0700, 1800 and 2100 per day. Finally, 91 VOC samples were collected only at Mt.TMS on the eight days.

Carbonyl samples were collected on the same sampling days using the silica cartridges impregnated with acidified 2,4-dinitrophenylhydrazine (DNPH). Air samples were drawn through the cartridge at a flow rate of 0.8–0.9 L min<sup>-1</sup> for 120 min (2 hours); the flow rate through the cartridges was monitored with a rotameter which was calibrated before and after each sampling. An O<sub>3</sub> scrubber was connected to the inlet of the DNPH–silica cartridge to prevent interference from O<sub>3</sub>. During these sampling days, carbonyls samples were consecutively collected from 0700 to 2100 every two hours with additional samples collected at 0000 and 0300. Finally, 70 carbonyl samples were collected during this sampling period. All cartridges were stored in a refrigerator at 4°C after sampling. The sampled carbonyl cartridges were eluted slowly with 2 ml of acetonitrile into a 2-ml volumetric flask. A 20-μl

aliquot was injected into the high performance liquid chromatography (HPLC) system through an auto-sampler. The operating conditions of the HPLC and the quality control and detection limit for carbonyl compounds are also provided in Guo et al., (2009).

***Meteorological parameters:*** In addition to the above chemical measurements, several meteorological conditions were continuously monitored using a mini-weather station (Vantage Pro™ & Vantage Pro 2 Plus™ Weather Stations, Davis Instruments), which consists of two components: a sleekly designed integrated sensor suite (ISS) to measure outdoor weather conditions, and a data-receiving console to receive the weather data wirelessly. Temperature, relative humidity, solar radiation, UV light, wind speed and direction were recorded during the sampling periods.

### **3.5.3 Sampling design**

#### **3.5.3.1 Short-term collection by ESP**

For short-term collection of particles, a Scanning Mobility Particle Sizer (SMPS) and a modified Electrostatic Precipitator (ESP) were used to collect samples to validate the SMPS+ESP+AFM method. Since we had only a SMPS and an ESP, we could only install them at one site for a month and then moved them to another site for a month. In the ESP, four iron nano-film detectors were placed for 7 hours each day with a flow rate of 0.3L/min (the exposure duration depended on the ambient level of acidic ultrafine particles). In total, 120 samples were collected in a month.

### **3.5.3.2 Long-term collection by DS**

For long-term collection of particles, the diffusion samplers (DS) and other relevant equipments were installed at each site. Nine iron nano-film detectors were placed inside the DS for exposures for 5-7 days at the rural site and 2-3 days at the urban site with a low flow rate of 0.03 L/min according to the ambient level of acidic ultrafine particles. After exposure, a new set of detectors replaced the exposed ones for the same exposure period. The whole sampling period lasted one or two months for each campaign. As such, about 10 sets of samples were collected and each set had 9 detectors. In total, about 90 samples were collected at each site.

### **3.5.4 Quantification and sizing of AUFPs collected on the detectors**

After sampling, the acidic and non-acidic particles collected on the detectors were sized and quantified in our laboratory. The sizes, diameters and shapes of acidic particles were imaged by AFM. Since two collection systems (i.e., ESP and DS) were utilized for sampling acidic particles, considering the collection efficiency of ESP and DS, respectively, the number concentration and size distribution of acidic ultrafine particles in the ambient air were determined. Moreover, the total number concentration of particles (including acidic and non-acidic particles) calculated by the SMPS + ESP + AFM method and DS+AFM method was compared respectively with continuous data obtained from the SMPS + CPC system to further validate these two methods.

### 3.5.5 SMPS Data processing and analysis

Typically, the sizes of submicrometer particles are categorized into three modes: a nucleation mode, representing quite newly formed particles; Aitken and accumulation modes, representing aged particles. In this study, we divided the size distribution into 5.5-10 (nucleation mode,  $N_{\text{nuc}}$ ), 10-100 (Aitken mode,  $N_{\text{Ait}}$ ), and 100-350 nm (accumulation mode,  $N_{\text{acc}}$ ). The PN concentrations in nucleation mode, Aitken mode, and accumulation mode were calculated with a 95% confidence level ( $p < 0.05$ ). The correlation coefficients and  $p$ -values between the different tested parameters were calculated. In addition, the measurement data of SMPS+CPC for identified nucleation mode particle burst events were checked to exclude any data caused by instrumental artifacts. Since SMPS+CPC instrument could be malfunctioned with reading artifact signals in the nucleation mode, possibly by air leak in the system (e.g., Hogrefe et al., 2006) or extremely high particle number concentrations introduced into the system (e.g., Joshi et al., 2012) Firstly, when the nucleation mode particle burst was observed, the SMPS was paused for ten minutes and then re-ran. This procedure was repeated every three-hour on the burst event days to avoid the malfunction of the instrument. Due to only a 20 mins data loss in 8 hours' data during nucleation mode particle burst events, the re-run procedure of SMPS+CPC almost had no influence in the data analysis. Secondly, nucleation mode particle burst events were often accompanied with high number concentration ( $>2 \times 10^4 \text{ cm}^{-3}$ ) of larger size particles i.e., Aitken mode particles ( $N_{\text{Ait}}$ ). Since high particle number concentrations ( $>2 \times 10^4 \text{ cm}^{-3}$ ) may enhance the CPC counting efficiency and diffusional particle losses in the CPC tubes (e.g., Joshi et al., 2012), to check if extremely high  $N_{\text{Ait}}$  had impact

on the instrument readings of nucleation-mode PN concentration ( $N_{\text{nuc}}$ ), 100 nm polystyrene latex (PSL) standard particles with a number concentration of  $1.0 - 2.0 \times 10^5 \text{ cm}^{-3}$  were generated and introduced into the SMPS at the end of each burst event to test the concentration-related performance of the SMPS. It was found that the SMPS+CPC can measure the number of PSL particles stably and particle size accurately without measurement of particles in nucleation mode. This examination suggested the little influence of high number concentration of particles in the Aitken mode on the measurement of particle concentration in nucleation mode. Hence, the increased  $N_{\text{nuc}}$  observed in nucleation mode particle burst events were the real ambient number concentrations, not the instrument artifact.

#### **3.5.5.1 Definition of nucleation mode particle burst and new particle formation event**

At the Mt. TMS site, NPF events were classified into three groups (Classes Ia, Ib and II) according to the classification scheme developed by Dal Maso et al., (2005), following the criteria that the particle mode must start in the distinct nucleation mode size and the particle mode must show signs of growth with a time span of hours. Class I presents the days when the formation and growth rate are determined with a good confidence level. Class I is divided into Class Ia and Ib. The Class Ia event has clear and strong particle formation with little or no pre-existing particles, while a Class Ib event is any other Class I event where the particle formation and growth rate still can be determined. A Class II event represents the event where the accuracy of formation rate calculation is questionable due to data fluctuation even though the banana shapes are still

observable. Days with no new particle formation observed are classified as non-NPF event days, due to the absence of particles in nucleation mode size range.

Basically, in a NPF event, nucleation particles produced from the photochemically-formed vapors are often accompanied with particle growth in hours while the nucleation particles formed from directly-emitted vapors do not show particle growth (Park et al., 2008; Gao et al., 2009; Cheung et al., 2011). Hence, at the urban site, a nucleation mode particle burst event was identified if the  $N_{\text{nuc}}$  greatly increased and prevailed over a few hours with a constant geometric mean diameter (GMD) without growth to larger particles. Moreover, the burst events should have positive correlation with primary gaseous pollutants (i.e.,  $\text{SO}_2$ ,  $\text{NO}_x$  and CO) and surface area of pre-existing aerosols. In contrast, a secondary nucleation mode particle formation (i.e., NPF) event was characterized if the  $N_{\text{nuc}}$  increased with continuous growth to Aitken- and accumulation-mode particles, and correlated well with solar radiation and occasionally  $\text{SO}_2$ , but not with other primary trace gases, i.e., CO and  $\text{NO}_x$ . Besides, all other sampling days without visual increase in  $N_{\text{nuc}}$  were classified as non-nucleation days.

#### **3.5.5.2 Calculation of formation rate ( $J_{5.5}$ ), growth rate (GR<sub>5.5-25</sub>) and condensational sink (CS)**

In this study, 5.5 nm particle formation rate (FR,  $J_{5.5}$ ) was represented and quantified by the following equation (Sihto et al., 2006), taking into account the coagulation losses and growth losses:

$$J_{5.5} = \frac{dN_{5.5-10}}{dt} + CoagS_{d_p=7nm} \cdot N_{5.5-10} + \frac{1}{4.5nm} GR_{5.5-10} \cdot N_{5.5-10} \quad 3.8)$$

where,  $J_{5.5}$  is the formation rate of new particles into the measurable range of above 5.5 nm. The coagulation loss for the interval 5.5–10 nm was approximated by a term representing loss of 7 nm sized particles (7 nm is approximately the geometric mean of 5.5 and 10 nm) with the concentration of  $N_{5.5-10}$ . The third term represents the loss due to condensation out of the 5.5–10 nm size range. Here the observed growth rate (GR) in the size range of 5.5–10 nm was quantified using the “mode fitting” method (Dal Maso et al., 2005). As only one line fitting is done for each particle formation event, this method assumes the growth rate to be constant throughout the event.

The evolution of modal geometric mean diameters (GMD) (Dal Maso et al., 2005) in a size range of 5.5–25 nm for each size distribution with a 4-minute resolution was used to examine particle growth processes:

$$GR_{5.5-25} = \frac{\Delta GMD}{\Delta t} \quad 3.9)$$

The condensation sink (CS) of newly formed particles, presented as the loss rate of molecules onto existing particles, was estimated by integrating over the aerosol size distribution as follows (Kulmala et al., 2005):

$$CS = 2\pi D \int D_p \beta_M(D_p) n(D_p) dD_p = 2\pi D \sum_i \beta_{Mi} D_{pi} N_i \quad 3.10)$$

where  $D$  is the diffusion coefficient of the condensing vapour,  $\beta_M$  is the transitional regime correction factor,  $D_{pi}$  is the particle diameter in size class  $i$ , and  $N_i$  is the PN concentration in the respective size class. For the particle diameter  $D_{pi}$  used in the Equation 3.10), the measured dry size spectra were

converted to wet size spectra by particle growth factor (GF) according to ambient relative humidity Laakso et al., (2004).

### 3.5.5.3 Contribution of sulfuric acid (SA)

To investigate the contribution of sulfuric acid (SA) vapor on the particle formation and growth, a predictive proxy based on global solar radiation, SO<sub>2</sub> concentration, condensation sink and relative humidity was used to estimate sulfuric acid concentrations (Mikkonen et al., 2011):

$$Q_{SA} = 8.21 \times 10^{-3} \cdot k \cdot \text{Radiation} \cdot [\text{SO}_2]^{0.62} \cdot (\text{CS} \cdot \text{RH})^{-0.13} \quad \mathbf{3.11}$$

where,  $Q_{SA}$  (cm<sup>-3</sup>s<sup>-1</sup>) is the source rate of SA, and  $k$  is a constant value 1.035.

### 3.5.5.4 Contribution of biogenic VOCs

Recent studies found that the growth rates of newly formed particles had positive correlations with monoterpene concentrations and their oxidation rates by O<sub>3</sub> not by OH radical (Yli-Juuti et al., 2011, Hao et al., 2011). The production rates of oxidation products of monoterpenes by O<sub>3</sub> in these NPF events were calculated from measured monoterpene (i.e.,  $\alpha$ - / $\beta$ -pinenes, myrcene, and limonene) and O<sub>3</sub> concentrations (Yli-Juuti et al., 2011):

$$[\text{OR}]_{\text{O}_3} = k_{\text{O}_3} \cdot [\text{O}_3] \cdot [\text{Monoterpene}] \quad \mathbf{3.12}$$

where the rate constant  $k_{\text{O}_3} = 1.4 \times 10^{-17}$  cm<sup>3</sup> molecules<sup>-1</sup> s<sup>-1</sup>.

## **Chapter 4: Development of iron nanofilm detectors**

### **4.1 Introduction**

In Hong Kong, there have been a few studies of the acidity of aerosols (e.g., Pathak et al., 2004; Yao et al., 2007). However, the aerosol acidity was characterized in terms of mass concentration, rather than number concentration. To our best knowledge, no study was conducted in Hong Kong to quantify the number concentrations of acidic ultrafine particles. Previous studies indicate that air pollution caused by particulate matter and ozone in the atmosphere of Hong Kong is serious (e.g., Pathak et al., 2003, 2004; Wang et al., 2005; Yao et al., 2007; So et al., 2007; Guo et al., 2009). Hence, Hong Kong is a proper location to test and improve the method of iron-film detectors so that reliable quantification of number concentration of acidic ultrafine particles can be obtained.

In order to obtain accurate number concentration of acidic ultrafine particles in the atmosphere of Hong Kong, this chapter mainly focused on the method development. The iron nanofilm coated on a silicon chip (i.e., the detector) used in previous study (Cohen et al., 2004a) was found to be easy to detach from the support under high humidity and high temperature. Hence, a variety of iron nanofilm detectors with more efficient and stable performance than those used in Cohen et al., (2004a) was developed in terms of substrate of the detectors and the coating methods. Standard acidic particles were generated and collected on the detectors. The sizes and shapes of reaction spots of generated acidic particles and the surface structure of the detectors were scanned by an Atomic Force Microscope (AFM), which was calibrated with

known size polystyrene latex (PSL) particles, acidic droplets and acid-coated carbon nanoparticles. Finally, the influence of temperature, relative humidity and gaseous pollutants on the surface structure of the detectors was explored.

## **4.2 Results and discussion**

### **4.2.1 Calibration of AFM**

In this study, the results showed that the width measurements (x-axis calibration) from the AFM were 1.24 times the nominal diameters of the PSL microspheres (see Figure 4.1a), whereas the height measurements (z-axis calibration) indicated that the measured height from the AFM was 0.39 times the nominal diameters of the PSL microspheres (see Figure 4.1b). The discrepancy between the measured width and nominal diameter of the standard PSL particles might be caused by the fact that the resolution of width is closely associated with the shape of the objects especially nanoparticles, and the variability in width and size of the scanning tips. The discrepancy between the measured height and nominal diameter of the standard PSL particles might be caused by sensitivity of the z-scanner. As we know, the height (vertical) measurement should be always correct assuming the Z-scanner of the microscope is properly calibrated. However, by using this AFM, we found the measured heights of PSL microsphere standards were less accurate than those obtained by Cohen et al. (2004a). The measured heights from the AFM were about 39% of the nominal diameters of the PSL microspheres. It might be mainly caused by the sensitivity of the z-pizeo and /or z-scanner. And to a lesser extent, the different materials on the surface of a sample could cause inaccurate topographic height measurement owing to the variation in

capacitive force between the tip and the sample (Yang et al., 2007). Although the vertical height measured by this AFM was much lower than the actual height, the correlation between the measured heights of different known-size PSL microsphere standards and their true diameters showed high reproducibility and precision (see Fig.4.1b). We can readily use the trendline equation to calibrate the AFM-measured particle diameters back to their true sizes. In this way, the actual  $z$  size can be obtained.

Similarly, to obtain the actual particle diameter ( $x$  size), a number of PSL microsphere standards with different diameters were used to calibrate the  $x$  size of the AFM. By using the calibration curve between the true diameters and the measured width ( $x$  size) of the PSL standards, the  $x$ -axis can be deconvoluted.

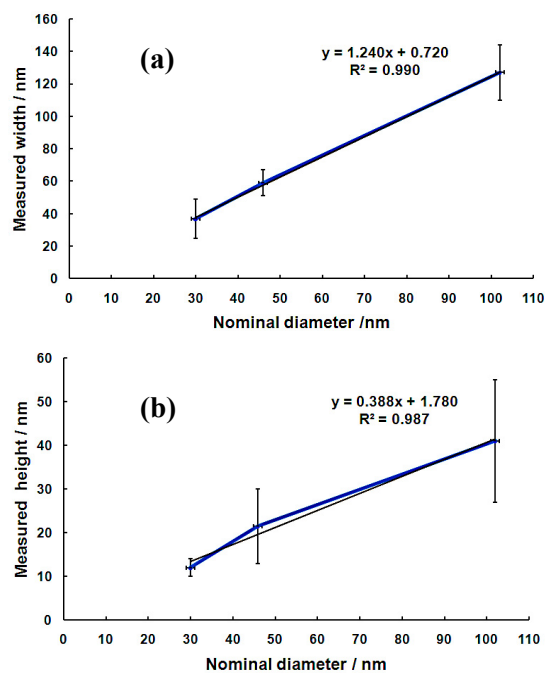


**Figure 4.1** Correlation between measured sizes and nominal diameters of the PSL microspheres; (a)  $x$ -axis calibration; (b)  $z$ -axis calibration. The vertical error bars represent the standard deviations (SD) of the measurements, and horizontal bars are the SD of the nominal diameters provided by the supplier of the PSL microspheres.

#### 4.2.2 Nanofilm Reaction Spots from Deposited Acidic Droplet and Acid-coated Standards

Figure 4.2 shows the two-dimensional (2D) and three-dimensional (3D) images of a reaction spot caused by a 75.4 nm sulfuric acid droplet deposited on the 25 nm thick iron nanofilm. This droplet was generated from the sulfuric acid solution of 0.009 g/cm<sup>3</sup>. The reaction site had a large bump due to the deformation of the iron film caused by the acidic droplet. The width of the reaction spot (full width of the bump, horizontal distance 1-1, 2D image) on the detector was  $310 \pm 27$  nm, about 4 times the diameter of the generated acidic droplet; and the vertical distance (from the base of the bump to the peak, 0-1, 3D image) of the bump was  $30.7 \pm 5.3$  nm, about two-fifths of the generated acidic droplet size.

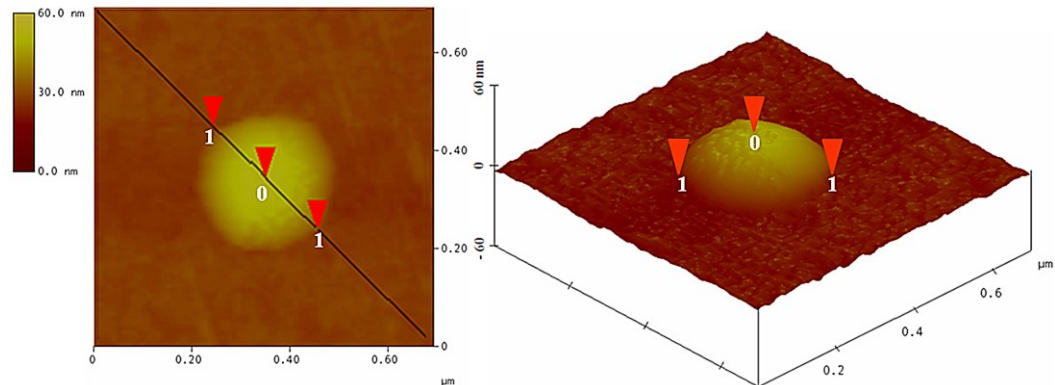


**Figure 4.2** Two-dimensional (2D) and three-dimensional (3D) images of a reaction spot caused by a 75.4 nm sulfuric acid droplet generated from the H<sub>2</sub>SO<sub>4</sub> solution with a concentration of 0.009 g/cm<sup>3</sup>

Figure 4.3 presents the correlation between horizontal distance (width) of reaction spot scanned by AFM and the diameter of generated acidic droplets. The results showed that the width of the reaction spot of acidic droplets on the

detectors was 2 to 4 times the diameter of generated particles (Figure 4.3, Ratio line). The width of the reaction spot was mainly dependent on the size of originally generated droplets and, to a lesser extent, the acidity. With the same acidity, the bigger the generated droplet was, the larger the width of the reaction spot on the detector was. It also clearly showed that the width of the reaction spot for large droplets (i.e., 75.4 and 124.5 nm) generated from H<sub>2</sub>SO<sub>4</sub> solutions increased with the decrease in pH values of H<sub>2</sub>SO<sub>4</sub> solutions, whereas the width for small droplet (i.e., 32.5 nm) remained constant. The higher acidity of the solution (low pH value) could produce particles more acidic. It may cause stronger corrosion on the surfaces of iron film, showing a larger outer ring of the reaction spot. While, lower acidity of the solution (high pH value) could produce droplets less acidic. It may cause weaker corrosion on the surfaces of iron film. Meanwhile droplets with less acidity means there was more water in the droplets. These droplets may lose water through evaporation in the process of deposition, showing smaller size of the reaction spots.

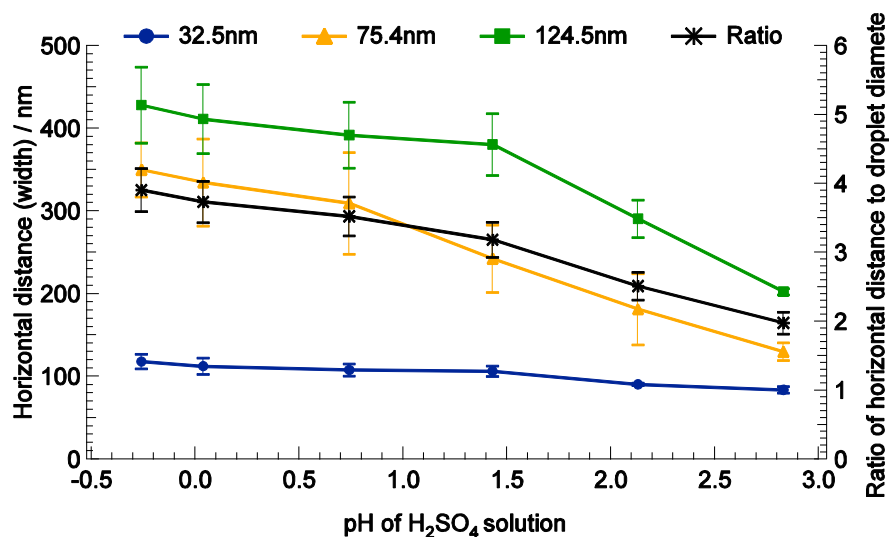


**Figure 4.3** Correlation between horizontal distance (width) of reaction spot scanned by AFM and the diameter of generated acidic droplets. The primary vertical axis represents the width of reaction spots; the secondary vertical axis represents the ratio of the width of reaction spots to the diameter of generated acidic droplets. The vertical error bars represent the deviation of the measurements

The vertical distance (height) of the reaction spots also had an obvious increase with the increase in droplet size (Figure 4.3). In addition, with the increase of the acidity of H<sub>2</sub>SO<sub>4</sub> solution, the height of the reaction spot increased for each of the three size droplets, ranging from one tenth to two-fifths, one-twentieth to two-fifths, and one-twenty-fifth to two-fifths of the size of the generated droplets, respectively. Moreover, the average ratio of the height of the reaction spot to the diameter of the corresponding droplet for the three size droplets obviously increased with the increase in acidity of H<sub>2</sub>SO<sub>4</sub> solutions used to generate acidic droplets. The particles produced by higher acidity of H<sub>2</sub>SO<sub>4</sub> solutions may cause stronger corrosion on the surfaces of iron film, showing a higher peak of the reaction spot. It is noteworthy that at the same acidity, the ratio of the measured height to the diameter of

corresponding droplet for the three size droplets was close with a low deviation, suggesting that the height of the reaction spot had a close correlation with size of the generated droplets.

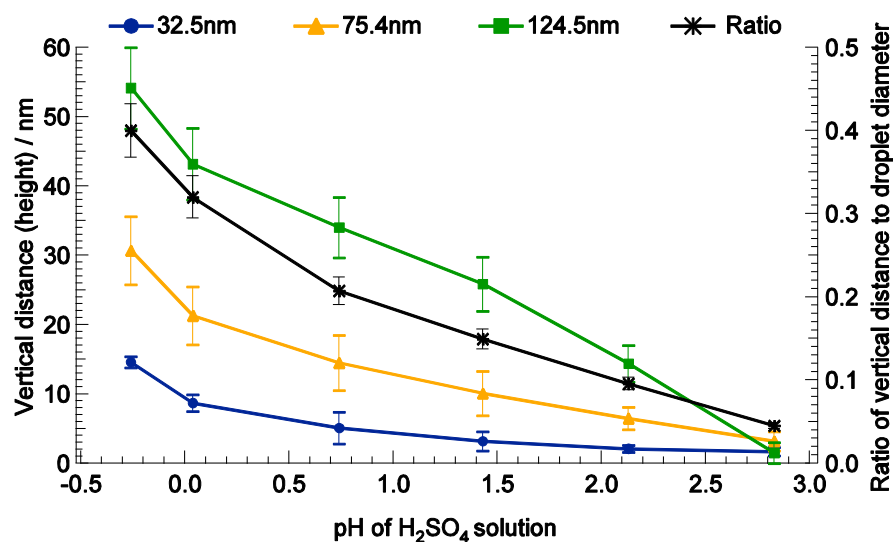


**Figure 4.4** Correlation between vertical distance (height) of reaction spot scanned by AFM and the diameter of generated acidic droplets. The primary vertical axis represents the height of reaction spots; the secondary vertical axis represents the ratio of the height of reaction spots to the diameter of generated acidic droplets. The vertical error bars represent the deviation of the measurements

Figure 4.5 (a & b) shows the 3D images of the reaction spots of a 32.5 nm and a 51.5 nm sulfuric acid-coated carbon particle on the iron nanofilm, respectively. The reaction site of the 32.5 nm sulfuric acid-coated particle had a large bump in the center surrounded by many extrusions (Figure 4.5a), whereas the reaction site of the 51.5 nm sulfuric acid-coated particle presented one large bump in the center surrounded by a circular ring (Figure 4.5b). The AFM-measured height and the width of the reaction spot for the 32.5 nm acidic particle were 11.8 nm and 108.2 nm, respectively, while for the 51.5 nm acid coated particle, the height and width were 21.4 nm and 172.8 nm,

respectively. The mechanism for such two different reaction spots was likely due to the fact that different surface to volume ratio of carbon particles caused different sulfuric acid adsorption onto particles, and subsequently different mass concentration of sulfuric acid on the surface of particles formed different morphology of reaction pits. To validate this assumption, we compared the differences of mass concentration between freshly-generated carbon particles (before exposed to  $\text{H}_2\text{SO}_4$  vapour) and  $\text{H}_2\text{SO}_4$  coated carbon particles in mobility size of 32.5 nm and 51.5 nm (after exposed to  $\text{H}_2\text{SO}_4$  vapour). The average mass ratio of 32.5 nm and 51.5 nm  $\text{H}_2\text{SO}_4$  coated carbon particles to original carbon particles was 1.81 and 1.28, respectively, suggesting that a smaller size particle had a higher  $\text{H}_2\text{SO}_4$  acid mass fraction, leading to a distinguished deformation on the surface of the iron nanofilm as shown in Figures 4.5a & b.

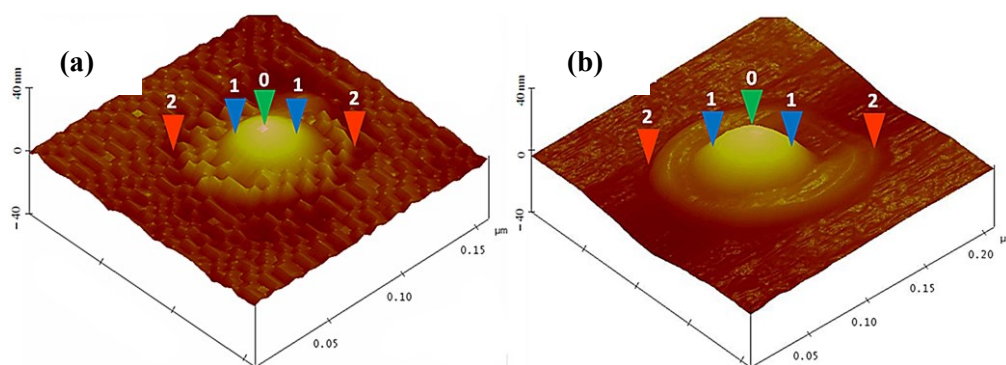


**Figure 4.5** Three-dimensional images of sulfuric acid-coated particle reaction spot on the 25-nm iron film; (a) A 32.5 nm acid-coated particle reaction spot; (b) A 51.5 nm sulfuric acid coated particle reaction spot. **Note:** The height of the reaction site above the iron-film surface was expressed as 0-2 vertical distance, and the width of the reaction site was taken as 2-2 horizontal distance i.e., maximum width of the reaction site. The central bump of the reaction site was taken as the width at half maximum value, shown as 1-1 horizontal distance.

Good correlations were found between the dimension of the reaction spots and the mobility diameter of the generated acid-coated particles (Figure 4.6). That is, the width of the reaction spots formed on the 25-nm iron film detectors was approximately three times (3.2) the diameter of the corresponding acid-coated particles ( $R^2=0.865$ ), and the height of the reaction spots was about one third (0.32) the diameter of the corresponding acid-coated particles ( $R^2=0.897$ ).

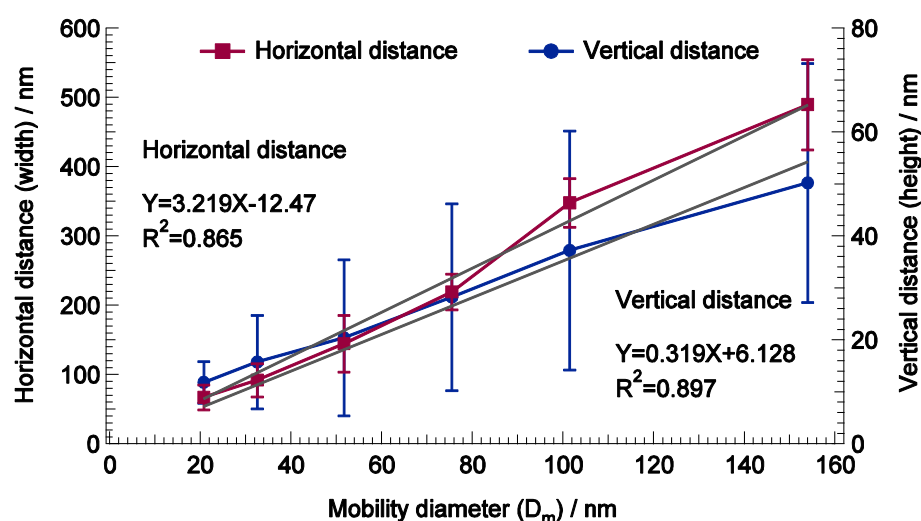


**Figure 4.6** Correlation between the dimension (width and height) of the reaction spots of acid-coated particles scanned by the AFM and the mobility diameter ( $D_p$ ) of the acid-coated particles. The vertical error bars represent the deviation of the replicate measurements

In previous studies, Horstman et al., (1967) found that measurements of the spot and acidic particle diameters by SEM yielded an average spot-to-particle diameter ratio of about 1.5 to 2. Cohen et al., (2000) illustrated that acid-coated carbon particles with a diameter of 100 nm produced clearly detectable reaction sites with the average height of  $35 \pm 16$  nm (average  $\pm$  standard

deviation) and the average width of  $704 \pm 230$  nm, implying that the spot-to-particle diameter ratio was 5 to 9. In our study, the average height of the reaction spots for 100 nm acid-coated carbon particles was  $28.3 \pm 12$  nm (about one third of the particle diameter) and the average width was  $316.4 \pm 56$  nm (approximately 3 times the particle diameter). The different spot-to-particle diameter ratios reported from different studies suggest that the dimension (width and height) of the reaction spot depends on the fraction of acid mass in the acid-coated particles, which could be different with the use of different acidic particle generation system, and on the characteristics of the iron nanofilm.

#### **4.2.3 Detector Response to Humidity, Temperature and Gaseous Pollutants**

During the 3-month exposure, the detectors were periodically examined visually and scanned with AFM. Visual observation of the exposed iron nanofilm detectors under the condition of 85% RH and 35°C showed that the surface of the Fe-VE and Fe-Ti-VE detectors with high number concentrations of standard acidic particles started to corrode after 2 weeks and was completely destroyed in three months. Compared to the AFM scan image before the exposure to high RH and temperature, the 32.5 nm sulfuric acid-coated carbon particles on the detectors under 85% RH and 35°C increased 2-3 times in diameter and 1.4-1.6 times in height. In contrast, the surfaces of the Fe-MS and Fe-Ti-MS detectors remained unchanged under the same weather condition for up to 3 months. Afterwards, they were partly corroded. In general, sputtered films typically have a denser structure, a smoother surface and a favourable thickness uniformity than evaporated films. The results of

performance test of detectors demonstrated that the Fe-MS and Fe-Ti-MS detectors had better stability and a better adhesion on the substrate than the Fe-VE and Fe-Ti-VE detectors. Further to investigate the adhesive strength of iron film on the substrate with and without coating Ti layer, no obviously difference was found during the 3 months exposure. However, after the exposure time was prolonged to 6 months, larger corroded areas on the surfaces of Fe-VE and Fe-MS detectors were found than those on the surfaces of Fe-Ti-MS and Fe-Ti-VE detectors, indicating iron film on the substrate without coating Ti layer was detached more easily from the substrate. The usage of a Ti intermediate layer enhanced the adherence of the iron nanofilm on the substrates.

Under the condition of 90% RH and 20°C, the surface structure of the four types of detectors did not have significant changes after 3-month exposure, only the sizes of the reaction spots slightly increased during the exposure period. For instance, the Fe-Ti-MS detectors with acidic droplets exposed to 90% RH and 20°C for 3 months showed some enlargement of the reaction spots (e.g., Figures 4.7a & b). Figure 4.7a showed that the size of the reaction spots of 32.5 nm standard acid-coated particles on the detector was  $112 \pm 27$  nm, 3 - 4 times the diameter of the standard particle. The height of the spot was  $16 \pm 8$  nm, about one half the diameter of the standard particle. After exposure to 90% RH and 20°C for 3 months, the dimension of the reaction site was enlarged horizontally and vertically to  $162 \pm 43$  nm and  $20 \pm 12$  nm, respectively (Figure 4.7b). The results demonstrated that both RH and temperature influenced the surface feature of the detectors. High temperature with a high RH can significantly destroy the iron nanofilm. Furthermore, the

results suggested that the Fe-MS and Fe-Ti-MS detectors were more resistant against extremely ambient conditions than the Fe-VE and Fe-Ti-VE detectors.

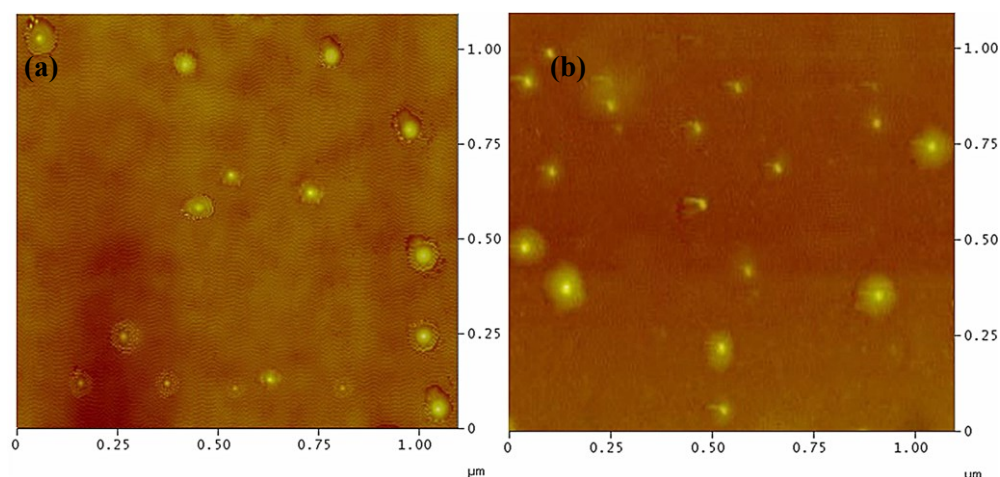


**Figure 4.7** AFM image of 32.5 nm acid-coated particles on Fe-Ti-MS detector; (a) AFM image before exposure to 90% RH and 20°C; (b) AFM image after 3-month exposure to 90% RH and 20°C

During the field measurement at Mt.TMS, Fe-VE nanofilm and Fe-MS nanofilm detectors were exposed to particle-free air to check if the ambient gases affected the surface of the detectors. The mean surface roughness of unexposed Fe-VE and Fe-MS nanofilm was  $0.31 \pm 0.17$  nm and  $0.28 \pm 0.15$  nm, respectively. The results of weekly quality control measurements on surface roughness showed that the average roughness in ten of  $1 \mu\text{m}^2$  area on the blank Fe-VE and Fe-MS nanofilm detectors were  $0.81 \pm 0.44$  nm and  $0.64 \pm 0.27$  nm, respectively. Small standard deviation values demonstrated that the detector surface was very stable for both Fe-VE and Fe-MS nanofilm detectors, especially for Fe-MS detectors. Based on the variations of the surface roughness, the surface roughness of these blank detectors was about 3 times that of unexposed detectors for the sampling period, particularly in September and November, perhaps due to the interference of occasionally high humidity

(range: 74.3%~99.8%) in September and/or high SO<sub>2</sub> (5.22 ppbv) and O<sub>3</sub> (67.41 ppbv) in November. Nevertheless, the increase in surface roughness had negligible effect on the quantification of acidic particles by AFM.

#### **4.2.4 Validation in a Field Measurement**

In the field measurement conducted at Mt.TMS, 23 groups of detectors (4 detectors per group, totally 92 detectors) were exposed to ambient air for seven hours and ultrafine particles were collected onto these detectors by an ESP on different sampling days at different time slots. According to the meteorological conditions and chemical composition of PM<sub>2.5</sub>, i.e., high RH and high SO<sub>4</sub><sup>2-</sup>, 16 detectors exposed on 22~25 November were preliminarily chosen for AFM scanning. The collected detectors were not scanned immediately after the deposition of particles. They were stored in a nitrogen atmosphere for 24 hours, and then scanned offline by AFM.

Figures 4.8 a & b show the AFM image of the exposed detectors collected during the sampling period. The acidic particles in the atmosphere deposited on the iron nanofilm detectors were easily distinguished from non-acidic particles (particles without surrounded rings and/or halos were assumed to represent non-acidic particles) in the atmosphere. Among a set of four detectors collected simultaneously, five of 100 μm<sup>2</sup> areas of each detector were randomly selected to measure the sizes and to count the total number of non-acidic and acidic particles on these detectors by AFM, respectively. Thus, in total twenty 100 μm<sup>2</sup> scanning areas were obtained for each group of detector samples. Table 4.1 presents the sampling time slots and average counts on each group of the detectors exposed in the sampling period (22 - 25 November 2010).

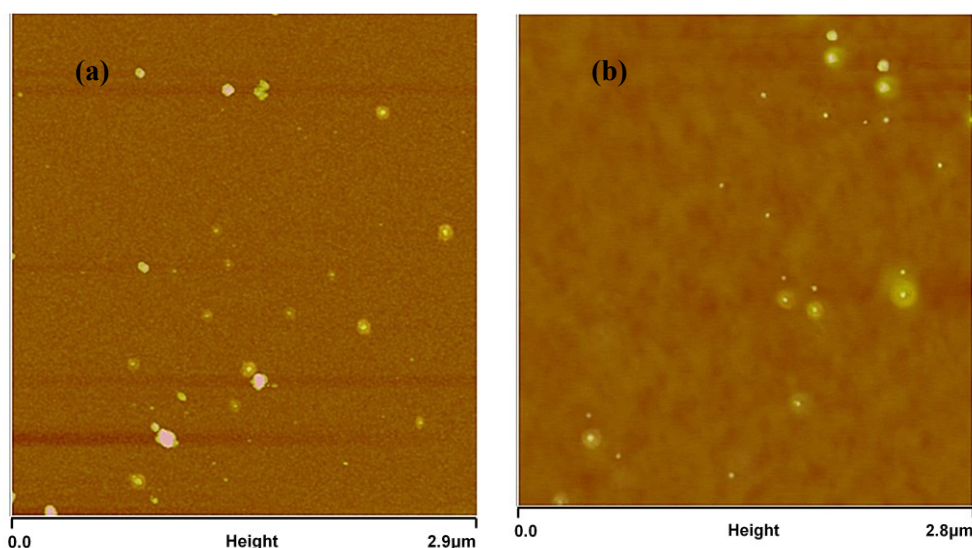


**Figure 4.8** Ambient acidic particles collected on the iron nanofilm detectors at Mt.TMS: (a) an AFM image with a  $2.9 \mu\text{m} \times 2.9 \mu\text{m}$  scanning area on a Fe-MS nanofilm detector; (b) a  $2.8 \mu\text{m} \times 2.8 \mu\text{m}$  scanning area on a Fe-VE nanofilm detector

The AFM scanning results showed that the total number of non-acidic and acidic particles collected on the detectors was more than 200 counts per  $100 \mu\text{m}^2$  scanning area. The size range of the non-acidic and acidic particles collected in field measurement was 7.5 - 386 nm and 7.4 - 312 nm, respectively. The diameter of non-acidic particles with peak value was larger than that of acidic particles, and both diameters with peak values changed on different sampling days. It is noteworthy that a remarkable number of acidic particles were below 20 nm, requiring high resolution scanning of  $1 \mu\text{m} \times 1 \mu\text{m}$  areas to distinguish the acidic particles from non-acidic particles. By repeating measurements for a number of particles in the field, good statistics can be obtained and histograms of size distributions compiled. Based on the number of non-acidic and acidic particles found on the detectors, the average number concentration of acidic particles in the atmosphere was estimated as follows.

**Table 4.1** Acidic and non-acidic particles collected during the field measurement at Mt.TMS (rural site)

Dates	Sampling time	Number of particles (mean± SD)		Size of particles (GMD± SD)*	
		Non-acidic particles per 100 $\mu\text{m}^2$	Acidic particles per 100 $\mu\text{m}^2$	Non-acidic particles size range and the diameter at peak per 100 $\mu\text{m}^2$	Acidic particles size range and the diameter at peak per 100 $\mu\text{m}^2$
22-Nov	15:00~22:00	236.7 ± 85.3	64.3 ± 28.4	8.5-375 nm 56.7 ± 11.9 nm	7.5-248 nm 47.7 ± 8.4 nm
23-Nov	15:00~22:00	147.2 ± 64.4	62.2 ± 32.5	9.4-386 nm 62.8 ± 14.7 nm	10.9-298 nm 43.6 ± 18.4 nm
24-Nov	15:00~22:00	157.8 ± 68.5	58.2 ± 29.6	8.7-358 nm 65.4 ± 21.8 nm	7.4-312 nm 50.4 ± 16.7 nm
25-Nov	15:00~22:00	194.6 ± 93.5	56.9 ± 32.4	7.5-316 nm 49.6 ± 18.7 nm	9.5-307 nm 40.5 ± 11.2 nm

\*The size of non-acidic particles was verified using the results of AFM  $x$  and  $z$  calibrations; the diameter of acidic particle or acidic droplet was verified according to the ratios between the size of reaction spot and the acidic droplet or acidic particle (see Section 4.2.2).

In the field measurement conducted at Mt.TMS, the size range of non-acidic and acidic particles collected on the detectors on 22 November, for example, was 8.5 - 375 nm and 7.5 - 248 nm, respectively. According to the setting of 44 channels in the SMPS, these measured non-acidic and acidic particles were categorized into 40 and 36 groups, respectively. The particle number concentration of each group was calibrated by the corresponding penetration rate of SMPS ( $PR_{SMPS}$ , see Figure 3.2) of these 44 channels, followed by the collection efficiency of ESP ( $E_{ESP}$ ), of which, the size range was classified into four groups, i.e., <30 nm, 30 - 50nm, 50 - 100nm, and >100nm. According to the known  $E_{ESP}$  values of the three size particles, i.e., 30, 50 and 100nm, the  $E_{ESP}$  of particles with a size larger than 100nm can be extrapolated from the

correlation between the  $E_{ESP}$  and particle size. Thus, the  $E_{ESP}$  values for these four groups of particles were 74%, 80%, 86% and 92%, respectively.

Since the collection plate of the ESP was a circle with a diameter of 20 mm diameter, it had  $3.14 \times 10^6$   $100 \mu\text{m}^2$  areas for AFM evaluation of the deposited particles. Hence, the ambient particles concentration,  $C_p$ , in particles per  $\text{cm}^3$ , derived from the number of deposited particles, is given by  $C_p = \sum N_i / (PR_{SMPS_i} \times E_{ESP_i} \times \text{Flow rate} \times \text{Time})$ , where  $N_i$  is the total number of particles in  $i$  size channel counted per  $100 \mu\text{m}^2$ ;  $PR_{SMPS_i}$  is the penetration rate of the  $i$  size channel particles; and  $E_{ESP_i}$  is the ESP collection efficiency of the  $i$  size channel particles. The sampling flow rate was  $300 \text{cm}^3/\text{min}$ . Since the scanning time for each spectrum was 4 min and 5 seconds for each channel, the sampling time for each size channel was  $7\text{h} \times 60\text{min}/\text{h} \times 5\text{s}/4\text{min} = 525\text{s}$ . By summing up the calculated number concentration of each size channel, the number concentration of the non-acidic and acidic particles on 22 November was  $(4.60 \pm 0.86) \times 10^3/\text{cm}^3$  (peaked at  $56.7 \pm 11.9 \text{ nm}$ ) and  $(2.10 \pm 0.45) \times 10^3/\text{cm}^3$  (peaked at  $47.7 \pm 8.4 \text{ nm}$ ), respectively. The total number concentration of ambient particles on 22 November was  $(6.70 \pm 0.41) \times 10^3/\text{cm}^3$  (peaked at  $51.6 \pm 10.8 \text{ nm}$ ). Similarly, the number concentrations of non-acidic and acidic particles and the total number concentration of ambient particles on the other three days (i.e., 23-25 November) were obtained (Table 4.2).

**Table 4.2** Comparison of the number concentration of ambient particles calculated by AFM with the values derived from the SMPS+CPC in the field measurement at Mt.TMS (rural site)

Date	Sampling time	Number concentration of particles (mean± SD 10 <sup>3</sup> /cm <sup>3</sup> )			
		Non-acidic particles	Acidic particles	Total particles	SMPS+CPC data*
22-Nov		4.60 ± 0.86	2.10 ± 0.45	6.70 ± 0.41	7.74 ± 1.56
23-Nov	15:00 - 22:00	2.86 ± 0.65	1.61 ± 0.42	4.48 ± 0.23	5.66 ± 1.10
24-Nov		3.07 ± 0.68	1.51 ± 0.35	4.58 ± 0.33	5.10 ± 1.03
25-Nov		3.78 ± 0.71	1.48 ± 0.36	5.26 ± 0.35	6.29 ± 1.39

\*For SMPS+CPC, the average hourly particle number concentration for the sampling period was calculated according to the trend of diurnal variation and the hourly averages for non-sampling period. Two-tail *t*-tests between the ambient particle number concentration measured by the AFM and the SMPS+CPC at 15:00 – 22:00 on these four days indicated that the *p* value was larger than 0.05.

The total number concentration of particles calculated by the SMPS + ESP + AFM method was compared with continuous data obtained from the SMPS + CPC system. Due to the fact that only one SMPS was available for our study, the number concentration and size distribution of ambient particles measured by SMPS + CPC were not obtained at the same time as the sampling time of SMPS + ESP. According to the stable metrological conditions from 20 to 29 November and integrated SMPS + CPC data on 20-21, and 26-29 November, the diurnal pattern of number concentration and size distribution was found to be similar on these days (data not shown here). Hence, it is reasonable to assume that the diurnal pattern of number concentration and size distribution on the sampling days of 22-25 November was the same as that on other days. Consequently, the mean number concentration and size distribution of

particles between 15:00 and 22:00 of a day were derived from the data measured by the SMPS + CPC at other hours on the same day. The comparison of the total number concentrations counted on detectors with the values derived from the SMPS + CPC is shown in Table 4.2.

It was found that the total number concentrations of ambient particles measured by the ESP collection and AFM analysis of the detectors were well in line with the levels measured by the SMPS + CPC on these four days (two-tail t-test,  $p>0.05$ ). Moreover, the geometric mean diameter (GMD) of the particles measured by these two methods showed remarkable agreement, namely, the average GMD measured by the SMPS + CPC was  $52.3 \pm 6.9$  nm (45.8 - 60.3 nm) and the AFM measured average GMD was  $51.9 \pm 3.1$  nm (49.1 - 56.3 nm). The results suggested that the iron nanofilm detectors could be a reliable tool for the measurement and analysis of acidic particles in the atmosphere, if more areas of the detectors were scanned and better resolution of the AFM images was achieved.

### **4.3 Summary and conclusions**

In this chapter, an iron nanofilm detector method was developed for the estimation of number concentration and size distribution of acidic particles in ambient air. Two new types of iron nanofilm detectors (i.e., Fe-Ti-MS and Fe-MS) were made and their surfaces and adhesion to silicon substrate remained stable when the surfaces of Fe-Ti-VE and Fe-VE detectors started to corrode after 2-week exposure under severe weather condition (85% RH and 35°C). However, under the condition of 90% RH and 20°C, the surface structure of the four types of detectors did not have significant changes at the end of the 3-month exposure period. Only some enlargement of the reaction sites was

observed during the exposure period. In addition, ambient gases were found to have negligible effect on the surface roughness of the iron nanofilm detectors.

It is crucial to establish the relationship between reaction spots on the detector and the size of generated acidic droplets and acid-coated particles. To achieve the purposes, acidic droplets and acid-coated standard particles were generated. The results showed that for acidic droplets, larger droplet with the same acidity as smaller droplet had a larger horizontal distance (width) and vertical distance (height) of the reaction spot. The width of the reaction spot on the detectors was 2 to 4 times the mobility-based diameter of generated droplets. With the increase of the acidity of H<sub>2</sub>SO<sub>4</sub> solution, the height of the reaction spot increased, ranging from one-twenty-fifth to two-fifths the mobility-based diameter of the generated droplets. For acid-coated particles, the width of reaction spots on the detectors was more than three times the mobility-based diameter of originally generated particle, while the height of reaction spots was about one third of the original particle mobility diameter.

The developed iron nanofilm detectors were used in a field measurement in order to prove that the method developed in this chapter was suitable for measuring the number concentration of acidic particles in the atmosphere. The number concentrations of ambient acidic particles, non-acidic particles and total particles were measured using the detectors. The results indicated that the total number concentrations of ultrafine particles measured on the iron nanofilm detectors were close to the number concentrations measured by the SMPS+CPC system ( $p > 0.05$ ), and the average GMD of the particles measured by AFM ( $51.9 \pm 3.1\text{nm}$ ) had a good agreement with that measured by SMPS + CPC ( $52.3 \pm 6.9\text{nm}$ ). Although the iron nanofilm detector method

is time-consuming for AFM scanning, the field measurement results indicate that this method is promising and feasible for the detection and evaluation of the number concentration and size distribution of ambient acidic aerosols. To achieve a better performance of this method, it is important to possess an AFM with higher resolution.

## **Chapter 5: Diffusion sampler for measurement of AUFPs**

### **5.1 Introduction**

In Chapter 4, the ambient particles were size-selected by differential mobility analyzer (DMA) and deposited onto the nanofilm detectors using an electrostatic precipitator (ESP). The AUFPs deposited on the iron nanofilm detectors, on which reaction spots were formed, were then counted and sized using an atomic force microscope (AFM). This earlier work was a development and validation of an analytical method that used iron film detector and AFM to identify and size acidic and non-acidic particles. However, this method has limitation for the assessment of long-term exposure to AUFPs due to the fact that 1) the detector will be saturated after only several hours of sampling by the ESP, and it will be highly time-consuming if using this approach to assess long-term exposure because numerous short-term samples for AFM analysis are needed; and 2) the cost is high for the operation and maintenance. Hence, the present study aimed to develop a relatively inexpensive sampler that would overcome the above problems and still be appropriate to the AFM analysis method developed in our work. It is noteworthy that while the AFM is a sophisticated measurement tool, one AFM could be used to assay samples from multiple sites. This will significantly reduce the cost, time and manpower.

This chapter presented a low-flow diffusion sampler (DS) with a flat rectangular channel that was used to estimate long-term average size

distributions and number concentrations of AUFPs. The sampler was designed based on the rationale that smaller particles, i.e., particle size  $<200$  nm entering the sampler would be more efficiently deposited by diffusion onto the collection surface of the channel. The nanofilm detectors were deployed inside the sampler at different locations along the channel to collect AUFPs. The total particle deposition efficiency of the sampler is a function of particle size and channel length with a fixed sampling flow rate, which decreases with the increase of particle size, and increases with the increase of distance from the inlet. To assess long-term exposure, the iron nanofilm detectors at different locations in the DS were utilized to collect ambient acidic aerosols over a period of days to weeks. After obtaining the counts of acidic particles in different size bins on the detectors from the AFM image analysis, the number concentration and size distribution of acidic particles in the air were calculated based on known collection efficiency of DS for each particle size bin. Because the DS is much cheaper, lighter and easier to operate than commercial samplers, e.g., DMA+ESP, this technique provides an alternative approach for the measurement of ultrafine particles, especially for the AUFPs once the results are proved to be robust.

Actually, concerns have been raised from previous study about collecting particles with the principle of diffusion (Cohen et al., 2004a). The diffusion sampler developed in this chapter was different from the design of previous investigators in several aspects: (1) Development of the detector settling locations inside the sampler. Generally, with the increase of the distance between detector settling location and the sampling inlet, the deposition efficiency of smaller particles is higher than that of larger particles. Hence,

different patterns of particle size distribution will appear at different detector settling locations. In previous design of Cohen et al., (2004a), nanofilm detectors were placed side by side in the cut receptacle at 7.0, 201.5, and 452 mm (midpoint of detector) from the inlet along the length of the channel. In our design, the third detector settling location was lengthened to 472.5 mm. The distance between the farthest settling location and the inlet was specifically increased for more effective separation of particles of different sizes; (2) Development of iron nanofilm detectors with effective and stable performance for long-term sampling duration. Two new types of iron nanofilm detectors (namely Fe-Ti-MS and Fe-MS) were developed, which were stable even after 3-month exposure to ambient air at a sampling site; (3) Development of sampling schedules based on the ambient particle number (PN) concentration. Fewer or no acidic particles were detected in the previous study in New York (Cohen et al., 2004b), suggesting that the method might either not be suitable for an airshed with low levels of air pollutants, or it should be improved. To ensure sufficient particles to be collected on the detectors for subsequent statistical analysis, and to avoid collected particles landing on one another resulting in underestimation of smaller particles and over-measurement of larger particles, the sampling duration was altered depending on the ambient PN concentration. For example, on the days with lower PN concentrations, a longer sampling duration was needed, whereas a shorter sampling duration was designed on the sampling days with higher PN concentrations; and (4) Establishment of an empirical method to calculate the number concentration and size distribution of particles in the atmosphere using the stepwise deposition efficiencies of particles at three different locations.

Before used for field sampling, the deposition efficiencies of DS as a function of particle size, sampling flow rate and even the distance of the detector location from the inlet were determined and expressed as semi-empirical equations derived from theoretical prediction and experimental measurements. The collection efficiency of the DS was calibrated experimentally using three different sizes of monodisperse polystyrene latex (PSL) microsphere standard with six different flow rates. After calibration, field measurement campaign was carried out at an urban site to assess the reliability and efficiency of the DS for the measurement of acidic and total ultrafine particles. The total particle number concentrations and size distributions estimated by the DS+AFM method were compared with the data obtained from the real-time scanning mobility particle sizer and condensation particle counter system (SMPS+CPC).

## **5.2 Results and discussion**

### **5.2.1 Collection efficiency of DS**

Figure 5.1 shows the theoretically-calculated (solid lines) and experimentally-determined (dots) deposition efficiencies of three different sizes of particles at the three different rectangular recess locations in the DS with six different air flow rates. It was found that the experimentally determined deposition efficiencies of the three-size particles, i.e.,  $\Delta\eta_a'$ ,  $\Delta\eta_b'$  and  $\Delta\eta_c'$  at these three locations with six different flow rates were all higher than corresponding theoretical values. The higher measured deposition efficiency suggested that apart from dominated diffusive deposition, sedimentation, inertial and/or even electrostatic forces on the deposition of particles need to be considered (Hinds

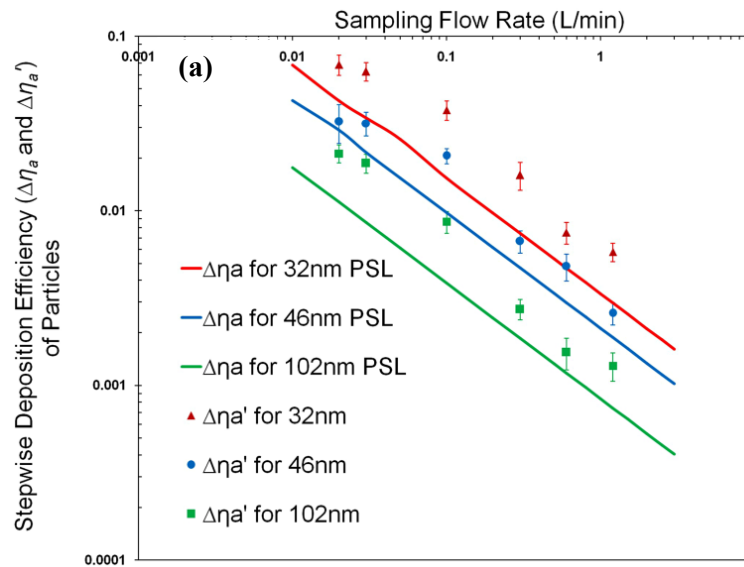
1999). Sedimentation losses mainly occur for larger particles (e.g., Fissan et al., 1997). Additional deposition of the larger particles is inertia impaction (e.g., Cohen et al., 1990). Electrostatic forces may have an effect on the enhanced deposition of smaller particles (e.g., Elimelech and O'Meliat, 1990; Semmler et al., 1998). In the present experimental calibration, the impact of the particle charge should be minor because the PSL particles used for calibration were electrically neutral particles and electrostatic forces might not be important since the plates making up the DS were metal. The theoretical equations need to be modified using the experimental data for the calculation of deposition efficiency. It can be seen that the stepwise deposition efficiency at the first location (i.e., the midpoint of the rectangular recess from the inlet was 7 mm) for all three-size particles decreased with the increase in flow rates (see Figure 5.1a). This was probably caused by the fact that higher flow rate would give less retention time for the deposition of particles on the detector's surface at the first location. Both theoretical and experimental data showed a power-law function of flow rate  $Q$ .

Furthermore, the stepwise deposition efficiency at the first location for each flow rate decreased with the increase in particle size (see Figure 5.1a). This was mainly due to the fact that diffusion coefficient  $D$  of smaller particle was much higher than that of larger particle. Hence, the deposition efficiency was dominated by diffusion, namely increasing with the decrease in particle size. As shown in the theoretical equations 3.4-3.5), the collection efficiency  $\eta$  is dependent on  $\mu$ . At the first location it was found that the deposition parameter  $\mu$  values for all 18 experimental scenarios calculated by theoretical equations were smaller than 0.003. Hence, the theoretical collection efficiency  $\Delta\eta_a$  was

derived from equation 3.4). The collection efficiency  $\Delta\eta_a$  showed a power-law relationship with  $\mu$ . Based on the relationship between theoretically-calculated  $\Delta\eta_a$  and  $\mu$ , the 18 experimental scenarios were utilized to estimate the relationship between experimentally-determined  $\Delta\eta_a'$  and  $\mu$  by nonlinear regression analysis (STATISICA 99 Edition 5.5A, USA). The  $\Delta\eta_a'$  as a function of  $\mu$  was estimated by a model:  $\Delta\eta_a' = \alpha_1 \times (\mu_{L2}^{\alpha_2} - \mu_{L1}^{\alpha_2})$  using the Quasi-Newton method. The  $\mu_{L1}$  and  $\mu_{L2}$  are the independent variables. The two parameters  $\alpha_1$  and  $\alpha_2$  are constants. After model estimation, the modified semi-empirical equation for the calculation of diffusive deposition efficiency at the first location was obtained as follows:

$$\Delta\eta_a' = 3.20 \times (\mu_{L2}^{0.576} - \mu_{L1}^{0.576}) \quad (5.1)$$

where the  $\mu_{L1}$  and  $\mu_{L2}$  represent the deposition parameters along with the channel length of L1 and L2, respectively, and are estimated using equations 3.6) and 3.7); the constant  $\alpha_1$  is a modified factor and  $\alpha_2$  is a power-law exponent obtained from experimental data. The constant  $\alpha_1$  and  $\alpha_2$  were 3.20 and 0.576 (regression coefficient,  $r = 0.968$ ) in equation 5.1), respectively.



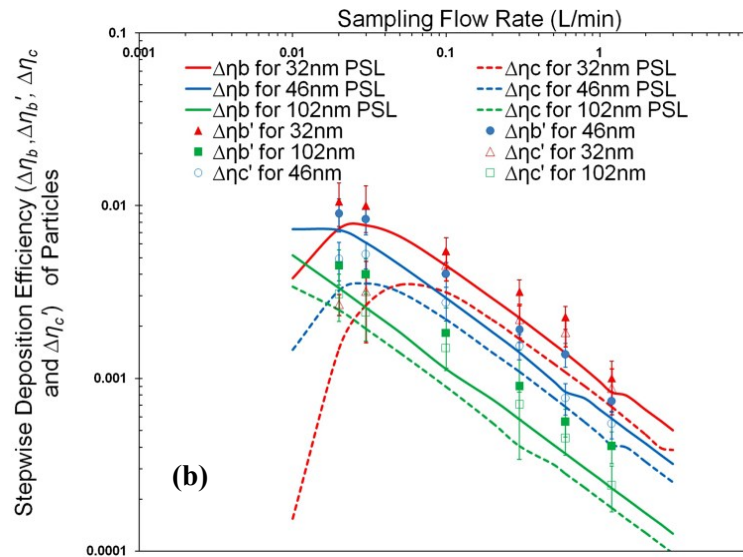


**Figure 5.1** Theoretical and experimental stepwise deposition efficiencies of three-size PSL particles as a function of flow rate: **(a)** at the first location ( $\Delta\eta_a'$  is experimental efficiency and  $\Delta\eta_a$  is theoretical efficiency); **(b)** at the second and third locations ( $\Delta\eta_b'/\Delta\eta_b$ , and  $\Delta\eta_c'/\Delta\eta_c$ , respectively). Error bars on the experimental data represent the standard deviations (SD) of the measurements

In contrast, the stepwise deposition efficiencies at the second (i.e., 201.5 mm) and third (i.e., 472.5 mm) locations showed different relationships with  $d_p$  and  $Q$  from that at the first location (Figure 5.3b). The values of  $\mu$  at the two locations were all larger than 0.003 except for larger size particles (e.g. >100 nm). Both the theoretical and experimental data did not show a power-law function of  $Q$  for each particle size at these two locations. Instead, at the second and third locations the deposition efficiencies for 32 and 46 nm PSL particles increased with the increase in flow rates when the flow rate was lower than 0.02 L/min. This was likely due to the fact that the transport distances of particles from the inlet to the second and third locations were much longer than to the first location. In other words, most of the smaller size

particles such as 32 nm and 46 nm PSL particles would only travel a short distance before diffusive deposition when the air flow rate was very low (e.g., <0.02 L/min). With the increase of the flow rate, more small particles reached the second and third locations. When the flow rate increased to 0.02 L/min (except 0.04 L/min for 32 nm PSL at the third location), the deposition efficiencies of small particles, i.e., 32 nm and 46 nm PSL particles, had the maximum values. The results suggested that there was a balance between transport and deposition of particles. However, when the air flow rate increased to >0.02 L/min (and >0.04 L/min for 32 nm PSL at the third location), the deposition efficiencies of these small particles decreased with the increase of flow rate, perhaps owing to the fact that the deposition positions of the particles were beyond the second and third locations after the increase of flow rates. As such, it is clear that there was a significant dependence of diffusion deposition on the flow rate.

At the second and third locations the values of  $\mu$  for the studied particle sizes (i.e., 32 and 46 nm) were all larger than 0.003 with the six different flow rates and for the 100 nm particles with the air flow rates < 0.6 L/min (total 16 experimental scenarios); hence, equation 3.5) was used to express exponential relationships of  $\mu$  with  $\Delta\eta_b$  and  $\Delta\eta_c$ . The  $\Delta\eta_b$ ' and  $\Delta\eta_c$ ' as a function of  $\mu$  determined from these 16 experimental scenarios were approximated by nonlinear regression method with exponential models:  $\Delta\eta_b' = \beta_1 \times [\exp(-\beta_2 \mu_{L3}) - \exp(-\beta_2 \mu_{L4})]$  and  $\Delta\eta_c' = \lambda_1 \times [\exp(-\lambda_2 \mu_{L5}) - \exp(-\lambda_2 \mu_{L6})]$ . The constant  $\beta_1$  and  $\lambda_1$  are the modified factors for the semi-empirical equations;  $\beta_2$  and  $\lambda_2$  are the determined constants for the independent variables at the second and third locations. Finally, the modified semi-empirical equations for the calculation of

diffusive deposition efficiency at the second and third locations (i.e.,  $\Delta\eta_b'$  and  $\Delta\eta_c'$ ) were obtained as follows, respectively:

$$\Delta\eta_b' = 1.844 \times [\exp(-8.04 \times \mu_{L3}) - \exp(-8.04 \times \mu_{L4})] \quad 5.2)$$

$$\Delta\eta_c' = 1.957 \times [\exp(-7.43 \times \mu_{L5}) - \exp(-7.43 \times \mu_{L6})] \quad 5.3)$$

where the  $\mu_{L3}$ ,  $\mu_{L4}$ ,  $\mu_{L5}$  and  $\mu_{L6}$  represent the deposition parameters along with the channel length of L3..., and L6, respectively, and are estimated using equations 3.6) and 3.7); The constants  $\beta_1$  and  $\beta_2$  were 1.844 and 8.04 (regression coefficient,  $r = 0.981$ ) for the second location in equation 5.2), respectively. And  $\lambda_1$  and  $\lambda_2$  were 1.957 and 7.43 (regression coefficient,  $r = 0.968$ ) for the third location for the three-size particles with the six different flow rates in equation 5.3).

### 5.2.2 Validation of the diffusion sampler

To test whether the DS was working properly, a field measurement was conducted at the HH site from 22 December 2010 to 15 January 2011. The average ambient temperature was  $15 \pm 3^\circ\text{C}$  during the sampling period. Ten groups of detectors (nine detectors per group, in total 90 detectors) were exposed to ambient air for 48 - 72 hours using the DS. The average UFPs number concentration measured by the SMPS+CPC system was  $2.4 \pm 0.4 \times 10^4 \text{ cm}^{-3}$  and the dominant particle size was  $\sim 30 \text{ nm}$  at this urban site during the sampling period. It is noteworthy that sampling duration of two - three days was appropriate for the level of UFPs number concentrations in urban environments, whereas in rural environments longer sampling duration such as over one week might be required. The ten groups of detectors exposed were then analyzed using AFM to calculate number concentration and size distribution of ambient UFPs and AUFPs. Tables 5.1 and 5.2 present the acidic

PN and the total PN concentrations measured by the DS+AFM system, and the total PN concentration measured by the SMPS+CPC system, respectively. The group of detectors collected on 22-25 December 2010 was used as an example to show how the acidic and total PN concentrations were obtained (also see Table 5.1). When the detectors were scanned by the AFM, the original scanning area on the detector was set to be  $10 \times 10 \mu\text{m}$ . If particles were found in this area, smaller areas, i.e.,  $5 \times 5 \mu\text{m}$  and  $2 \times 2 \mu\text{m}$  were further scanned to obtain clearer images of particles. Figure 5.2 (a, b and c) shows the AFM scanning images of ambient particles collected on the detectors at the three different locations of the DS. The particles surrounded by a circular ring were regarded as the acidic particles. The dimensions of the reaction spots were examined by the AFM and used to extrapolate the particle diameters based on the correlations between the particle diameter and the size of the reaction spot. After the AFM scanning and analysis, the data were categorized and calculated to derive the number concentration and size distribution of ambient AUFPs and total UFPs (Table 5.1).

For example, the three detectors with ID name of A1, A2 and A3 deployed at the first location were scanned. Ten of  $100 \mu\text{m}^2$  areas of each detector were randomly selected to scan the size and the number of acidic and non-acidic particles on the surfaces of the detectors. In total, thirty  $100 \mu\text{m}^2$  scanning areas were obtained for the detector samples at the first location of the DS. To compare with the SMPS+CPC measurement data, the scanned total and acidic particles were categorized into 22 size bins following the channel setting in SMPS, i.e.,  $<5$ ,  $5-10.2$ ,  $10.2-15.8$ ,... ,  $171.7-192$  and  $192-215.2$  nm (see

Figure 5.3). The arithmetic mean diameter (AMD) in each size bin was calculated using the equation:

$$AMD = \frac{\sum_i d_{pi} n_{pi}}{N} \quad 5.4)$$

where,  $d_{pi}$  is the particle size,  $n_{pi}$  is the particle count in size  $d_{pi}$ , and  $N$  is the total number counted in the corresponding size bin.

The stepwise deposition efficiency, i.e.,  $\Delta\eta_a'$ , for particles in each size bin was then calculated using the equation 5.1). Based on the  $\Delta\eta_a'$  values, the counted total acidic and non-acidic particles, air flow rate and sampling durations, the ambient acidic and total PN concentrations in the 22 size bins were obtained (see Figure 5.3). That is, the ambient particle concentration  $C_a$ , derived from the number of deposited particles on the detectors at the first location of the DS, is given as follows:

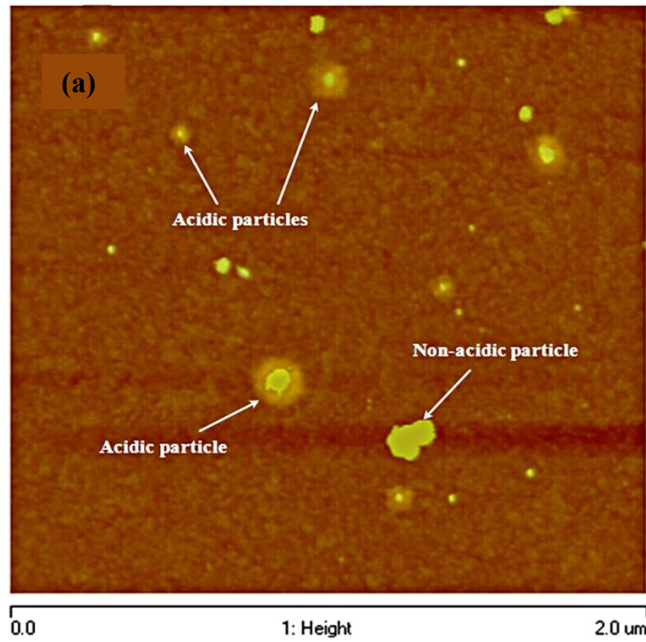
$$C_a = 2.5 \times 10^5 \times \sum \{N_{d_{pij}} / (\Delta\eta_{a',d_{pij}} \times Q \times \text{sampling time})\} \quad 5.5)$$

where  $N_{d_{pij}}$  is the number of particles in the size bin from  $d_{pi}$  to  $d_{pi}$  counted per  $100 \mu\text{m}^2$ ;  $\Delta\eta_{a',d_{pij}}$  is the deposition efficiency of the particles in the same size bin. By summing up the calculated number concentration in each size bin, the average number concentrations of total and acidic particles were obtained.

Similarly, the total and acidic particles deposited on the detector samples at the second (ID name: B1, B2 and B3; 201.5 mm from the inlet) and third locations (ID name: C1, C2 and C3; 472.5 mm) were counted and used to calculate ambient total and acidic particle number concentrations ( $C_b$  and  $C_c$ , respectively) incorporating with  $\Delta\eta_{b',d_{pij}}$  and  $\Delta\eta_{c',d_{pij}}$ , respectively. Finally, the mean number concentrations of total and acidic particles measured by one set of nine detectors were determined by averaging the values obtained at the

three different locations. In addition, the averaged number concentrations of ambient particles in the 22 size bins provided a discrete particle size distribution. The particle size distribution was further converted to a continuous distribution using the PN concentration in each size bin divided by the range of the size bin (i.e.,  $dN/dd_p$ ). To further obtain the lognormal size distribution, the lognormal particle size was calculated using the equation:  $dN/d\log d_p$  (see Figure 5.4). The geometric mean diameter (GMD) of the size distribution was calculated using the equation:

$$\text{Log}(GMD) = \frac{\sum_i n_{pi} \log d_{pi}}{N} \quad 5.6)$$



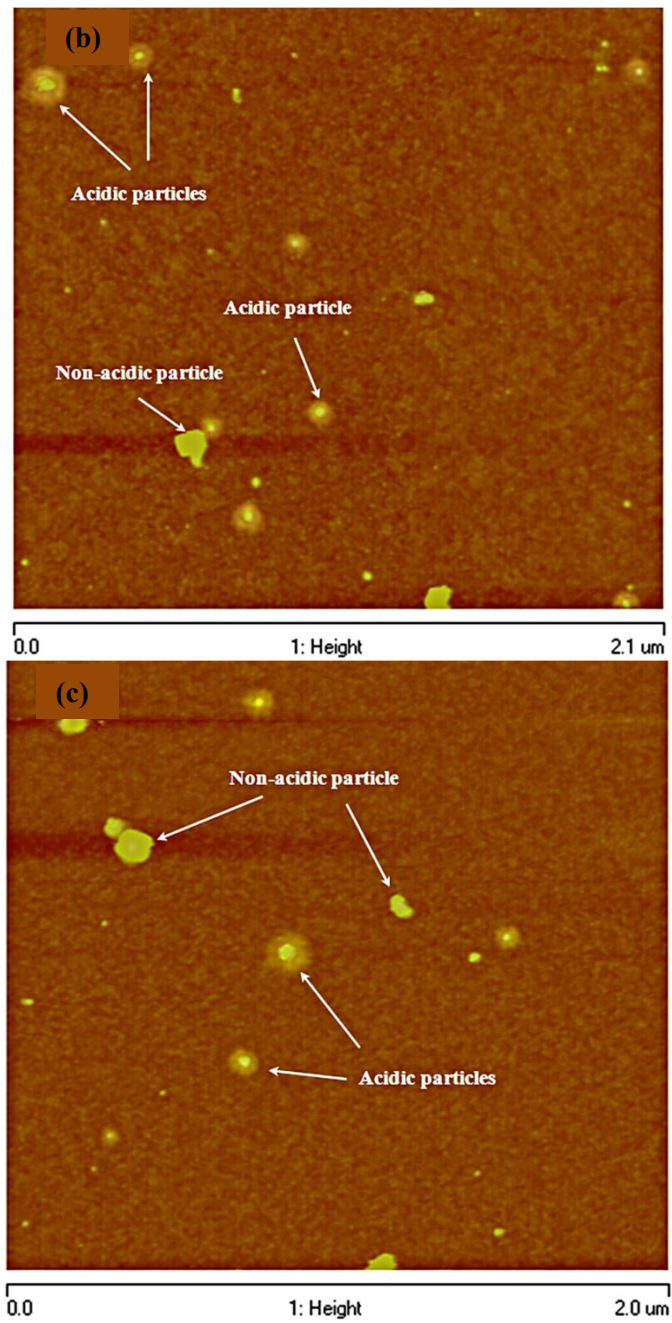


**Figure 5.2** AFM scanning images of ambient particles collected on the Fe-MS nanofilm detectors in the DS. (a) at the first location i.e., 7mm from the inlet; (b) at the second location i.e., 201.5 mm from the inlet; (c) at the third location i.e., 472.5 mm from the inlet.

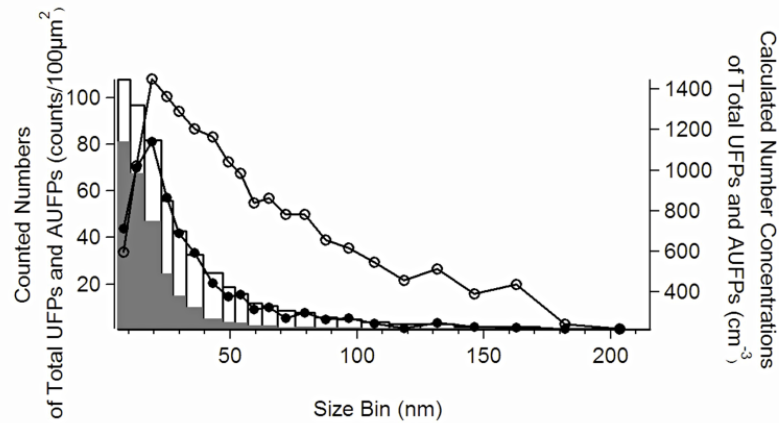


**Figure 5.3** The average numbers of total (white bar) and acidic particles (black bar) counted in each  $10 \times 10 \mu\text{m}$  scanning area on the three detectors with ID name of A1, A2 and A3 deployed at the first location and the average number concentrations of ambient total (line with white dots) and acidic particles (line with black dots) calculated based on the corresponding counted numbers of 5.5-200 nm particles in 22 size bins.

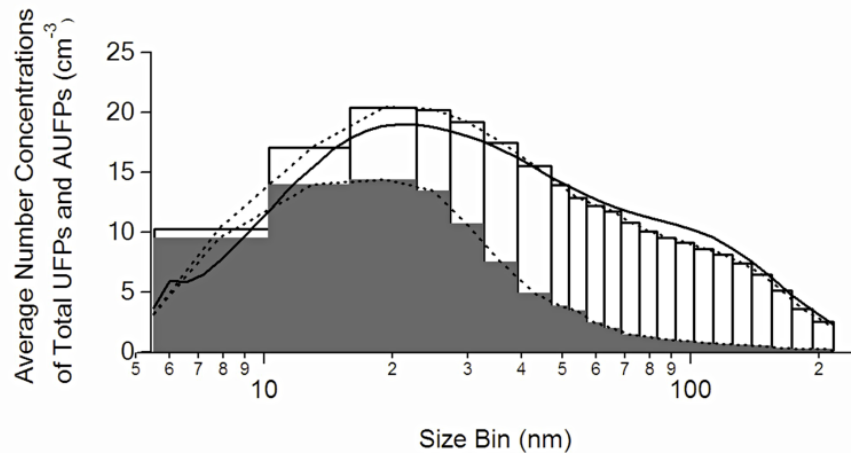


**Figure 5.4** The calculated lognormal size distribution of ambient total (white bar and dash line) and acidic particles (black bar and dash line) by DS+AFM method; and the average size distribution of ambient total particles measured by the SMPS+CPC (black solid line). The smooth continuous distribution is obtained by joining the bin mid-points.

**Table 5.1** Acidic particle and total particle number concentration and GMD measured by one group of detectors and the comparison with SMPS+CPC data during the field measurement at the urban site

Number of Particles (mean± SD) at 0.03 L/min flow rate							
Date & Time	ID	Number of 10×10 μm scanned areas	Acidic particles per scanned area (mean ± SD)	Total particles per scanned area (mean ± SD)	Ambient acidic PN (mean ± SD)× 10 <sup>4</sup>	Ambient total particles (mean ± SD)× 10 <sup>4</sup>	SMPS+CPC data (mean ± SD)× 10 <sup>4</sup>
22Dec. 12:00~25 Dec. 12:00 2010 (3 days)	A1	10	328 ± 130	547 ± 160	0.57 ± 0.23	1.75 ± 0.51	1.94 ± 0.88
	A2	10	381 ± 106	621 ± 201	0.66 ± 0.18	1.98 ± 0.64	
	A3	10	374 ± 126	519 ± 127	0.65 ± 0.22	1.66 ± 0.41	
	B1	15	75 ± 23	111 ± 38	0.74 ± 0.23	2.20 ± 0.75	GMD: 25 ± 3nm
	B2	15	64 ± 29	109 ± 46	0.63± 0.29	2.16 ± 0.91	
	B3	15	58 ± 19	123 ± 48	0.57 ± 0.19	2.43 ± 0.95	
	C1	20	38 ± 8	52 ± 16	0.74 ± 0.16	2.06 ± 0.64	
	C2	20	41 ± 12	60 ± 25	0.80 ± 0.23	2.38 ± 0.99	
	C3	20	37 ± 9	53 ± 24	0.72 ± 0.18	2.11 ± 0.95	
Average					<b>0.68 ± 0.21</b>	<b>2.08 ± 0.75</b>	

**Table 5.2** Acidic particle and total particle number concentrations and GMD in the size range of 5-200 nm measured by ten groups of DS detectors and the comparison with SMPS+CPC data during the field measurement at the urban site

Date & Time	Ambient acidic particles measured by DS+AFM (mean ± SD)× 10 <sup>4</sup>	Ambient total particles measured by DS+AFM (mean ± SD)× 10 <sup>4</sup>	Ambient total particles measured by SMPS+CPC (mean ± SD)× 10 <sup>4</sup>
22 Dec. 12:00 -25 Dec. 12:00 2010 (3 days)	0.68 ± 0.21 (GMD:19 ± 6nm)	2.08 ± 0.75 (GMD:24 ± 7nm)	1.94 ± 0.88 (GMD:25 ± 3nm)
25 Dec. 12:00 -27 Dec. 12:00 2010 (2 days)	1.37±0.32 (GMD:16 ± 5nm)	2.28± 0.82 (GMD:22 ± 5nm)	1.95 ± 0.99 (GMD:21 ± 2nm)
27 Dec. 12:00 -29 Dec. 12:00 2010 (2 days)	1.46±0.41 (GMD:15 ± 5nm)	2.69± 0.92 (GMD:25 ± 4nm)	2.97 ± 1.01 (GMD:26 ± 3nm)
29 Dec. 12:00 -31 Dec. 12:00 2010 (2 days)	1.03 ±0.35 (GMD:17 ± 7nm)	2.42± 0.89 (GMD:23 ± 4nm)	2.16 ± 1.11 (GMD:24 ± 3nm)
31 Dec. 12:00	0.69±0.28	1.59± 0.62	1.71 ± 0.79

-03 Jan. 12:00 2011 (3 days)	(GMD:20 ± 4nm)	(GMD:25 ± 7nm)	(GMD:23 ± 4nm)
03 Jan. 12:00 -05 Jan. 12:00 2011 (2 days)	1.17±0.39 (GMD:17 ± 4nm)	2.33± 0.77 (GMD:27 ± 4nm)	2.16 ± 1.28 (GMD:26 ± 3nm)
05 Jan. 12:00 -07 Jan. 12:00 2011 (2 days)	0.81 ±0.37 (GMD:16 ± 6nm)	1.93± 0.62 (GMD:26 ± 6nm)	1.61 ± 0.71 (GMD:25 ± 3nm)
07 Jan. 12:00 -10 Jan. 12:00 2011 (3 days)	0.59±0.27 (GMD:19± 4nm)	1.62± 0.56 (GMD:29 ± 5nm)	1.87 ± 1.05 (GMD:28 ± 3nm)
10 Jan. 12:00 -13 Jan. 12:00 2011 (3 days)	0.74±0.24 (GMD:20 ± 7nm)	1.98± 0.63 (GMD:26 ± 6nm)	1.84 ± 1.02 (GMD:27 ± 3nm)
13 Jan. 12:00 -15 Jan. 12:00 2011 (2 days)	1.10±0.37 (GMD:18 ± 5nm)	2.45± 0.84 (GMD:28 ± 6nm)	2.33 ± 1.36 (GMD:27 ± 3nm)
<b>Average</b>	<b>0.96 ±0.32</b> <b>(GMD:19 ± 5nm)</b>	<b>2.14± 0.74</b> <b>(GMD:25 ± 6nm)</b>	<b>2.05 ± 1.02</b> <b>(GMD:25 ± 3nm)</b>

By comparison, the average number concentrations of total ambient particles measured by the DS + AFM were in line with the values measured by the SMPS + CPC (*t*-test,  $p > 0.05$ ), and the calculated GMD of the particle size distribution from the DS data showed remarkable agreement with that obtained from SMPS (*t*-test,  $p > 0.05$ ) (see Table 5.2). Importantly, although the total PN concentration in the size range of 5.5-200 nm measured by the DS was consistent with the SMPS + CPC data (*t*-test,  $p > 0.05$ ), the PN concentration measured by the DS showed higher values in the size range of 6.5-47 nm and lower values in the size range of 47-200 nm than the SMPS + CPC data. The higher PN level measured by the DS for smaller ultrafine particles was associated with several factors. First of all, electrostatic forces have higher impact on smaller particles, and the deposition efficiency of charged particles is higher than neutralized or zero-charged particles. Hence, the charged smaller particles in the atmosphere could enhance the measured

PN concentrations by the DS. Secondly, since surface charge density of acidic particles is usually higher than that of non-acidic particles (e.g., Elimelech and O'Meliat, 1990), and acidic particles in the smaller size have the higher fraction than in the larger size of the total particles, electrostatic forces might cause more acidic particles to be deposited on the DS. Thirdly, subsequent evaporation of volatile species in particles would shift the size distribution to smaller size ranges, increasing the charging percentage of the particles entering the DS. Lastly, SMPS usually undermeasures smaller particles due to significant diffusion loss of smaller particles. As such, it is possible for the DS + AFM system to over-estimate the concentrations of the smaller particles due to the particle charge effect.

In addition, compared to that of the total particles, the size, at which the peak concentration of acidic particles was observed, was smaller. This meant that the size of acidic particles in ambient air was smaller than that of non-acidic particles. It could be partly explained by the fact that the fraction of acidic particles to the total particles varied in different size bins based on the AFM results. The highest fraction of acidic PN in total PN concentration was in the size range of 5.5-30 nm with a mean value of about 65%, in the size range of 30-100 nm the ratio of acidic PN to total PN concentration was 15%, the lowest fraction was in the size range of 100-200 nm with an average of about 8%. The result suggested that the acidic particles in ambient air were relatively fresh.

### **5.3 Summary and conclusions**

In this chapter, a DS+AFM method was developed to determine the number concentration of ambient acidic particles, based on the diffusion deposition of

ultrafine particles and detection of iron nanofilm detector for acidic particles. To calibrate the diffusive deposition efficiency of particles at the different detector locations in the diffusion sampler, the semi-empirical equations were obtained based on the combination of theoretical calculation and experimental data. It was found that (1) the experimentally measured deposition efficiencies were all higher than the theoretical values for the designed DS; (2) the stepwise deposition efficiency of particles in each size decreased with the increase in transport distance from the inlet; (3) the stepwise deposition efficiency of particles decreased with the increase in flow rate, showing negative power-law relationship at the first location; and (4) at different locations, the highest deposition efficiency of particles was shown in different sizes. The geometric mean diameter of the particle size distribution varied along the length of the sampler channel when sampling poly-disperse aerosols.

In the field measurement, the total particle number concentrations and size distributions measured by the DS+AFM showed good agreements with the measurement data of SMPS + CPC. Therefore, it is reasonable to assume that the number concentration and size distribution of acidic particles estimated by the DS+AFM method were reliable. Moreover, we found that the highest fraction of acidic particles to the total particles was in the size range of 5.5-30 nm with a mean value of 65%, while the lowest fraction was in the size range of 100-200 nm with an average of 8%. The result indicated that most acidic particles at this urban site were ultrafine particles and relatively fresh.

## **Chapter 6: Observation of new particle formation at a rural site**

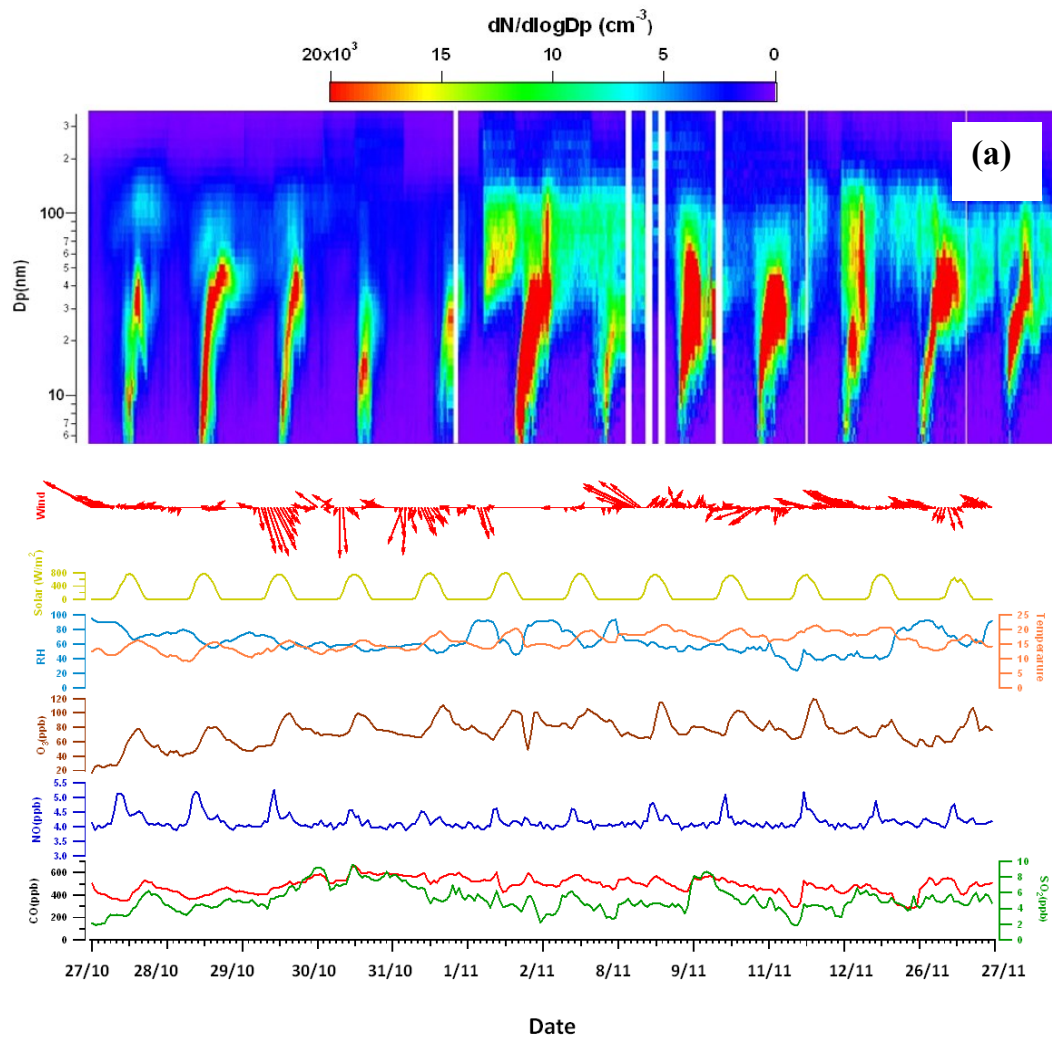
### **6.1 Introduction**

In this chapter, an intensive field measurement was conducted from 25 October to 29 November in 2010 near the summit of Mt. Tai Mo Shan (Mt.TMS; 640m a.s.l). The PN size distributions were characterized and the NPF events were classified based on their strength and growth of geometric mean diameter (GMD). Moreover, the favorable meteorological conditions and possible mechanisms for the nucleation and growth of new particles were discussed by analyzing concurrently-observed meteorological parameters, gaseous pollutants, major hydrocarbons (e.g., isoprene,  $\alpha$ -/ $\beta$ -pinenes, myrcene, limonene and aromatics), and carbonyl compounds i.e., formaldehyde, acetaldehyde and acetone.

### **6.2 Classification of the new particle formation and ozone pollution events**

Figure 6.1a shows the temporal variations of PN size distribution (5.5 – 350 nm), trace gases (SO<sub>2</sub>, NO, CO and O<sub>3</sub>) and meteorological conditions (solar radiation, T, RH and wind) during these NPF events in October and November 2010. According to the classification scheme developed by Dal Maso et al., (2005), the typical Class Ia events occurred on 27, 28, 29 October and 01 November, 2010 at Mt.TMS. The examples of Class Ib included 30 October, 02, 08 and 09 November, 2010. On 31 October, 11, 12 and 26 November, Class II events were observed. Figure 6.1b) shows the average diurnal

variations of particle number size distribution in NPF events and non-NPF events.



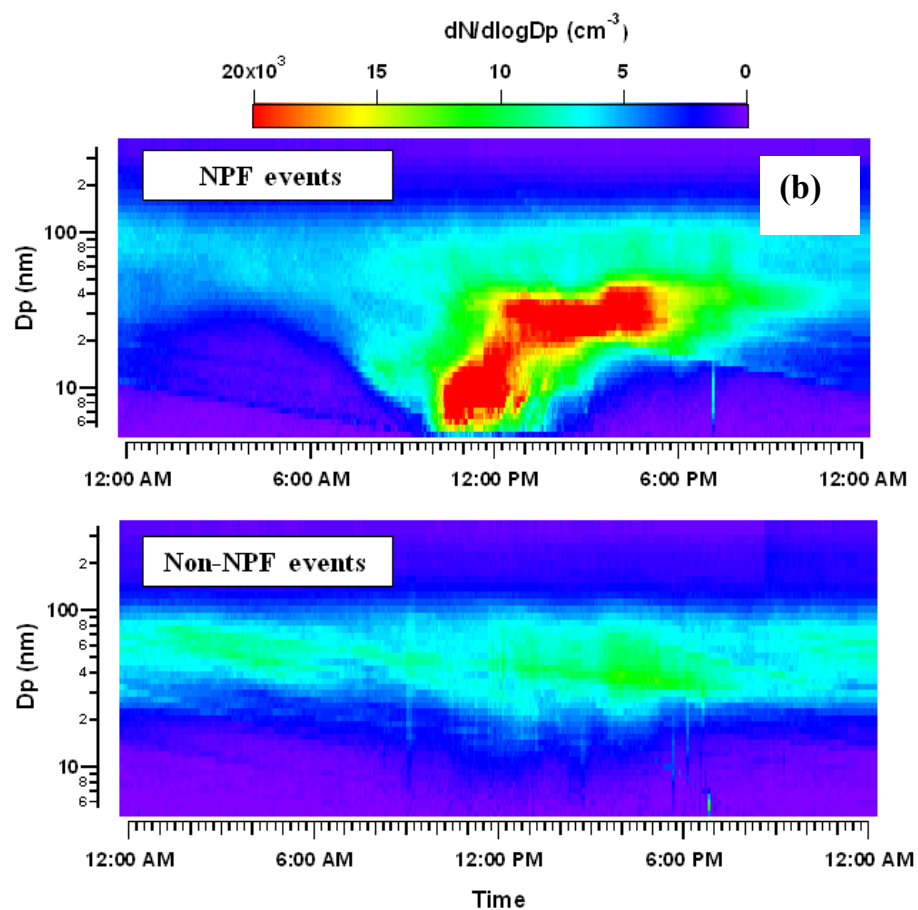


**Figure 6.1** (a) Temporal variations of PN size distribution (5.5 – 350 nm), trace gases ( $\text{SO}_2$ , NO, CO and  $\text{O}_3$ ) and meteorological conditions (solar radiation, T, RH and wind) during the NPF events in October/ November 2010; (b) Average diurnal variations of particle number size distribution in NPF events and non-NPF events.

Previous studies indicated that air pollution caused by ultrafine particulate matter and O<sub>3</sub> in the atmosphere of Hong Kong is severe (e.g., Wang et al., 2005; Guo et al., 2009). It is well-known that both biogenic and anthropogenic VOCs together with nitrogen oxides (NO<sub>x</sub>) are important precursors of surface-level O<sub>3</sub>, and the oxidation products of photochemical reaction may play a key role in determining the spatial and temporal features of the nucleation events. Hence, NPF events likely occur along with photochemical O<sub>3</sub> production. In this chapter, all the NPF events indeed occurred on the O<sub>3</sub> episode days, while a few non-NPF events were also observed on O<sub>3</sub> episode days. Based on the levels of particle number and/or O<sub>3</sub> collected from 25 October to 29 November, four different types of events were classified from the NPF and non-NPF events throughout the 35 sampling days. Table 6.1 summarizes the four different types of events including type1 (12 days): all NPF events (class Ia, Ib and II events) on O<sub>3</sub> episode days (maximum hourly O<sub>3</sub> mixing ratio  $\geq 90$  ppbv); type2 (4 days): non-NPF events on O<sub>3</sub> episode days; type3 (3 days): non-NPF events on non-O<sub>3</sub> episode days but with high particle number concentrations (PN concentration  $\geq 10^4 \text{cm}^{-3}$ ) and type4 (16 days): non-NPF events on non-O<sub>3</sub> episode days also with low levels of PN concentration. The hourly average O<sub>3</sub> mixing ratio, nucleation mode particle and total PN concentrations in the size range of 5.5-350 nm from 0800 to 1600 LT were higher on most NPF event days (type1) than on non-NPF event days with O<sub>3</sub> episodes (type2). Different from type1 and type2 events, the elevated PN concentration in type3 events was probably attributed to primary emissions from local sources, i.e., vehicle emissions.

**Table 6.1** Summary of the observed formation start time, the hourly average mixing ratios of trace gases (SO<sub>2</sub>, NO<sub>x</sub>, CO and O<sub>3</sub>), meteorological conditions (UV, T, RH and wind), total PN concentration (5.5 – 350 nm) and nucleation mode particle concentration (N<sub>nuc</sub>) in four different types of events classified from NPF event days (class Ia, Ib and II events) and non-NPF event days from 08:00 to 16:00 LT observed at Mt.TMS

Event type	Date	Observed NPF start time (LT)	O <sub>3</sub> (ppb)	SO <sub>2</sub> (ppb)	NO <sub>2</sub> (ppb)	NO (ppb)	CO (ppb)	Solar radiation (Wm <sup>-2</sup> )	Relative humidity (%)	Temperature (°C)	Wind direction speed/ (ms <sup>-1</sup> / °)	Total PN / N <sub>nuc</sub> concentration (cm <sup>-3</sup> ×10 <sup>4</sup> )
Type 1 (NPF + O <sub>3</sub> ) Day	27 Oct 2010 (Class Ia)	1100	62.5	3.9	8.1	4.0	406	522	75.6	14.6	3.5/332	1.92/0.60
	28 Oct 2010 (Class Ia)	1000	67.5	4.3	8.2	3.9	400	561	62.5	13.7	3.5/337	2.76/1.1
	29 Oct 2010 (Class Ia)	1030	79.1	5.7	9.5	3.8	476	546	61.5	14.8	2.6/302	2.07/ 0.52
	30 Oct 2010 (Class Ib)	1045	86.6	8.2	9.2	3.5	599	546	56.1	15.1	2.8/310	1.65/0.58
	31 Oct 2010 (Class II)	1020	84.6	5.0	10.2	3.6	557	539	69.5	17.0	2.0/336	1.01/0.10
	01 Nov 2010 (Class Ia)	1015	87.1	4.7	8.1	3.5	494	565	62.7	18.0	1.1/330	1.55/0.50
	02 Nov 2010 (Class Ib)	1015	93.1	5.1	8.2	3.5	551	548	64.7	18.0	1.7/301	0.76/0.15
	08 Nov 2010 (Class Ib)	1030	88.4	4.5	10.2	3.7	526	528	59.0	20.4	2.0/315	1.42/0.11
	09 Nov 2010 (Class Ib)	1035	88.9	5.6	8.4	3.6	518	515	53.9	18.9	1.3/332	1.18/0.16
	11 Nov 2010 (Class II)	1100	91.4	3.7	11.1	3.7	434	513	39.0	20.0	1.5/341	0.92/0.15
12 Nov 2010 (Class II)	1030	77.4	5.3	6.5	3.7	428	525	47.0	20.1	0.82/52	0.87/0.17	

	<b>26 Nov 2010 (Class II)</b>	1045	74.5	5.0	7.9	3.5	487	424	66.1	16.5	1.0/48	0.72/0.054
<b>Type 2 (Non-NPF + O<sub>3</sub>) Day</b>	<b>17 Nov 2010</b>	-----	77.8	4.4	10.6	4.0	639	451	80.5	17.5	1.5/334	0.65/0.010
	<b>18 Nov 2010</b>	-----	75.5	3.7	12.2	3.7	529	360	81.9	18.0	1.3/330	0.67/0.012
	<b>19 Nov 2010</b>	-----	78.6	5.0	12.8	3.7	694	424	81.5	18.3	1.4/331	0.78/0.018
	<b>27 Nov 2010</b>	-----	72.8	4.7	7.6	3.5	480	355	74.0	17.4	2.2/85	0.37/0.030
<b>Type 3 (Non-NPF + non- O<sub>3</sub> + high PN) Day</b>	<b>7 Nov 2010</b>	-----	56.0	6.7	20.3	4.2	718	424	79.2	20.6	0.42/267	0.97/0.024
	<b>21 Nov 2010</b>	-----	37.5	6.3	21.5	5.2	453	327	85.4	19.1	0.32/220	1.0/0.034
	<b>29 Nov 2010</b>	-----	51.1	8.6	31.4	8.0	578	230	87.0	18.3	0.44/288	0.99/0.013
<b>Type 4 (Non-NPF + non- O<sub>3</sub> + low PN) Day</b>	<b>Other 16 days</b>	-----	58.6	3.4	16.8	4.5	467	291	78.3	18.0	1.9/78	0.56/0.011

### 6.3 Comparison of NPF days and non-NPF days

To find out the favorable conditions for the NPF events, comparison of different parameters (i.e., meteorological conditions and gas phase concentrations) between NPF days and non-NPF days was made. Here the non-NPF days included non-NPF events on O<sub>3</sub> episode days (type 2), and on non-O<sub>3</sub> episode with both high and low PN concentration days (type 3 and type 4). Figure 6.2 shows the average diurnal variations of total PN concentration, SO<sub>2</sub>, NO<sub>x</sub>, CO, O<sub>3</sub> and meteorological conditions (solar radiation, RH, T and wind rose plots) during NPF event days and non-NPF event days over the whole sampling period at Mt.TMS, respectively.

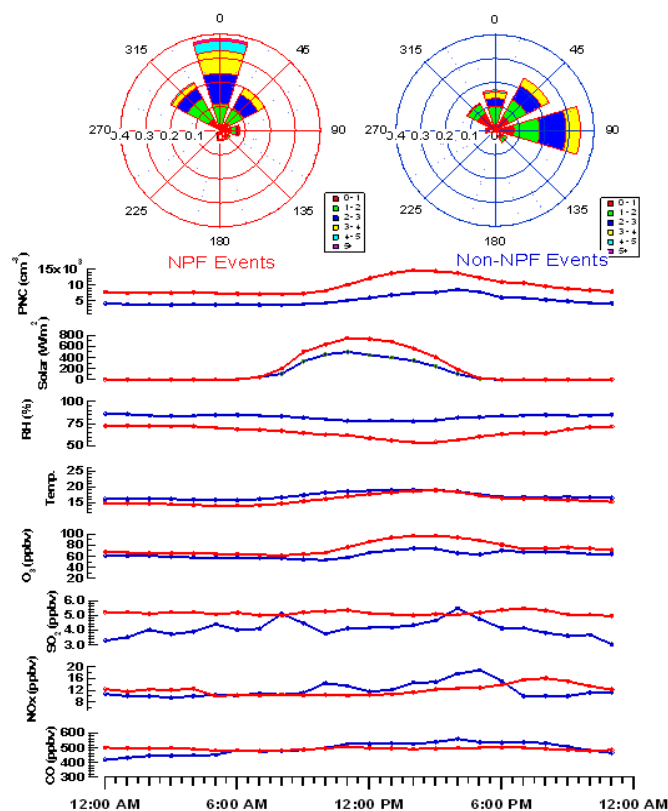


**Figure 6.2** Average diurnal variations of total PN concentration, trace gases (SO<sub>2</sub>, NO<sub>x</sub>, CO and O<sub>3</sub>) and meteorological conditions (solar radiation, RH, T and wind) during NPF event days and non-NPF event days over the whole sampling period at the Mt.TMS site.

### 6.3.1 Particle number concentration and diurnal variation

It was found that the diurnal pattern of PN concentration was different between NPF events and non-NPF events (Figure 6.2). In NPF events, the PN concentration began to rise at 10:00 ( $0.72 \times 10^4 \text{ cm}^{-3}$ ), reached its peak at 14:00 ( $1.5 \times 10^4 \text{ cm}^{-3}$ ), and then gradually decreased, similar to the diurnal pattern of  $\text{O}_3$ . In non-NPF events, the PN concentration showed a slow increase from 10:00, reached the peak value at 16:00 ( $\sim 0.85 \times 10^4 \text{ cm}^{-3}$ ), and then decreased. The peak value of PN coincided with peaks of  $\text{NO}_x$  and  $\text{SO}_2$ , indicating the influence of primary emissions from urban area on non-NPF days, especially for non-NPF events on high PN concentration days. As expected, the 24-hr average total PN concentration was significantly higher in NPF events ( $0.95 \times 10^4 \pm 0.13 \text{ cm}^{-3}$ ) than that ( $0.50 \times 10^4 \pm 0.06 \text{ cm}^{-3}$ ) in non-NPF events ( $p < 0.001$ ). And the average AUFPS number concentration was also higher in NPF events ( $0.25 \times 10^4 \pm 0.03 \text{ cm}^{-3}$ ) than that ( $0.16 \times 10^4 \pm 0.02 \text{ cm}^{-3}$ ) in non-NPF events. The PN values observed in this study were slightly lower than those reported at a site in the Po Valley area, Italy (Hamed et al., 2007), where the maximum total PN concentrations on NPF event days and non-NPF event days were  $2.4 \times 10^4 \text{ cm}^{-3}$  and  $(0.7\text{--}1.5) \times 10^4 \text{ cm}^{-3}$ , respectively, in the same season. However, at another site in the Po Valley, the average PN concentration for 5–800 nm particles during the NPF events was about  $1 \times 10^4 \text{ cm}^{-3}$  with a range of  $0.2 \times 10^4$  to  $2 \times 10^4 \text{ cm}^{-3}$  (Rodriguez et al., 2005), similar to the levels found in this study. In Pittsburgh, the average PN concentration for 3–500 nm particles was about  $2.2 \times 10^4 \text{ cm}^{-3}$  (Stanier et al., 2004b), a little higher than the observed values at Mt.TMS.

### 6.3.2 Effect of meteorological parameters on new particle formation

The maximum solar radiation on NPF event days ( $750 \text{ Wm}^{-2}$ ) was 50% higher than that ( $500 \text{ Wm}^{-2}$ ) on non-NPF event days (Figure 6.2), suggesting the association between solar radiation and NPF events. Indeed, all NPF events were initiated at about 10:00~11:00 when the solar radiation rapidly increased. This could be explained by the fact that photochemical reactions among various chemicals were facilitated by stronger solar radiation, leading to NPF events. The observations are consistent with other studies (Stanier et al., 2004b; Hamed et al., 2007; Guo et al., 2008; Modini et al., 2009). Stanier et al., (2004b) claimed that nucleation was typically observed starting around 0900 EST in Pittsburgh, USA. In eastern Australia, the NPF events usually began at 10:00~11:00 LT (Guo et al., 2008; Modini et al., 2009), except for one case in which a particularly strong nucleation event began in early morning (0800) (Modini et al., 2009). In this study, the observed start time of NPF events was defined as the time when the 5.5 nm size particle concentration (the minimum detectable size for our aerosol instrument) remarkably increased. Since it takes time for newly formed particles (about 1 nm in diameter) to grow into 5.5 nm, the real start time of these NPF events could be earlier than the observed start time, and the time lag varies under different atmospheric conditions. The fitted time lag was defined using the time series of the formation rate of 5.5 nm particles and the sulfuric acid concentration in each NPF event (Riipinen et al., 2011) (see Table 6.2). Based on the observed start time and the fitted time lag for each NPF event, the estimated start time of these NPF events were ranged from 09:50 to 10:40 LT during this sampling session.

Interestingly, the average temperature was slightly lower in the NPF events than that in the non-NPF events (Figure 6.2), similar to those observed at different locations in Finland (Boy and Kulmala, 2002; Komppula et al., 2003; Vehkamäki et al., 2004) and in summer in Italy (Hamed et al., 2007). Contrarily, higher temperatures have been associated with the nucleation events in east and south Germany (Birmili and Wiedensohler, 2000; Birmili et al., 2003), and in spring, autumn and winter in Italy (Hamed et al., 2007). By investigating the fraction of GR explained by maximum sulfuric acid condensation in this study (detailed in Section 3.3.2), higher fractions (21~57%) of sulfuric acid contribution to GR was found in the NPF events at lower temperature (13.7~18 °C), while lower fractions (9.2~22%) was determined in the NPF events with higher temperature (18.9~20.4 °C), in line with the findings of Kurtén et al., (2007) who found that in the atmosphere, the majority of sulfuric acid molecules prefer to bind with water molecules under low temperature conditions. The result suggests that the lower temperature at the start time of the NPF events may enhance the nucleation of sulfuric acid with water vapor.

The RH on average was lower on NPF event days than on non-NPF event days (Figure 6.2). Low RH, frequently down to near 50% (at noon hours), was observed during nucleation events, similar to the RH levels in the Po Valley area, Italy (Hamed et al., 2007), and in clean areas in Hyytiälä station, Finland (Boy and Kulmala, 2002). This is a strong indication that the NPF is favored under low RH. This could be partly explained by the fact that lower RH days usually have less clouds causing increased solar radiation to produce more OH radicals to form more condensable vapors (Hamed et al., 2007). Another

proposed reason could be that at high RH, condensation sink increased due to hygroscopic growth of the pre-existing particles. Sub-3 nm clusters could be scavenged to inhibit the nucleation at high RH (Hamed et al., 2011).

During the NPF event days, the wind was mainly from the north direction, while east winds were more frequently observed on the non-NPF event days (Figure 6.2). To investigate the transport pathways of the air masses arriving at the Mt.TMS site during the sampling period, we analyzed back trajectories for NPF days and non-NPF days. The analysis was done by using HYSPLIT 4 (Hybrid Single-Particle Lagrangian Integrated Trajectory) model developed by NOAA Air Resource Laboratory (ARL) (Draxler and Hess, 1998). Back trajectories arriving at 10:00 with 1000 m arrival height were calculated one day backward in time. Figure 6.3 shows the position of the air parcel at 24-h back in time for NPF and non-NPF days, respectively. The air masses were classified into three major categories on the NPF days: i) air masses originated from inland China (track 1, accounting for 56% of the total trajectories); ii) air masses originated from Yangtze River Delta with a faster movement than track 1 (track 2, 32%); and iii) air masses originated from the South China Sea with a very slow movement (track 3, 12%). The track 1 mainly occurred at daytime hours on NPF event days, and the average mixing ratios of SO<sub>2</sub>, O<sub>3</sub>, CO and N<sub>nuc</sub> concentrations at Mt.TMS were 4.9 ppbv, 87 ppbv, 480 ppbv and  $0.52 \times 10^4 \text{ cm}^{-3}$ , respectively. The air in track 1 had the highest O<sub>3</sub> mixing ratio and N<sub>nuc</sub> concentration, followed by the air in track 3 (74 ppbv for O<sub>3</sub>,  $p < 0.001$  and  $0.36 \times 10^4 \text{ cm}^{-3}$  for N<sub>nuc</sub>,  $p < 0.05$ ) and air in track 2 (66 ppbv for O<sub>3</sub>,  $p < 0.001$  and  $0.17 \times 10^4 \text{ cm}^{-3}$  for N<sub>nuc</sub>,  $p < 0.001$ ), indicating that air masses originated from track 1 were favorable to the NPF events. Nucleation

processes in the atmosphere tend to produce new particles that are more regionally dispersed over an urban or rural area. As the wind was mainly from the north direction during the NPF event, besides the NPF at Hong Kong, it was also possible that the increase of  $N_{\text{nuc}}$  concentration was due to the transport of newly formed particles from other places. On the other hand, there were two types of air masses classified on non-NPF days: i) track 1 originated from eastern China coast with a slow movement, accounting for 92% of the total air masses; and ii) track 2 originated from western Pacific Ocean and arrived at Mt.TMS with a much faster movement, accounting for 8% of the total air masses. The average mixing ratios of  $\text{SO}_2$ ,  $\text{O}_3$  and  $N_{\text{nuc}}$  concentration in track 1 were 4.0 ppbv, 87 ppbv, and  $0.05 \times 10^4 \text{ cm}^{-3}$ , respectively, while they were 3.6 ppbv, 56 ppbv, and  $0.02 \times 10^4 \text{ cm}^{-3}$ , respectively in track 2. The higher  $\text{O}_3$  (87 ppbv) and CO (640 ppbv) values in track 1 air were mainly due to regional transport from eastern China. In contrast, low  $\text{SO}_2$  (3.6 ppbv), CO (421 ppbv),  $\text{O}_3$  (56 ppbv) and high RH (83%) levels in track 2 were caused by the strong winds originated from western Pacific Ocean, which brought clean marine air and scattered rain to the sampling site. The back trajectory results are consistent with the rose plot analysis which found that air masses associated with NPF events were mainly from northwestern to northeastern directions.

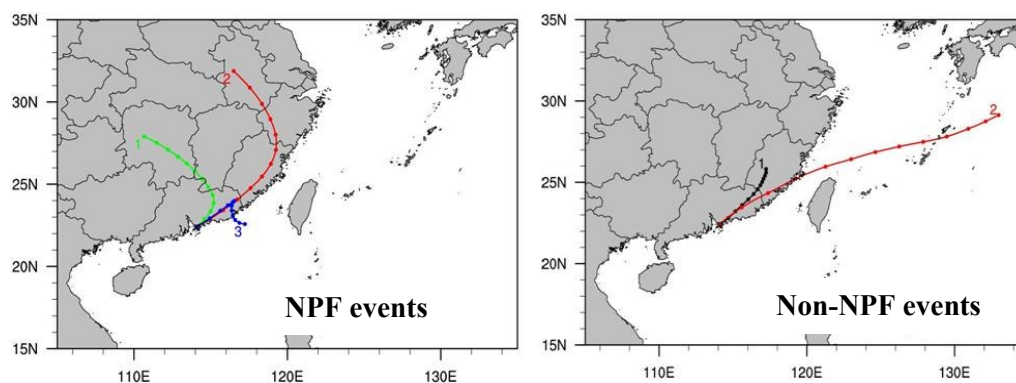


**Figure 6.3** Back trajectories for Mt.TMS at the 1000 m height level on NPF event days and non-NPF event days

### 6.3.3 Effect of gas concentrations on new particle formation

The hourly average  $O_3$  mixing ratios were higher on NPF event days than the corresponding values on non-NPF event days during daytime hours (i.e., 1000 – 1800 LT) (Figure 6.2). Also, the diurnal pattern of  $O_3$  mixing ratio was consistent with that of PN concentration on the NPF event days, suggesting that  $O_3$  and NPF had similar sources or formation mechanisms, most likely the photochemical reactions among the precursors (i.e., VOCs,  $NO_x$  and  $SO_2$ ) of  $O_3$  and NPF. As such,  $O_3$  could also be an important indicator for nucleation event occurrences. In addition,  $O_3$  could be the precursor of NPF as it is responsible for the formation of condensable species via direct reactions with VOCs, and indirect generation of other oxidants (i.e., OH and  $HO_2$ ) upon photolysis.

All the hourly average  $SO_2$  mixing ratios were higher on the NPF event days than on the non-NPF event days, except for the values at 08:00LT and 16:00 LT, which were likely related to primary emissions. The average mixing ratio on NPF event days and non-NPF event days was  $5.2 \pm 0.2$  ppbv and  $4.2 \pm 2.5$  ppbv, respectively. The large variations of the  $SO_2$  mixing ratio on non-NPF

event days were caused by some high SO<sub>2</sub> levels observed on non-NPF days with high PN concentrations (type 3) (Table 6.1), due to regional transport and/or local emissions. When the non-NPF days with high PN concentrations (type3) were excluded from the total non-NPF event days, the average SO<sub>2</sub> mixing ratio on non-NPF days became  $4.2 \pm 0.4$  ppbv, lower than that on the NPF event days. For NPF events, SO<sub>2</sub> is needed for the production of sulfuric acid, which participates in the nucleation and growth of stable nm-sized clusters. The higher SO<sub>2</sub> found in the NPF events implied that SO<sub>2</sub> might be favorable to the nucleation. However, by comparing the SO<sub>2</sub> levels in the NPF events (type1) with those in the non-NPF events with high PN concentrations (type 3), we found that the average SO<sub>2</sub> mixing ratio in non-NPF events with high PN concentration (type 3) was higher than that in NPF events (type 1) (Table 6.1,  $p < 0.05$ ), indicating that only a high SO<sub>2</sub> level was not sufficient for NPF. Other factors such as less pre-existing large particles and strong solar radiations (see Table 6.1) were also required.

It was found that the average daytime NO<sub>x</sub> value ( $11 \pm 1.3$  ppbv, daytime NO<sub>2</sub>:  $7.1 \pm 0.8$  ppbv) was lower on NPF event days than that ( $14 \pm 1.6$  ppbv, daytime NO<sub>2</sub>:  $9.2 \pm 1.5$  ppbv,  $p < 0.001$ ) on non-NPF event days during the process of formation and growth (Figure 6.2). The stronger solar radiation on NPF event days than on non-NPF event days was probably one of the reasons for the lower NO<sub>2</sub> levels on the NPF event days. The increase in solar radiation would promote the decay of NO<sub>2</sub> mixing ratios via the complex photochemical reactions, consistent with the negative correlation ( $R = -0.86$ ,  $p < 0.001$ ) between the daytime NO<sub>2</sub> values and solar radiation on the NPF event days. On non-NPF event days, the daytime NO<sub>2</sub> mixing ratios were

higher than the corresponding hourly values on the NPF event days, and had a peak at 18:00 LT, suggesting the possible influence of primary emissions transported to the site from the region and/or local urban areas via mesoscale recirculation.

#### **6.4 Characteristics of new particle formation and growth**

Table 6.2 shows the formation rate, growth rate and condensation sink of each NPF and growth event observed at Mt.TMS. The correlations of particle formation rate, growth rate and condensation sink with meteorological parameters, inorganic trace gas concentrations ( $O_3$ ,  $SO_2$ ,  $NO_x$  and  $CO$ ), biogenic VOCs (BVOCs), anthropogenic VOCs (AVOCs), and carbonyl compounds are presented in Table 6.3. The correlations of sulfuric acid and the VOC oxidation products with the formation rate and growth rate for each NPF event were particularly investigated in this section.

In this study, the formation rate (FR) at 5.5 nm was estimated from the increase of 5.5–10 nm PN concentration between the event start time and the time when the PN concentration exhibited a maximum during the NPF event. Based on the calculations, the FR values varied between 0.044 and 10.2  $cm^{-3}s^{-1}$ . The estimated average FR for Class Ia event was about 5.6  $cm^{-3}s^{-1}$ , higher than that of Class Ib (4.2  $cm^{-3}s^{-1}$ ) and Class II (1.1  $cm^{-3}s^{-1}$ ), indicating high FRs of nucleation mode particles in rural areas like the Mt.TMS site. The average growth rate (GR) for the nucleation events was calculated by the slope of GMD against time during the period of particle growth from 5.5 to 25 nm. By computation, the GRs of Class Ia events observed at Mt.TMS were from 3.0 to 5.4  $nm h^{-1}$  (average 4.4  $nm h^{-1}$ ), while the GRs of Class Ib events ranged from 1.5 to 4.5  $nm h^{-1}$  (average 2.9  $nm h^{-1}$ ), and from 1.8 to 8.4  $nm h^{-1}$

(average  $4.3 \text{ nm h}^{-1}$ ) for Class II events, all in line with the range of new particle growth rates observed in rural/suburban locations i.e.,  $1\text{--}10 \text{ nm h}^{-1}$  (Kulmala et al., 2004a).

#### **6.4.1 Case study-typical new particle formation and growth event at Mt.TMS**

In order to give a visible picture of NPF and growth processes from the beginning to the end, one Class Ia NPF event intensively occurred on 28 October, 2010 was selected for the case study. New particle formation event (nucleation mode) on 28 October was clearly observed after raining on 27 October, in line with the fact that nucleation events often occur after a sharp decrease in concentrations of pre-existing particles with large surface area (Guo et al., 2008; Liu et al., 2008). The minimum temperature of 12.5 degrees recorded on 28 October was the lowest in October since 1988. The NPF started when the wind speed increased to a maximum value (i.e.,  $5.26 \text{ ms}^{-1}$ ) (09:00LT). At the same time, slow increase in  $\text{SO}_2$ , decrease in CO (see Figure 6.4), and rise of the calculated boundary layer height were observed (Figure 6.5), indicating that these variations accompanied with the NPF were likely a result of breakup of the morning inversion that mixed  $\text{SO}_2$ -enriched and CO-depleted air from aloft and diluted the accumulated urban emissions (Zhang et al., 2004a). As shown in Figure 6.4, the nucleation mode appeared in the measurement range at about 10:00 LT and increased substantially with an observable growth rate ( $3.0 \text{ nm h}^{-1}$ ). The nucleation mode particle concentration ( $N_{\text{nuc}}$ ) increased rapidly from  $\sim 0.13 \times 10^4 \text{ cm}^{-3}$  to  $\sim 2.4 \times 10^4 \text{ cm}^{-3}$  at noon with an average formation rate ( $J_{5.5}$ ) of  $6.9 \text{ cm}^{-3}\text{s}^{-1}$ . Since the concentration of around  $0.2\text{--}1 \times 10^6 \text{ cm}^{-3}$  of  $<5 \text{ nm}$  particles is needed to

induce a growth rate of  $1\text{nmh}^{-1}$  by self-coagulation (Kulmala et al., 2004b), the initial nucleation mode particle concentration of  $< 3 \times 10^4 \text{ cm}^{-3}$  in this event indicated that self-coagulation only made a minor contribution to the particle growth. After 14:00, the GR decreased whereas the CS increased from 0.021 to  $0.053 \text{ s}^{-1}$ , suggesting the increase in large surface area particles might have scavenged potential condensable vapors responsible for particle growth. After 16:00, the total PN concentration decreased gradually to the background at 22:00. Additionally, correlation of  $N_{\text{nuc}}$  with secondary pollutant  $\text{O}_3$  ( $R = 0.70$ ,  $p < 0.001$ ) was much higher than that with primary pollutants i.e.,  $\text{SO}_2$  ( $R = 0.17$ ,  $p < 0.01$ ),  $\text{CO}$  ( $R = 0.06$ ,  $p < 0.01$ ) and  $\text{NO}$  ( $R = 0.23$ ,  $p < 0.01$ ), suggesting that the NPF event was likely associated with the photochemical formation via VOC oxidation processes, rather than direct emissions from urban sources.

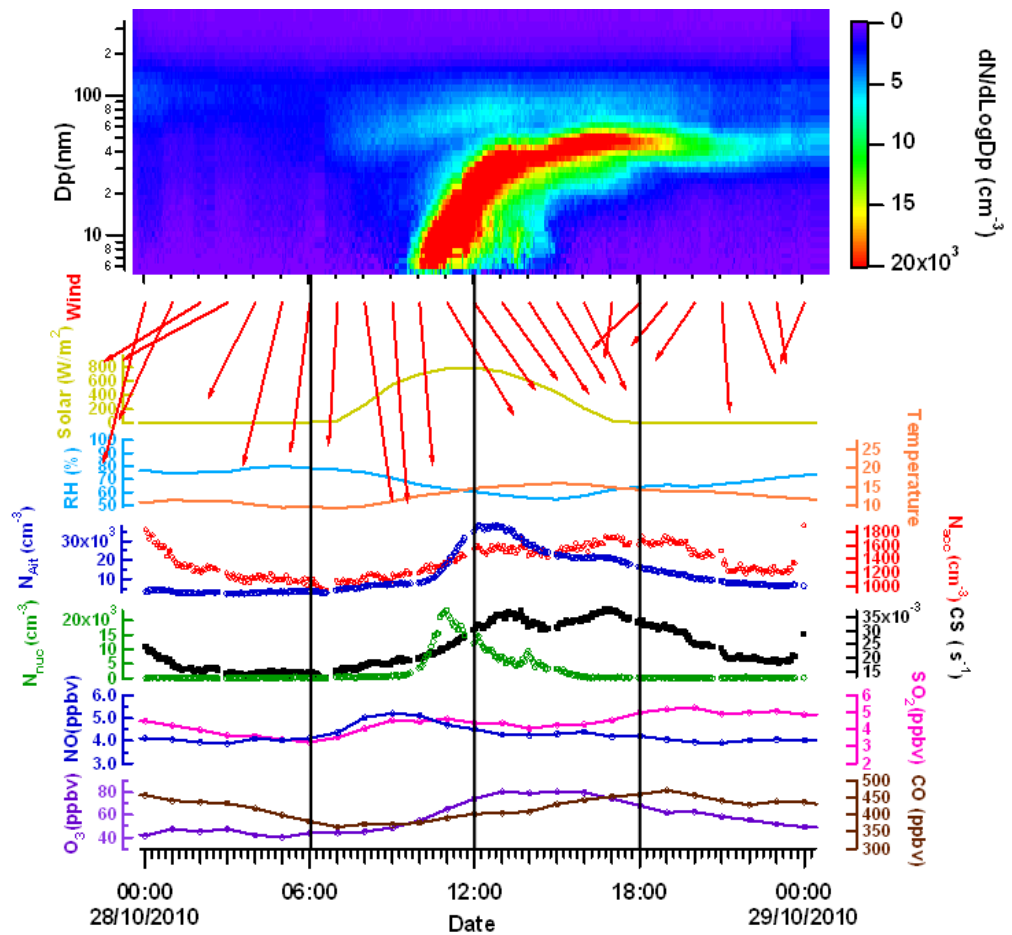


**Figure 6.4** Contour plots of the average diurnal variations of particle size distribution, the meteorological conditions and the concentrations of airborne pollutants on 28 October 2010 at Mt.TMS. From top to bottom, the parameters are: (i) Particle size distribution; (ii) Wind direction and speed (iii) Solar radiation; (iv) Temperature and relative humidity; (v) Number concentrations of Aitken mode and accumulation mode particles; (vi) Number concentration of nucleation mode particles and condensation sink, (vii) NO and SO<sub>2</sub>; (viii) O<sub>3</sub> and CO.

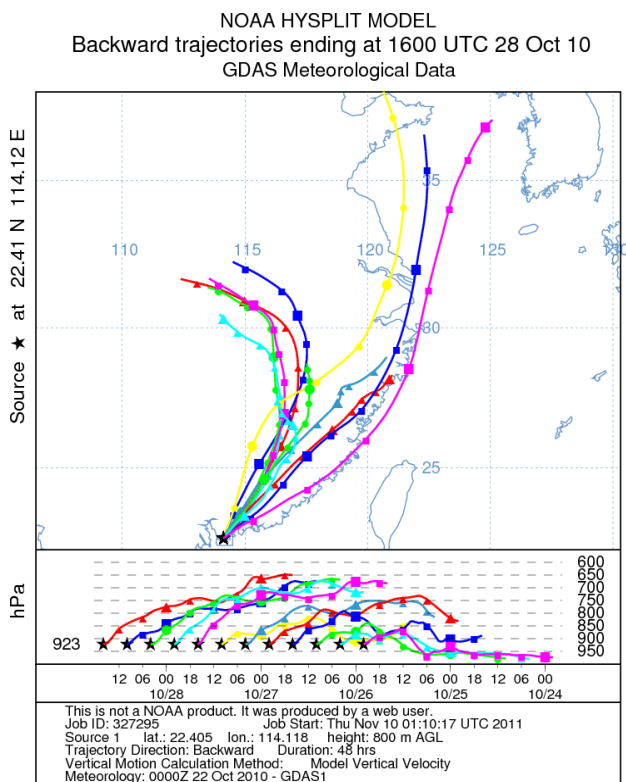


**Figure 6.5** 72h back-trajectories calculated during the nucleation mode particle formation event on 28 October, 2010 at Mt.TMS.

Given that the transformation from gas-phase pollutants to nucleation mode particles requires sufficient time, there may be a delay between the measured gaseous pollutants i.e.,  $\text{SO}_2$  and the formation of nucleation mode particles. Indeed, a much better correlation between  $\text{H}_2\text{SO}_4$  proxy and  $J_{5.5}$  with 0.8-hour time lag was found (see Table 6.2), suggesting the possible involvement of  $\text{H}_2\text{SO}_4$  vapor or/and  $\text{SO}_2$  oxidation products in this nucleation event. More detailed discussion is given in Section 6.4.2.

The variations of organic aerosol precursors i.e., VOCs and carbonyls were preliminarily investigated on 28 October. The concentrations of BVOC and AVOC species i.e., the potential precursors of secondary organic aerosols (SOA), started to increase at  $\sim 07:00\text{LT}$ , reached the maxima at  $\sim 13:00\text{LT}$  (i.e., BVOCs: isoprene 96 pptv,  $\alpha$ -pinene 24 pptv,  $\beta$ -pinene 6 pptv, myrcene 5 pptv

and limonene 329 pptv; and AVOCs: propene 510 pptv, toluene 6079 pptv, ethyltoluenes 180 pptv and triethylbenzenes 246 pptv). The start time for the increase in VOC species (07:00LT) were about 3 hours earlier than the time when the 5.5 nm nucleation mode particles started to increase (10:00LT). It is noteworthy that there is a time delay before a VOC turns to condensable species that could promote particle to grow to the detectable size of 5.5 nm for the instrument. The delayed time depends on the production rate of the condensational vapor from VOCs and on the growth rate of the particle from cluster into 5.5 nm. It is known that the oxidation products of BVOCs and AVOCs have a potential contribution to the NPF and growth (Griffin et al., 1999; Kulmala et al., 2004a, Hatch et al., 2011). In this event, it was found that the concentrations of the measured BVOCs versus  $N_{\text{nuc}}$  showed a power-law relation with a power exponent between 1 and 3. Moreover, during all the NPF events, the exponents of isoprene,  $\alpha$ -pinene and  $\beta$ -pinene with  $N_{\text{nuc}}$  also fell into the range of 1-3 in this study (see Figures 6.6 a & b). Direct evidences on the participation of organic vapors in the nucleation process have been obtained in laboratory experiments (e.g., Zhang et al., 2004b) and field measurements (e.g., Paasonen et al., 2010). These presented exponents in this study are not the nucleation coefficients of organic vapor concentrations and  $N_{\text{nuc}}$ . Nevertheless, our results at least shed the potential contribution of organic compounds on atmospheric nucleation. More detailed discussion about the characteristics of contribution of VOCs on the growth rate is given in Section 6.4.3.

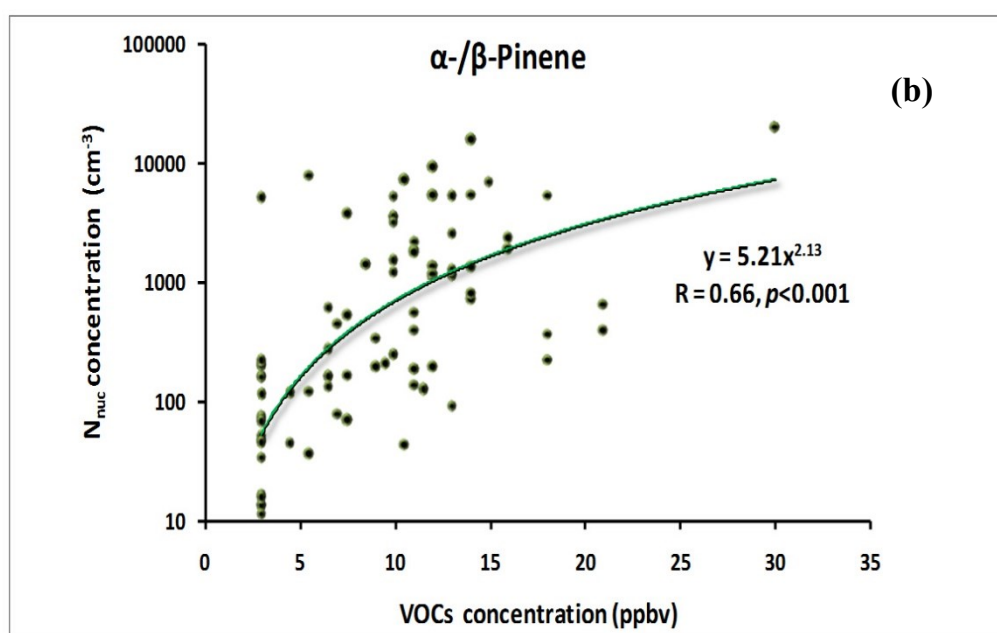
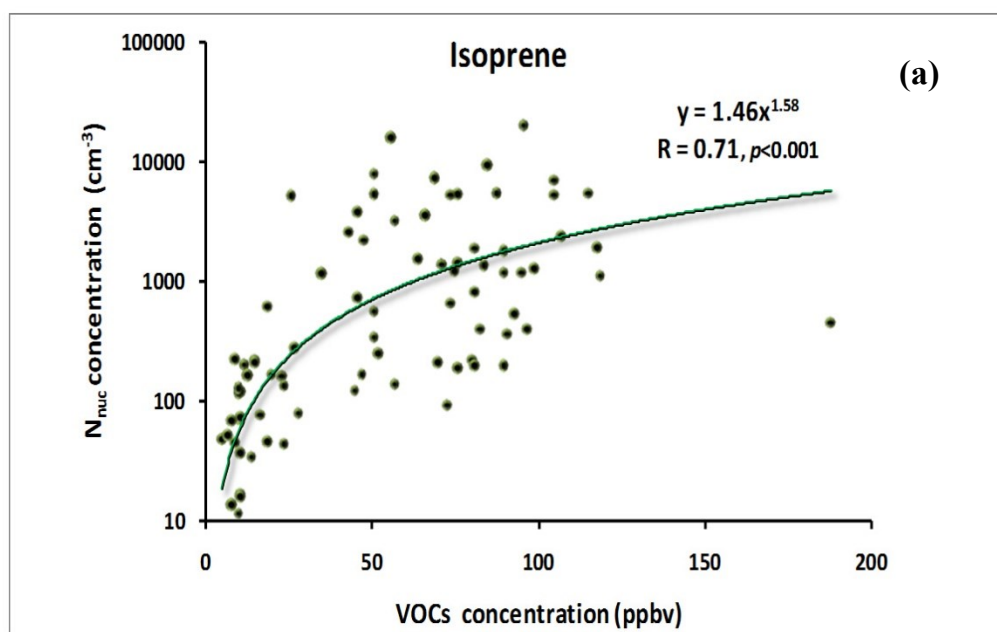


**Figure 6.6** Power-law relationships between concentrations of the measured BVOCs, i.e., (a) isoprene and (b)  $\alpha$ -/ $\beta$ -pinene and  $N_{\text{nuc}}$  during all NPF events. The power exponent, correlation coefficient and  $p$ -value between measured BVOCs and  $N_{\text{nuc}}$  are also shown in the fitted lines.

### 6.4.2 Sulfuric acid vapor

The real nucleation rate ( $J_{\text{real}}$ ) and the particle growth rate are both expected to be positively correlated with “non-volatile” vapor concentrations (Kulmala et al., 2004a). As already discussed in section 3.2, we are unable to measure  $J_{\text{real}}$  due to instrumental limitation. Nonetheless, it would be useful to study the relationship between measured gaseous compounds and the calculated  $J_{5.5}$ . In this study,  $J_{5.5}$  had positive relationships with gas phase  $\text{SO}_2$  and solar radiation (Table 6.3). Since the product of ultraviolet radiation and  $\text{SO}_2$  (i.e.,  $\text{UV} \times \text{SO}_2$ ) can be used as a surrogate parameter for  $\text{H}_2\text{SO}_4$  production (Petäjä et al., 2009), the positive relationships of  $J_{5.5}$  with  $\text{SO}_2$  and solar radiation suggested that concentration of sulfuric acid had a contribution to the nucleation mode particle (5.5 nm) formation. Figure 6.7 shows a plot of the estimated particle formation rate  $J_{5.5}$  vs. the sulfuric acid proxy calculated by Eq. 3.11) (in logarithmic scale). The sulfuric acid proxy concentrations here had been delayed by the fitted time lags for each NPF event ranging from 0.2~0.8 hours. Moderate correlation coefficients  $R$  ranging from 0.49 to 0.79 with all  $p < 0.05$  were observed (see Figure 6.7 and Table 6.2). Several studies have analyzed the slope of  $\log(\text{H}_2\text{SO}_4)$  vs.  $\log(J_3)$  because this could in principle reveal the number of sulfuric acid molecules required for a critical, thermodynamically stable cluster as well as give hints on the acting nucleation mechanism. These studies have observed slopes between 1 and 2 (i.e., exponent  $n_{J_3}$  between 1 and 2) (Weber et al., 1999; Kulmala et al., 2006; Sihto et al., 2006; Kuang et al., 2008). As shown in Figure 6.7 and Table 6.2, the optimal fitted line had a slope of about 1.3 and the exponent  $n_{J_{5.5}}$  for all NPF events never exceeded 2 in this study, indicating reasonable consistency with

earlier studies. The results suggested that the activation of stable clusters and/or kinetic nucleation were possibly the mechanisms for atmospheric particle formation.

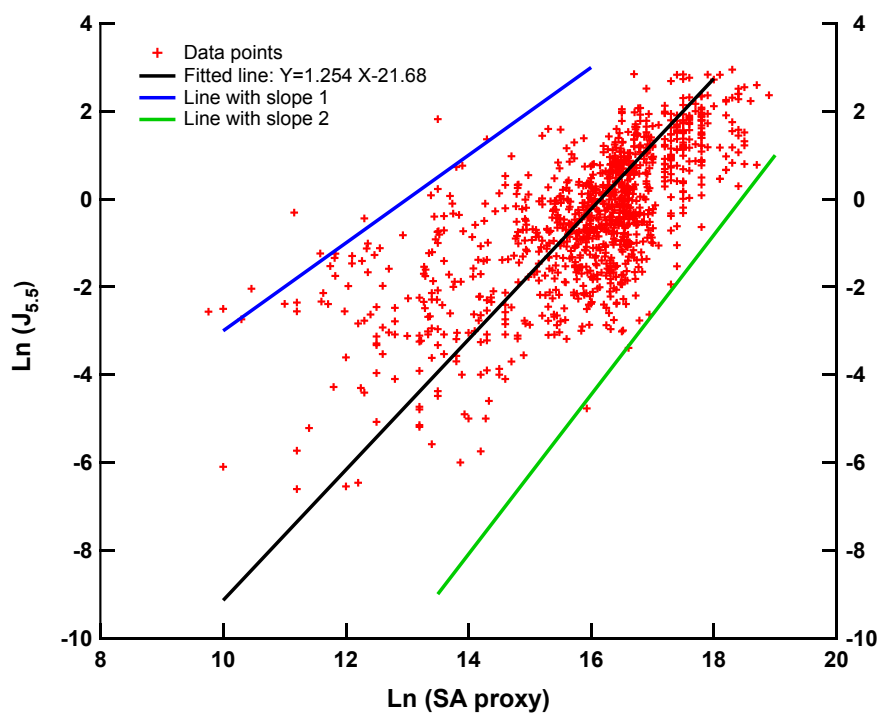


**Figure 6.7** The logarithm of formation rate  $J_{5.5}$  estimated from particle measurements versus the logarithm of the sulfuric acid proxy (4 minutes averages) during the nucleation events from 0600~1600 LT. Sulfuric acid proxy concentrations have been delayed by the fitted time lags. Lines with slopes 1 and 2 (corresponding to values 1 and 2 in the exponent  $n_{J_{5.5}}$ ) are also shown.

Apart from the connection with particle nucleation, the  $\text{H}_2\text{SO}_4$  vapor has also been found to take part in the particle growth. Weber et al., (1997) estimated the growth rate of nucleation mode particles from the time taken between the increase in gas phase sulfuric acid concentration and the increase in 3 nm particle concentrations. The observed growth rates of 1–2 nm  $\text{h}^{-1}$  were approximately ten times faster than those calculated assuming condensational

growth caused by sulfuric acid and water. In our calculations, we determined the observed growth rates from the SMPS data plots in the beginning of the event. Table 6.2 gives the fraction of sulfuric acid contribution to GR during each nucleation event, where the measured GR, estimated sulfuric acid concentration ( $C_{sa}$ ) and the sulfuric acid concentration needed for GR of 1 nm/h ( $C_o$ ) considering the influence of relative humidity (Nieminen et al., 2010) in each nucleation event are shown. The fraction contribution (FC) of sulfuric acid to GR in all NPF events ranged from 9.2% to 52.5%, showing large variations of sulfuric acid contribution to the observed GR during these NPF event days. Meanwhile, no direct correlation between observed GR and sulfuric acid concentration was found, indicating that the condensation of sulfuric acid vapor for particle growth was influenced by the atmospheric conditions i.e., solar radiation, water vapor and background PN concentration.

To further investigate the key atmospheric conditions behind the nucleation events, we utilized the parameterization approach described by Stanier et al., (2004b), who suggested that favorable conditions for nucleation can be described using a product of UV radiation and sulfuric dioxide (its increase indicates increase of sulfuric acid concentration), and the condensation sink. Figure 6.8 shows scatter plot of  $UV \times SO_2$  versus CS during the NPF events (red dots) and non-NPF events at Mt.TMS. For most of the NPF event days, the data points lay to the right of the diagonal line. The threshold (line) was calculated according to the model-based correlations in Pirjola et al., (1999) under the ground-level conditions. This model was designed to predict the required  $H_2SO_4$  production rates for nucleation and growth as a function of CS, RH and temperature. The lower right region

indicated more favorable conditions to nucleation than upper left region. As expected, the relatively low CS values on NPF days compared to those on non-NPF days were the favorable conditions for nucleation at this site. When the  $UV \times SO_2$  product increased and the CS values decreased, the nucleation events were likely observed. The criterion of Stanier et al., (2004b) indicates that low enough CS value is needed together with high enough sulfuric acid production, in agreement with our findings that  $SO_2$ , solar radiation and CS inverse have positive relationships with FR (Table 6.3). At Mt.TMS, the NPF events occurred with  $SO_2$  mixing ratios ranged from 4.0~5.5 ppbv during the sampling period (October/November). Wang et al., (2005) reported that the monthly average mixing ratio of  $SO_2$  from August 2001 to December 2002 at a background site in Kong Hong was 7.5 ppbv in October and 11 ppbv in November, respectively, suggesting that the  $SO_2$  background concentration in the PRD region was abundant for the required  $SO_2$  in nucleation events. Hence, low enough CS value and strong UV radiation are favorable conditions or even more important factors for NPF occurrence at this sampling site.

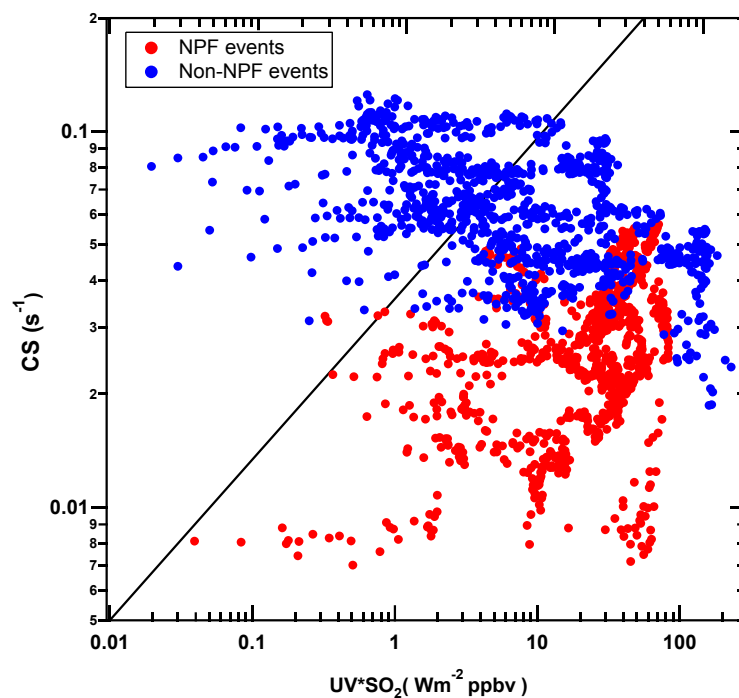


**Figure 6.8** Scatter plot of  $UV \cdot SO_2$  versus condensation sink during the NPF events (red dots) and non-NPF events (blue dots). Condensational sink ( $y$  axis-left) is plotted against the product of ultraviolet light intensity and  $SO_2$  concentration ( $x$  axis). Four-minute averaged values are plotted from the event start time to the event end time on NPF event days. On non-NPF event days, a time range from 08:00 to 16:00LT is applied.

**Table 6.2** Particle formation rate ( $J_{5.5}$ ), growth rate (GR), minimum and maximum condensation sink (CS), sulfuric acid (SA) vapor concentration (Csa), the SA vapor needed for 1 nmh<sup>-1</sup> particle size growth (Co), fractional contribution of SA vapor to particle growth (FC), fitted time delay ( $\Delta t$ ) and the exponent ( $n_{J5.5}$ ) for the correlation of  $J_{5.5}$  with sulfuric acid for each NPF event day covering 06:00-18:00 LT with  $p$ -value of the t-test.

Date		$J_{5.5}$ (cm <sup>-3</sup> s <sup>-1</sup> )	GR (nmh <sup>-1</sup> )	CS (s <sup>-1</sup> )	Csa (× 10 <sup>6</sup> cm <sup>-3</sup> )	Co (× 10 <sup>6</sup> cm <sup>-3</sup> )	FC (%)	$\Delta t$ (h)	$n_{J5.5}$	R $p$ -value
Class Ia	27 Oct 2010	5.9	5.4	0.021~0.062	12.3	10.7	21.3	0.4	1.0	0.60, p<0.05
	28 Oct 2010	6.9	3.0	0.021~0.053	12.5	11.0	37.9	0.8	1.1	0.70, p<0.001
	29 Oct 2010	3.6	4.0	0.025~0.062	11.7	11.0	26.6	0.2	1.0	0.61, p<0.05
	01 Nov 2010	6.0	5.0	0.023~0.033	7.77	10.9	14.3	0.4	1.3	0.77, p<0.01
Class Ib	30 Oct 2010	2.6	1.5	0.031~0.055	9.40	11.1	56.5	0.4	1.1	0.69, p<0.05
	02 Nov 2010	1.8	2.7	0.021~0.024	9.72	10.9	33.0	0.6	1.4	0.77, p<0.05
	08 Nov 2010	1.7	4.5	0.018~0.046	9.14	11.0	18.5	0.2	1.0	0.72, p<0.05
	09 Nov 2010	2.2	3.0	0.014~0.026	7.52	11.4	22.0	0.2	1.2	0.73, p<0.01
Class II	31 Oct 2010	1.1	1.8	0.024~0.030	8.92	11.0	45.1	0.6	1.1	0.74, p<0.05
	11 Nov 2010	1.5	8.4	0.008~0.041	8.76	11.3	9.2	0.4	1.1	0.69, p<0.05
	12 Nov 2010	1.0	4.6	0.016~0.031	6.20	12.0	11.2	0.2	1.2	0.78, p<0.01
	26 Nov 2010	1.0	2.4	0.010~0.024	6.09	10.8	23.5	0.4	1.3	0.49, p<0.05

### 6.4.3 VOCs

Studies have demonstrated that many BVOC species, i.e., isoprene and monoterpenes, and some AVOCs such as toluene could make contributions to the formation of secondary organic aerosol in the atmosphere (e.g., Fu and Kawamura, 2011; Kamens et al., 2011). In this study, it was found that monoterpenes along with O<sub>3</sub>, solar radiation and temperature were positively correlated with GR, while other VOCs species, i.e., isoprene, aromatics and carbonyls including formaldehyde, acetaldehyde and acetone showed poor and negative relationships with GR (Table 6.3). However, the analysis on the correlations of isoprene with total PN concentrations and nucleation mode PN concentrations on NPF event days and non-NPF event days indicated that isoprene had linear correlations with PN and power-law correlations with N<sub>nuc</sub> on both NPF event days ( $R_{PN} = 0.82$  and  $R_{N_{nuc}} = 0.71$ ,  $p < 0.001$ ) and on non-NPF event days ( $R_{PN} = 0.70$  and  $R_{N_{nuc}} = 0.75$ ,  $p < 0.001$ ), suggesting that isoprene might be not a critical parameter for NPF. Instead, the negative correlations of isoprene with FR ( $R = -0.40$ ,  $p < 0.05$ ) and GR ( $R = -0.38$ ,  $p < 0.05$ ) implied that the increase in isoprene might have a negative effect on NPF. Indeed, a recent chamber study found that large isoprene emission could suppress biogenic NPF (Kiendler-Scharr et al., 2009). They claim that NPF rate depends on the concentrations of OH radical which could react with BVOCs to form particles. Due to the strong reactivity of isoprene with OH radicals, OH concentrations are significantly constrained in the presence of isoprene. Moreover, the oxidation products from the reaction between isoprene and OH radical do not contribute to the nucleation process due to their high volatility (Kiendler-Scharr et al., 2009). Therefore, the increased

isoprene emission would inhibit the reaction of non-isoprene VOCs with OH radicals which could produce condensational organic vapors. Previous studies indicate that condensable organics might be important in speeding up the growth of newly formed molecular clusters (e.g., Kerminen et al., 2004). The growth rates of 7–20 nm particles showed positive correlation with monoterpene concentrations and their oxidation rate by O<sub>3</sub> (Yli-Juuti et al., 2011). To investigate the contributions of monoterpenes and their oxidation products to the nucleation mode particle growth, the measured monoterpenes concentration and the estimated oxidation products rate of monoterpenes by O<sub>3</sub>, i.e., [MT\*O<sub>3</sub>] were plotted against the GR of particles during the event hours, i.e., 0800 - 1600 LT in eight NPF events. The linear correlation coefficients are shown in Table 6.3. The results indicated that the GR of 5.5–25 nm particles had good correlations with monoterpene concentrations ( $R = 0.82$ ,  $p < 0.05$ ), and the measurement-based calculated [MT\*O<sub>3</sub>] ( $R = 0.80$ ,  $p < 0.05$ ), suggesting that monoterpenes and their oxidation products could be important in driving the growth of freshly nucleated particles in this mountain area. Indeed, Bonn et al., (2003) found that large organic acids formed from  $\alpha$ -pinene ozonolysis possibly participated in biogenic nucleation and growth.

**Table 6.3** Linear correlations of gaseous pollutants, metrological parameters, CS, BVOCs, AVOCs and carbonyls with the FR, GR and CS for all NPF events observed during the sampling campaign. The data points for gaseous pollutants, metrological parameters and CS are 72; for VOCs and carbonyls are 32. The p-values for all the correlations are below 0.05.

Parameter	Gaseous pollutants				Metrological parameters			CS	BVOCs			AVOC	Carbonyls		
	R (O <sub>3</sub> )	R (SO <sub>2</sub> )	R (NO <sub>x</sub> )	R (CO)	R (Radiation)	R (RH)	R (T)	R (CS)	R (Isoprene)	R (Monoterpenes)	R ([MT*O <sub>3</sub> ])	R (Aromatics)	R (Formaldehyde)	R (Acetaldehyde)	R (Acetone)
<b>FR</b>	-0.54	0.62	-0.22	-0.45	0.54	-0.40	-0.62	-0.56	-0.40	0.57	0.35	-0.42	-0.26	-0.56	-0.10
<b>GR</b>	0.51	-0.33	-0.26	-0.61	0.64	-0.48	0.41	0.51	-0.38	0.82	0.80	-0.50	-0.40	-0.45	-0.25
<b>CS</b>	-0.48	0.62	0.70	0.44	0.62	0.45	-0.56	-----	0.72	0.35	0.20	0.22	-0.10	0.16	0.35

\*Monoterpenes include:  $\alpha$ -Pinene,  $\beta$ -Pinene, Myrcene and Limonene. Aromatics include: Benzene, Toluene, *m*-xylene, *p*-xylene, *o*-xylene, 2-ethyltoluene, 3-ethyltoluene, 4-thyltoluene, 1,3,5-trimethylbenzene, 1,2,4-trimethylbenzene and 1,2,3-trimethylbenz

## 6.5 Conclusions

Particle number size distributions were measured at a suburban site near the mountain summit of Mt.TMS from October to November 2010. The NPF events were observed on 12 out of 35 days at Mt.TMS based on the evolution of particle size distributions and  $N_{\text{nuc}}$  concentrations. Diurnal variations of air pollutants and meteorological parameters suggested that particle nucleation and growth events were associated with cool and dry air from the PRD region caused by the winter monsoon. The mean values of the growth and formation rates of the nucleation mode particles were  $4.2 \text{ nm h}^{-1}$  and  $3.0 \text{ cm}^{-3} \text{ s}^{-1}$ , respectively. Wind speed, solar radiation,  $\text{O}_3$  and  $\text{SO}_2$  concentrations were all on average higher on NPF event days than on non-NPF event days. In contrast, temperature, relative humidity and daytime  $\text{NO}_2$  concentrations were higher on non-NPF event days than on NPF event days. Backward trajectory analyses and wind roses showed that north to northeast winds were prevailing during the NPF events while east winds dominated on the non-NPF event days.

It was found that the formation rate of 5.5nm particle had a power-law dependence on sulfuric acid concentration (with time lag  $\Delta t_{5.5}$ ), with the typical power between 1 and 2, and the contribution of sulfuric acid vapor to the particle growth rate ranged from 9.2% to 52.5% on these NPF event days. The examination of various nucleation parameters revealed that high sulfuric acid production with low condensation sink could be indicators of the occurrence of a potential NPF event. Moreover, based on the correlations of GR with ambient concentrations of BVOCs and their oxidation products, i.e., condensable organics, we found that monoterpenes seemed to be the most important BVOC species related to the GR of particles on the NPF event days.

# **Chapter 7: Observation of nucleation mode particle burst and new particle formation events at an urban site**

## **7.1 Introduction**

In Chapter 6, a number of NPF case studies in rural area demonstrated that NPF is typically favored under the conditions of low pre-existing aerosols, As such, the elevated background concentration of aerosols in polluted locations appears to suppress the NPF. Nevertheless, the NPF was still observed in some polluted environments and most of the studies have related the NPF to the concentration of vapor-phase H<sub>2</sub>SO<sub>4</sub> which is mainly generated by the oxidation of SO<sub>2</sub> by the hydroxyl ( $\cdot$ OH) radical during daytime.

In Hong Kong, about 97% of SO<sub>2</sub> emissions are from local marine sources (50%) and power plants (47%) ([http://www.epd.gov.hk/epd/tc\\_chi/environmentinhk/air/data/emission\\_inve.html](http://www.epd.gov.hk/epd/tc_chi/environmentinhk/air/data/emission_inve.html)). In addition, under the prevailing north/northeast synoptic winds in winter, the regional polluted air enriched with SO<sub>2</sub> from inland Pearl River Delta (PRD) often reaches Hong Kong. Hence, we presented one-month data of particle number (PN) concentrations and particle size distributions (PSD) with a size range of 5.5-350 nm in winter (from December 2010 to January 2011) to investigate the intensity and frequency of nucleation events at an urban site. The characteristics of nucleation mode particle burst and the NPF events were discussed in details, by looking into the simultaneously monitored trace gases (i.e., O<sub>3</sub>, SO<sub>2</sub>, NO-NO<sub>2</sub>-NO<sub>x</sub> and CO) and

meteorological parameters. This sampling site (HH) is situated on the rooftop of a building in the campus of Hong Kong Polytechnic University at Hung Hom. To the northeast of the sampling site, there are two funeral parlors with a distance of ~500 m. To the southwest and southeast is the Victoria Harbour (Figure 7.1).

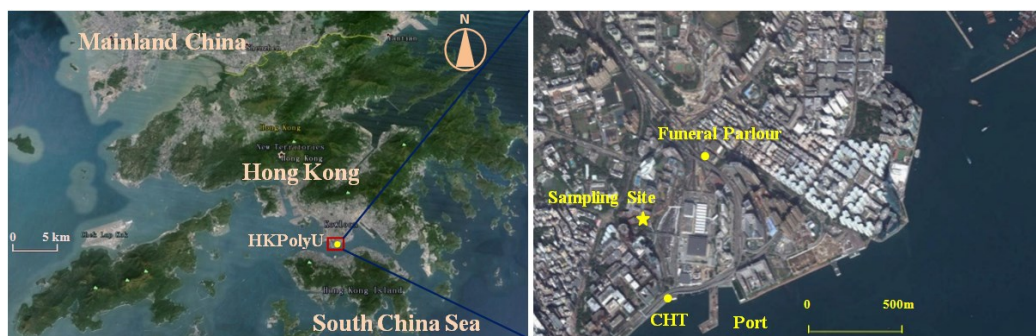


**Figure 7.1** The sampling site and the surrounding environment

## 7.2 General characteristics

### 7.2.1 Particle number concentration

During the sampling period, the daily average PN concentration in the size range of 5.5 - 350 nm was  $2.0 \pm 0.3 \times 10^4 \text{ cm}^{-3}$  (mean  $\pm$  95% confidence interval), falling into the range of reported values ( $0.93 - 6.7 \times 10^4 \text{ cm}^{-3}$ ) in literature for urban sites in Asia, North America and Europe (e.g., Wang et al., 2008; Gao et al., 2009; Westerdahl et al., 2009; Bae et al., 2010; Fernández-Camacho et al., 2010; Cheung et al., 2011). The average number concentrations of nucleation-, Aitken- and accumulation mode particles (namely  $N_{\text{nuc}}$ ,  $N_{\text{Ait}}$  and  $N_{\text{acc}}$ ) were  $0.25 \pm 0.04 \times 10^4$ ,  $1.6 \pm 0.2 \times 10^4$  and  $0.15 \pm 0.01 \times 10^4 \text{ cm}^{-3}$ , respectively. By comparison with studies conducted in other coastal urban areas, the measured UFP number concentration ( $N_{\text{UFP}} = N_{\text{nuc}} + N_{\text{Ait}}$ ) in this study was  $1.85 \pm 0.21 \times 10^4 \text{ cm}^{-3}$ , lower than that in Huelva, Southwest Spain ( $2.2 \times 10^4 \text{ cm}^{-3}$ ; Fernández-Camacho et al., 2010) and in the

Yangtze River Delta, China ( $2.9 \times 10^4 \text{ cm}^{-3}$ ; Gao et al., 2009), but much higher than that in Brisbane, Australia ( $0.93 \times 10^4 \text{ cm}^{-3}$ ; Cheung et al., 2011). And based on the measurement of AUFPs by DS detectors at this sampling period, we found the AUFPs number concentrations were elevated up to  $1.0 \times 10^4 \text{ cm}^{-3}$  during several sampling sessions, i.e., 25-27 December 2010, 27-29 December 2010, 29-31 December 2010, 03-05 January 2011 and 13-15 January 2011, at which the nucleation events were frequently observed (see Section 7.2.3).

### **7.2.2 Diurnal variations**

Figure 7.2 shows the average diurnal variations of PN concentrations in the three modes ( $N_{\text{nuc}}$ ,  $N_{\text{Ait}}$  and  $N_{\text{acc}}$ ), meteorological parameters (solar radiation, wind, RH and Temperature) and gaseous pollutants ( $\text{SO}_2$ ,  $\text{NO}_x$ , CO and  $\text{O}_3$ ) for the sampling period.  $N_{\text{nuc}}$  presented a low peak at  $\sim 08:00$ , a high peak at 10:00-14:00 and a broad peak at 18:00 - 01:00 on next day. Coincident with traffic rush hours, the early morning  $N_{\text{nuc}}$  peak was likely caused by the condensation and nucleation of chemical species e.g., inorganic and organic vapors emitted from hot engines after rapid cooling and dilution (Kittelson, 1998, 2006; Charron and Harrison, 2003; Yu, 2010). This was consistent with the  $N_{\text{Ait}}$  peak observed at the same hour.

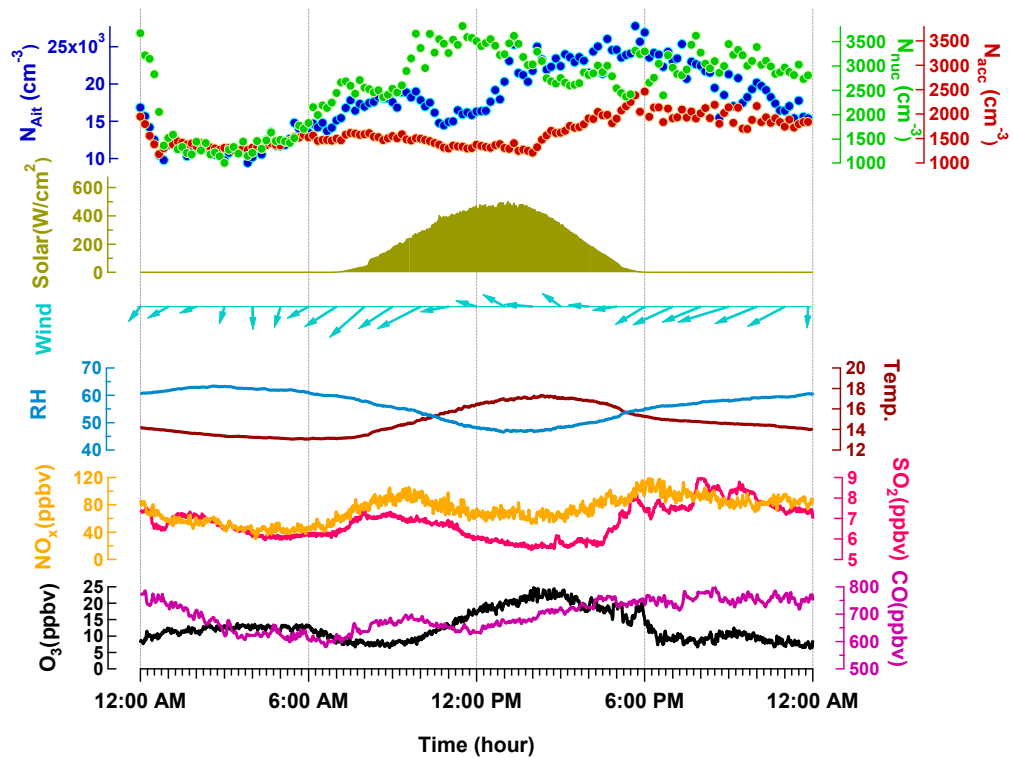


**Figure 7.2** Average diurnal variations of (a) nucleation mode (green), Aitken mode (blue) and accumulation mode (red) particle number concentrations, (b) solar radiation, (c) wind direction/speed, (d) temperature and RH, (e) NO<sub>x</sub> and SO<sub>2</sub> mixing ratios and (f) O<sub>3</sub> and CO mixing ratios (from top to bottom).

Commencing at 10:00, the solar radiation intensity and temperature increased rapidly, along with the decrease in RH (i.e., conditions typically attributed to clear days), and the wind speed reduced close to zero (Figure 7.2). The  $N_{\text{nuc}}$  increased from  $2.0 \times 10^3 \text{ cm}^{-3}$  to  $3.5 \times 10^3 \text{ cm}^{-3}$  at noon. Meanwhile, the secondary pollutant O<sub>3</sub> also showed an increase whereas the  $N_{\text{Ait}}$ ,  $N_{\text{acc}}$ , SO<sub>2</sub>, NO<sub>x</sub> and CO levels decreased from 10:00 to 12:00. The nucleation and Aitken modes shifted towards each other during the afternoon, until 17:00, as a result of the intensive growth of the nucleation mode particles. The peak of Aitken mode particles correlated well with the peak of nucleation mode particles, with a time delay of about three hours, suggesting the growth of nucleation mode

particles into Aitken mode particles. This is typical new particle formation (NPF) process.

It was found that  $N_{\text{nuc}}$  remained relatively high values from 18:00 to 01:00 on next day, while  $N_{\text{Ait}}$  and  $N_{\text{acc}}$  decreased during this period. As shown in Figure 7.2, the increase of  $N_{\text{Ait}}$  with one peak at 08:00 and another peak at 18:00 was coincident with the typical traffic rush hours, suggesting the dominant contribution of traffic emissions to  $N_{\text{Ait}}$ . The decrease of  $N_{\text{Ait}}$  during 18:00 - 01:00 on next day indicated the contribution of traffic to PN weakened in this period, implying additional  $N_{\text{nuc}}$  source(s) responsible for the high values in the evening. Meanwhile, the levels of  $\text{SO}_2$ ,  $\text{NO}_x$  and CO also stayed high during this period. The high concentrations of  $N_{\text{nuc}}$  and gaseous pollutants might be attributed to the nucleation mode particle burst events observed in late evening and at midnight during the sampling period. Detailed discussion about the burst events is given in Section 7.3.

### **7.2.3 Nucleation mode particles burst and NPF events**

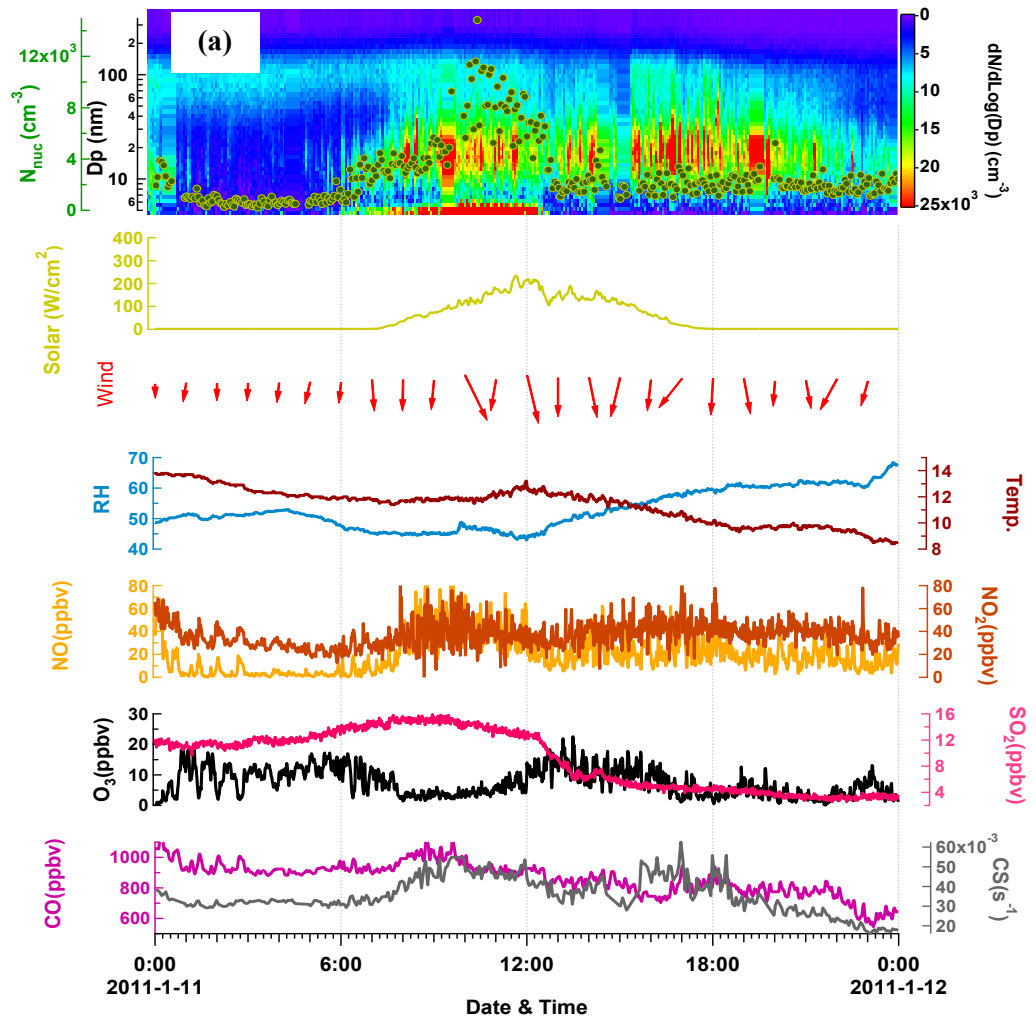
The analysis on diurnal variations of PN concentrations, meteorological parameters and gaseous pollutants showed the increase in  $N_{\text{nuc}}$  was associated with primary emission and/or secondary formation. According to the definition of nucleation events in chapter 3, four days were classified as nucleation mode particle burst events (i.e., 07, 10, 11 and 14 January, 2011) and 7 days as NPF events for the sampling period (see Table 7.1). Using the classification scheme (Class I and II) developed by Dal Maso et al., (2005), the 7 NPF events were further categorized into Class I (3 days, i.e., 26, 30 and 31 December, 2010) and Class II (4 days, i.e., 23 December 2010, 01, 15 and

17 January, 2011). Class I events are defined as those in which both the growth rate  $GR_{5.5-10\text{nm}}$  and formation rate  $J_{5.5}$  can be determined with a good confidence level. A typical Class I event demonstrates clear and strong particle formation events with little or no pre-existing particles obscuring the observation of the newly formed particles. Class II events are defined as those in which the banana shape is still observable with a clear growth in the size range of 10-25 nm, however, it was not possible to obtain formation rate  $J_{5.5}$ , due to strong fluctuations in the particle concentration in the size range of 5.5-10 nm. While  $GR_{5.5-10\text{nm}}$  still can be determined by  $GR_{10-25\text{nm}}$ . In principle, the particle formation takes place during the daytime followed by an almost linear particle diameter growth (e.g., Mäkelä et al., 2000). The growth rate  $GR_{5.5-10\text{nm}}$  was regarded as equal to the  $GR_{10-25\text{nm}}$  during the NPF event.

### **7.3 Nucleation mode particle burst events**

Figure 7.3a shows a burst event observed on 11 January 2011. This event occurred between 06:00 and 13:00 when the solar radiation intensity and temperature were very low (max:  $\sim 200\text{ W/cm}^2$  and  $14^\circ\text{C}$ , respectively), indicating that photochemical reactions might not be the driving force of nucleation mode particle formation during this event. Instead, it is favorable for the condensation and nucleation of chemical vapor directly emitted from combustion sources in cold and dry weather. Elevated  $N_{\text{nuc}}$  was observed without subsequent growth with a constant GMD ( $24 \pm 3\text{nm}$ ), likely due to the relatively high CS during the event, causing the condensable vapors scavenged into the pre-existing large particles. It was also found that northerly wind prevailed with elevated wind speed during the burst event, suggesting that vehicle emissions and/or incineration from funeral parlour in northeast

direction might contribute to the burst (Figure 7.1). Further investigation showed that  $N_{\text{nuc}}$ , primary gaseous pollutants, i.e.,  $\text{SO}_2$ ,  $\text{NO}_x$  and CO and CS reached the daily maximum ( $\sim 0.92 \times 10^4 \text{ cm}^{-3}$ ,  $\sim 15 \text{ ppbv}$ ,  $\sim 160 \text{ ppbv}$ ,  $1023 \text{ ppbv}$  and  $0.06 \text{ s}^{-1}$ , respectively), whereas the secondary pollutant  $\text{O}_3$  level was the lowest during the burst event. This polluted plume with unusual high levels of primary pollutants was unlikely generated from vehicle emissions as the traffic flow was similar everyday and such phenomenon was not regularly observed in the sampling period. Hence, incineration from funeral parlour was suspected. In Hong Kong, funeral parlour is a place for memorial of dead, in which paper money, paper furniture and house with wood/bamboo frame, joss incense and candles are burnt in simple and crude incinerators. As observed, this kind of activity is not regular but will release large amount of gaseous-phase and particulate-phase pollutants to the air whenever occurred. Indeed, furnaces for joss paper and incense burning often caused incomplete combustion due to poor air supply, resulting in remarkable emissions of pollutants such as CO,  $\text{NO}_x$  and  $\text{SO}_2$  (Yang et al., 2001; Jetter et al., 2002; Lee and Wang, 2004, 2006), and particles with diameter between  $<10$  and  $300 \text{ nm}$  (Fang et al., 2002, 2003; Choosong et al., 2010; Li et al., 2010b). In this study,  $N_{\text{nuc}}$  had moderate correlations with  $\text{NO}_x$  ( $r = 0.69$ ,  $p < 0.01$ ), CO ( $r = 0.68$ ,  $p < 0.01$ ) and  $\text{SO}_2$  ( $r = 0.58$ ,  $p < 0.01$ ), suggesting that funeral incineration was likely responsible for this event.



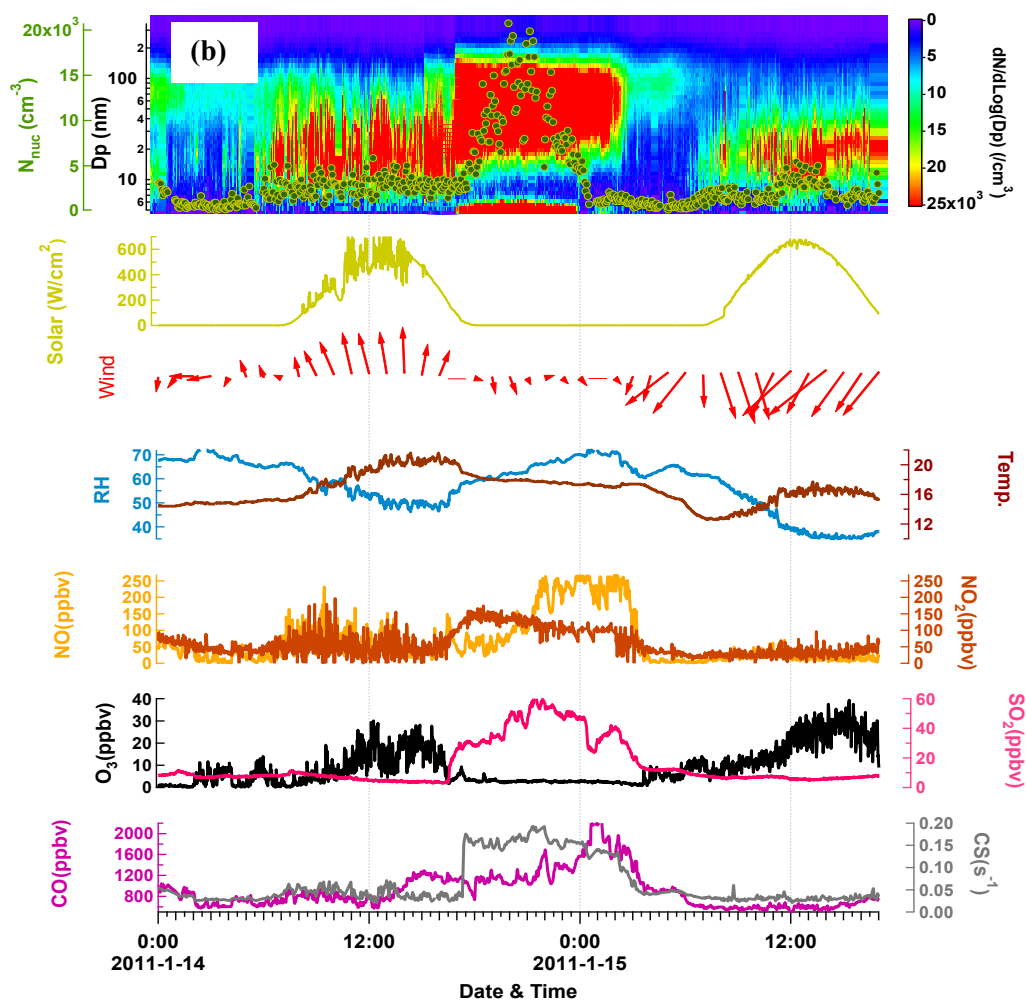


**Figure 7.3** The nucleation mode particle burst events (a) on 11 January 2011 and (b) on 14/15 January 2011. From top to bottom: Contour plot of particle size distribution, diurnal variations of solar radiation, wind direction/speed, temperature and RH, NO and NO<sub>2</sub> mixing ratios, O<sub>3</sub> and SO<sub>2</sub> mixing ratios and CO mixing ratio and condensation sink (CS).

Figure 7.3b presents another burst event from 17:00 on 14 January 2011 to 03:00 on 15 January 2011. Since this burst event occurred in the evening, there was no solar radiation along with decreased temperature and increased RH, and wind became calm with northern direction. Under such weather condition, the dispersion of air pollutants was expected to be poor. Indeed, apart from the sharp increase in  $N_{nuc}$ ,  $N_{Ait}$ ,  $N_{acc}$ , SO<sub>2</sub>, NO<sub>x</sub> and CO levels also

showed tremendous increase during the event. The  $N_{\text{nuc}}$  increased rapidly from  $0.46 \times 10^4 \text{ cm}^{-3}$  to the maximum value of  $\sim 1.9 \times 10^4 \text{ cm}^{-3}$ , while the  $\text{SO}_2$ ,  $\text{NO}_x$  and CO mixing ratios lifted from  $\sim 30$  to  $\sim 56$  ppbv,  $\sim 180$  to  $\sim 330$  ppbv, and  $\sim 1000$  to  $\sim 2000$  ppbv, respectively. Similar to the reasons in the burst event of 11 January 2011, the extremely high levels of primary gaseous pollutants measured in this event indicated that the polluted air, which lasted for 10 hours, was not from vehicle emissions. Throughout the entire event, a bimodal size distribution with one peak at 5.5-7 nm and another at 50-75 nm was observed, suggesting that the nucleation mode particles had the same source as Aitken- and accumulation mode particles. In addition, the nucleation-mode particles exhibited no subsequent growth into Aitken and accumulation modes with a constant GMD value of  $36 \pm 4$  nm, and survived for several hours in the presence of a strong condensation sink ( $0.05 \text{ s}^{-1}$  to  $0.19 \text{ s}^{-1}$ ) (see Figure 7.3b). The reason was probably that the production rate of nucleation-mode particles was higher than the loss rate caused by coagulation and condensation processes, and high CS caused condensable vapor to be scavenged into pre-existing large particles. Furthermore, in this event, the  $N_{\text{nuc}}$ ,  $N_{\text{Ait}}$  and  $N_{\text{acc}}$  all correlated well with  $\text{SO}_2$  ( $r = 0.74$ ,  $r = 0.85$  and  $r = 0.76$ , respectively,  $p < 0.001$ ) and  $\text{NO}_2$  ( $r = 0.82$ ,  $r = 0.88$  and  $r = 0.92$ , respectively,  $p < 0.001$ ), suggesting that  $N_{\text{nuc}}$  was related to primary emission. Since the atmospheric dispersion was poor when the event occurred, we speculated that the source(s) should be near the sampling site. Species-to-species ratio analysis found that the measured  $\text{SO}_2/\text{NO}_2$  and  $\text{CO}/\text{NO}_2$  ratios in the event were  $0.3 \pm 0.1$  ppbv/ppbv and  $8.6 \pm 1.0$  ppbv/ppbv, respectively, different from the ratios of traffic emissions ( $\text{SO}_2/\text{NO}_2$ : 0.3 - 0.5 ppbv/ppbv and  $\text{CO}/\text{NO}_2$ : 20 - 30

ppbv/ppbv) in Hong Kong (data from [www.epd.gov.hk](http://www.epd.gov.hk)), indicating that this event was caused by non-vehicle combustion sources using higher sulfur-content fuel. Site visits showed that incineration at the funeral parlor in the northeast direction and the marine vessel emissions at Victoria Harbour in south direction were the two major non-vehicle combustion sources around the sampling site. As the wind direction was northerly during the event, incineration from the funeral parlour was the top suspects. Indeed, the CO levels ( $\sim 1000$ - $2000$  ppbv) in this event were comparable to that of candles ( $\sim 800$ - $2000$  ppbv) and incense burning ( $\sim 800$ - $38000$  ppbv) (Lee and Wang, 2004, 2006). In addition, in this event the CO/NO ratio ( $11 \pm 3$  ppbv/ppbv) was consistent with that ( $\sim 10$  ppbv/ppbv) of wooden pellets combustion (Musialik-Piotrowska et al., 2010), and the SO<sub>2</sub>/NO<sub>2</sub> ratios ( $0.3 \pm 0.1$  ppbv/ppbv) was similar with the ratios in biofuel combustion (e.g., wood: 0.2-0.4 ppbv/ppbv) (Gadi et al., 2003). Furthermore, the PSD observed in this event was comparable to that generated from candle and incense burning, namely, the particles ranged between 2.5-300 nm with one peak in the nucleation-mode ( $\sim 2.5$ - $9$  nm), one peak in the Aitken-mode ( $\sim 10$ - $40$  nm) and one peak in the accumulation-mode ( $\sim 100$ - $300$  nm) (Karasev et al., 2004; Lipsky et al., 2006; Wright et al., 2007; Géhin et al., 2008; Chuang et al., 2011; Manoukian et al., 2013). However, firm conclusions could only be drawn after the source profiles of funeral incineration in Hong Kong are obtained.

#### **7.4 NPF events**

Overall, among the 7 NPF events identified in this study, the growth rate  $GR_{5.5-10\text{nm}}$  of the Class I events ranged from 5.6 to 8.3 nm h<sup>-1</sup> with a mean

value of  $6.7 \text{ nm h}^{-1}$ , while the growth rate of the Class II events was between  $3.7$  and  $4.6 \text{ nm h}^{-1}$  with a mean level of  $4.1 \text{ nm h}^{-1}$  (Table 7.1).

**Table 7.1** The event date, growth rate ( $GR_{5.5-10\text{nm}}$ ), vapor concentration of sulfuric acid proxy ( $C_{\text{SA}}$ ) in each Class I and II NPF event, and  $5.5 \text{ nm}$  particle formation rate ( $J_{5.5}$ ), exponent ( $n$ ), the correlation coefficient of  $\ln(C_{\text{SA}})$  versus  $\ln(J_{5.5})$  at 07:00-10:00 and fractional contribution of SA vapor to particle growth (FC) in each Class I NPF event.

Date	$GR_{5.5-10\text{nm}}$ ( $\text{nm h}^{-1}$ )	$C_{\text{SA}}$ ( $\text{cm}^{-3}$ )	$J_{5.5}$ ( $\text{cm}^{-3} \text{ s}^{-1}$ )	$n$	R ( $\ln C_{\text{SA}} \sim \ln J_{5.5}$ )	FC (%)
<b>Class I</b>						
<b>26 Dec 2010</b>	8.3	$2.16 \times 10^7$	$2.3 \pm 0.9$	2.2	0.74	28.6
<b>30 Dec 2010</b>	5.6	$8.89 \times 10^6$	$2.2 \pm 0.7$	2.9	0.64	17.5
<b>31 Dec 2010</b>	6.3	$1.13 \times 10^7$	$1.2 \pm 0.4$	3.3	0.83	19.7
<b>Class II</b>						
<b>23 Dec 2010</b>	3.9	$1.36 \times 10^7$	-	-	-	38.4
<b>01 Jan 2011</b>	4.2	$1.62 \times 10^7$	-	-	-	42.4
<b>15 Jan 2011</b>	4.6	$1.20 \times 10^7$	-	-	-	28.7
<b>17 Jan 2011</b>	3.7	$7.69 \times 10^6$	-	-	-	22.9

As an example, we took a Class I NPF event to investigate the characteristics of NPF and growth. This NPF event was observed on 26 December, 2010, the day immediately after  $0.5 \text{ mm}$  rainfall was recorded on 25 December at the site. In the morning, the solar radiation intensity and temperature increased rapidly with decreased RH, and the wind speed increased from calm to northerly/northeasterly winds, following the break-up of the nocturnal inversion layer (Figure 7.4). Furthermore, the CS prior to the beginning of this NPF event was low. The nucleation mode appeared in the measurement range at  $\sim 10:00$  and the  $N_{\text{nuc}}$  increased substantially from  $\sim 1.9 \times 10^3 \text{ cm}^{-3}$  at 10:30 to  $9.5 \times 10^3 \text{ cm}^{-3}$  at 12:00 (Figure 7.4). In the afternoon,

nucleation and Aitken modes shifted towards each other until 13:00, as a result of the intensive growth of the nucleation-mode particles. To further investigate the NPF event, the correlations of  $N_{\text{nuc}}$  with primary pollutants i.e.,  $\text{SO}_2$ ,  $\text{NO}$ ,  $\text{CO}$  and secondary pollutants i.e.,  $[\text{NO}_2+\text{O}_3]$  were evaluated.  $N_{\text{nuc}}$  poorly correlated with  $\text{NO}$  ( $r = 0.12$ ,  $p < 0.01$ ) and  $\text{CO}$  ( $r = -0.25$ ,  $p < 0.01$ ) but had moderate correlation with  $\text{SO}_2$  ( $r = -0.71$ ,  $p < 0.001$ ) and  $[\text{NO}_2+\text{O}_3]$  ( $r = 0.67$ ,  $p < 0.001$ ), suggesting that photochemical reactions involving vapor-phase  $\text{H}_2\text{SO}_4$  and/or volatile organic compounds (VOCs) were responsible for this NPF event.

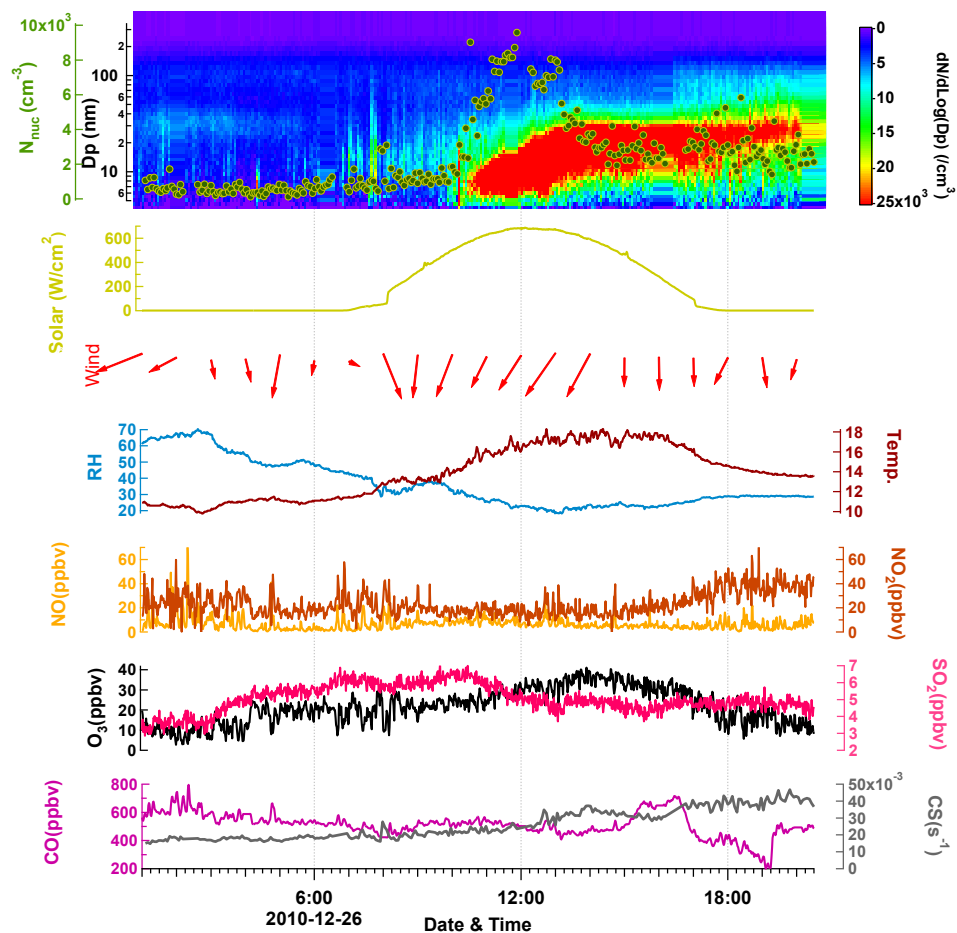


**Figure 7.4** The NPF event on 26 December 2010. From top to bottom: Contour plot of particle size distribution, diurnal variations of solar radiation, wind direction/speed,

temperature and RH, NO and NO<sub>2</sub> mixing ratios, O<sub>3</sub> and SO<sub>2</sub> mixing ratios and CO mixing ratio and condensation sink (CS) .

We then investigated the relationship between 5.5 nm particle formation rate ( $J_{5.5}$ ) and H<sub>2</sub>SO<sub>4</sub> vapor concentration ( $C_{sa}$ ) in the three Class I NPF events. Good correlations between  $J_{5.5}$  and H<sub>2</sub>SO<sub>4</sub> vapor concentration ( $r = 0.64 - 0.83$ ) were found (Table 7.1), which showed the exponents in the correlation of  $J_{5.5}$  with H<sub>2</sub>SO<sub>4</sub> concentrations between 2 and 4 (mean value = 2.8, Figure 7.5). The mean exponent was slightly higher than the values (i.e., 1 - 2) obtained in some previous studies (e.g., Weber et al., 1999; Kulmala et al., 2006; Sihto et al., 2006), but similar to that (i.e., >2) reported by Wang et al., (2011), perhaps suggesting different formation mechanisms. In fact, the relationship between particle formation rate and H<sub>2</sub>SO<sub>4</sub> concentration with the exponent of 1 - 2 was well explained by the activation and kinetic theory. For the NPF events with a larger exponent value, a thermodynamic process was developed to explain the NPF mechanism (e.g., Kuang et al., 2008; Wang et al., 2011). In this study, the larger exponent between particle formation rate and H<sub>2</sub>SO<sub>4</sub> concentration implied that apart from H<sub>2</sub>SO<sub>4</sub> vapor, other chemical species such as low-volatile organic vapors might be also involved in the initial start of the nucleation process (McGraw and Zhang, 2008). In addition, the contribution of SA to particle growth was about 28.3% ±9.3% at this urban site (Table 7.1). Meanwhile, at Tai Mo Shan (TMS) the fraction contribution (FC) of sulfuric acid to GR in all NPF events ranged from 9.2% to 52.5% with an average of 26.6%. The FC of sulfuric acid to GR at these two sites were both comparable with those reported in previous studies (4% - 31%) (Boy et al., 2005). Boy et al., (2003) estimated the lower range of a growth rate

fraction for SA was 8.8%, indicating that the concentration of SA in Hong Kong area wherever in rural or urban areas seems always to be high for particle growth need.

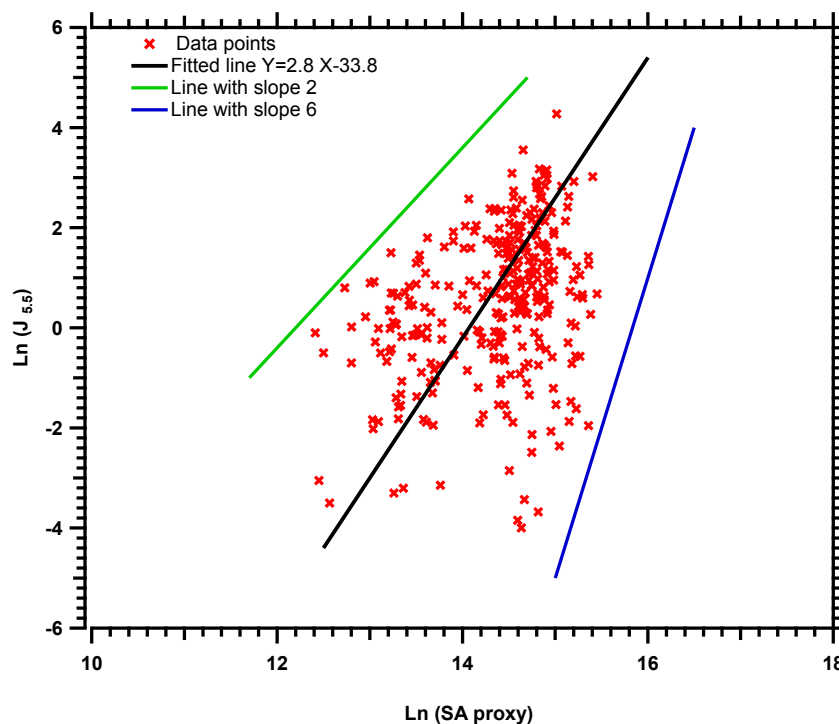


**Figure 7.5** Logarithm of formation rate  $J_{5.5}$  versus logarithm of sulfuric acid proxy ( $C_{SA}$ , 4-minute averages) during Class I NPF events at 07:00~10:00.  $C_{SA}$  are delayed by fitted time lags ranging from 0 to 2 hours. The two red lines represent the exponent values of 2 and 4 for the correlation of  $J_{5.5}$  and sulfuric acid proxy concentrations.

## 7.5 Comparison among burst events, NPF events and non-nucleation events

Figure 7.6 shows the average temporal variations of  $N_{nuc}$ , meteorological parameters and trace gas mixing ratios in (a) nucleation mode particle burst events (red lines), (b) NPF events (blue lines) and (c) non-nucleation events (green lines). It is obvious that the  $N_{nuc}$  in the non-nucleation events had no

distinct peaks, whereas the  $N_{\text{nuc}}$  in the burst events showed bimodal pattern with one peak in the morning and another at night, and the  $N_{\text{nuc}}$  in NPF events presented one peak during midday. The peaks shown at different hours of a day indicated the sources of the nucleation mode particles were different. In addition, the Pearson correlation coefficients were calculated between hourly nucleation mode particle number concentration and ambient pollutants as well as meteorological parameters (see Table 7.2).

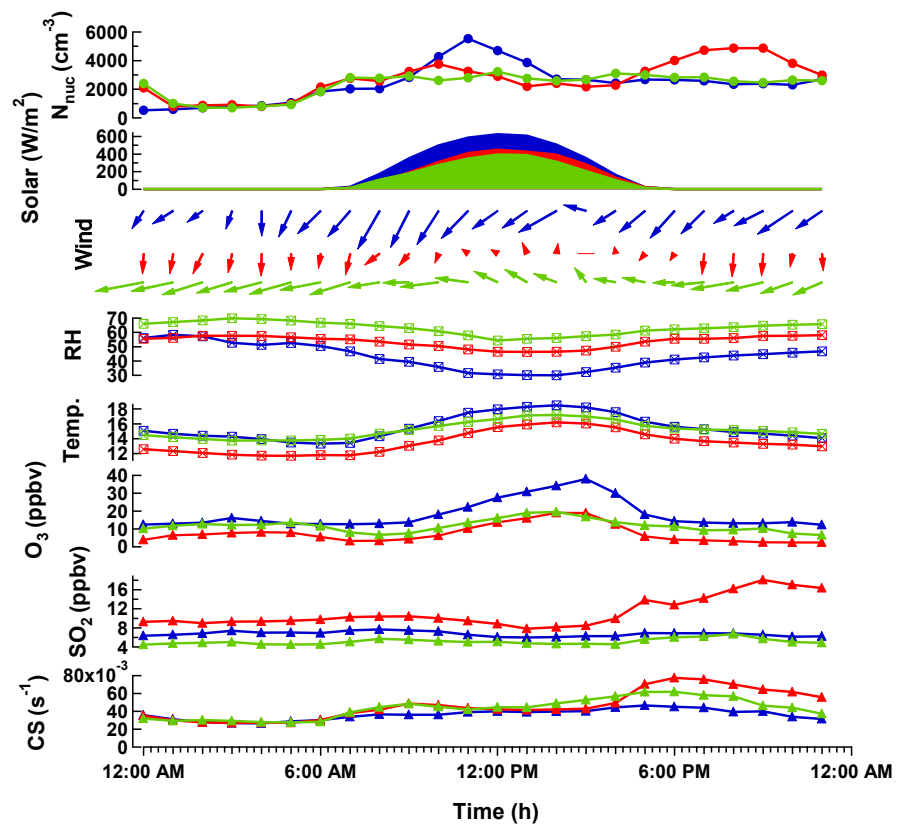


**Figure 7.6** Average diurnal variations of nucleation mode particle number concentration, solar radiation, wind direction/speed, RH, temperature,  $\text{O}_3$  mixing ratio,  $\text{SO}_2$  mixing ratio and condensation sink (from top to bottom) during nucleation mode particle burst events (red lines), NPF events (blue lines) and non-nucleation events (green lines).

**Table 7.2** Pearson correlation coefficients ( $r$ ) between hourly averaged nucleation mode particle number concentrations and gaseous concentrations as well as meteorological parameters during nucleation mode particle burst events, NPF events and non-nucleation events. The coefficients higher than 0.7 and the positive correlation coefficients of  $N_{\text{nuc}}$  with  $O_3$  and wind speed are in bold. All  $p$ - values are smaller than 0.01.

Date	$O_3$	CO	$SO_2$	NOx	SR	Temp	RH	CS	Wind speed	$C_{SA}$
<b>nucleation mode</b>										
<b>particle burst events</b>	-0.35	<b>0.78</b>	<b>0.71</b>	<b>0.89</b>	0.05	0.30	-0.06	<b>0.88</b>	-0.09	0.06
<b>NPF events</b>	<b>0.47</b>	0.07	-0.26	0.33	<b>0.79</b>	0.66	<b>-0.86</b>	0.56	<b>0.55</b>	<b>0.79</b>
<b>non-nucleation events</b>	-0.06	0.44	0.37	<b>0.79</b>	0.44	0.69	-0.73	<b>0.77</b>	-0.57	0.44

By comparison, the average solar radiation intensity and temperature in NPF events were higher, but the RH was lower than that in burst events and non-nucleation events, suggesting that dry and sunny weather was favorable to the NPF. The good negative correlation between the  $N_{\text{nuc}}$  and RH ( $r = -0.86$ ,  $p < 0.001$ ) can be explained in terms of the lower ambient RH being an important factor in the formation of new particles. In contrast, the burst events were mainly accompanied with higher RH and lower temperature than the NPF events, implying that cold and humid weather would enhance the nucleation of gaseous pollutants with low vapor pressure from combustion sources, leading to the increase of  $N_{\text{nuc}}$ . In addition, the wind directions and speeds in the three events were different (Figure 7.6). The wind speed was the lowest in burst events. Low wind speed is often associated with stagnant atmospheric condition which is favorable for the accumulation of air pollutants i.e., nucleation mode particles near the emission sources. As such, it was not surprising that elevated primary  $N_{\text{nuc}}$  levels were observed in burst

events. In contrast, the initial start of NPF events often occurs when the wind speed is high and the atmospheric dispersion is excellent. This is because excellent dispersion associated with high wind speeds reduces the pre-existing larger particles, favoring the NPF process. We also found that in the NPF events, the peak  $N_{\text{nuc}}$  level was related to northeasterly winds, suggesting air mass from the northeast was related to the NPF events.

Apart from the impact of meteorology, air pollutants were related to the events as well. Good correlations of  $N_{\text{nuc}}$  were found with ambient trace gaseous pollutants i.e., CO, SO<sub>2</sub> and NO<sub>x</sub> ( $r = 0.78$ ,  $r = 0.71$  and  $r = 0.89$ ,  $p < 0.001$ , respectively) during nucleation mode particle burst events. The hourly average O<sub>3</sub> mixing ratio was generally higher in NPF events than the corresponding value in non-nucleation and burst events, and the highest correlation was observed between the  $N_{\text{nuc}}$  and O<sub>3</sub> ( $r = 0.47$ ,  $p < 0.01$ ) as well as solar radiation ( $r = 0.79$ ,  $p < 0.01$ ), suggesting the photochemical secondary formation of nucleation mode particles. On the other hand, the SO<sub>2</sub> levels were the highest in the burst events and correlated well with the  $N_{\text{nuc}}$  concentrations ( $r = 0.72$ ,  $p < 0.001$ ). Compared to the burst events,  $N_{\text{nuc}}$  in the NPF events had weak negative correlation with SO<sub>2</sub> ( $r = -0.26$ ,  $p < 0.01$ ) but good positive correlation with H<sub>2</sub>SO<sub>4</sub> proxy ( $r = 0.79$ ,  $p < 0.001$ ). The phenomena suggested that the formation of nucleation mode particles in NPF events was directly related to the concentration of vapor-phase H<sub>2</sub>SO<sub>4</sub> which is mainly generated by the oxidation of SO<sub>2</sub>.

Additionally, the CS values were low in the NPF events, consistent with the principle that low CS is favorable to the secondary NPF. In contrast, the CS values in the burst events were the highest, contradictory to the principle that

high CS prevents the nucleation process as discussed in NPF events. The elevated CS observed in the burst events indicated that nucleation could still occur despite high CS values. This was probably due to the fact that nucleation and condensation of the extremely high concentrations of gaseous precursors (e.g., H<sub>2</sub>SO<sub>4</sub> and organics) directly emitted from the combustion sources could overcome the nucleation barrier imposed by the high pre-existing particle concentration (Seinfeld and Pandis, 2006).

## **7.6 Summary and conclusions**

In a 30-day intensive sampling campaign conducted in winter at an urban site in Hong Kong, 4 nucleation mode particle burst events and 7 NPF events were identified. The diurnal variation analysis showed that  $N_{\text{nuc}}$  was influenced by primary emissions in early morning and at night, while the elevated  $N_{\text{nuc}}$  at noon was attributed to the NPF via photochemical reactions. The  $N_{\text{nuc}}$  in the burst events had close correlation with NO<sub>x</sub> and SO<sub>2</sub>, implying that combustion sources with high sulfur-containing fuel such as joss paper, incense, candle and wood burning in funeral parlor, were the dominant emissions of the  $N_{\text{nuc}}$  at the site. During the burst events, weather conditions with low wind, high RH and low temperature/solar radiation were often observed. The calm wind was not beneficial to the dispersion of nucleation mode particles directly emitted from the combustion sources, whereas the high RH and low temperature enhanced the nucleation and condensation of the gaseous precursors emitted from the sources. On the other hand,  $N_{\text{nuc}}$  in the NPF events showed no correlation with SO<sub>2</sub>, CO and NO<sub>x</sub>, but good correlation with H<sub>2</sub>SO<sub>4</sub> vapor concentrations, suggesting the potential participation of photochemically formed H<sub>2</sub>SO<sub>4</sub> in the nucleation processes.

Weather conditions with strong solar radiation, high temperature, low RH, and low condensation sink were found to be perfect for the NPF in the atmosphere of urban Hong Kong.

## **Chapter 8: Conclusions and suggestions for future research**

### **8.1 Conclusions**

In order to obtain accurate number concentration of acidic ultrafine particles in the atmosphere of Hong Kong, new technologies had been developed in this study. Firstly, two new types of iron nanofilm detectors coated by magnetron sputtering (MS) were developed with more stable performance. Iron nanofilm coated using MS method had a smoother surface than using thermal vacuum evaporation (VE). A 5 nm titanium (Ti) layer was coated between the substrate and iron nanofilm to increase the adhesion of iron nanofilm on the substrate. The iron nanofilm (i.e., Fe-Ti-MS and Fe-MS) coated by MS showed stronger adhesion to silicon substrate than coated by VE method. The surfaces of Fe-Ti-MS and Fe-MS detectors remained stable under severe weather condition (85% RH and 35°C), while the surfaces of Fe-Ti-VE and Fe-VE detectors started to corrode after 2-week exposure. Fe-Ti-MS and Fe-MS detectors did not have significant changes even after the 3-month exposure period under the condition of 90% RH and 20°C. In addition, ambient corrosive gases (i.e., SO<sub>2</sub> and NO<sub>x</sub>) were found to have negligible effect on the surface roughness of the iron nanofilm detectors during the sampling periods.

After iron nanofilm detectors with stable performance were made, the relationship between reaction spots on the detector and the size of generated

acidic droplets and acid-coated particles was established. For acidic droplets, larger droplet with the same acidity as smaller droplet had a larger horizontal distance (width) of the reaction spot, whereas vertical distance (height) had an obvious increase with the increase of the droplet size and acidity. However, no good linear correlation between size of droplet and reaction spot was obtained. The main reason was that even after the size classifier, the monodisperse droplets can still easily coagulate together, inducing polydisperse droplets deposited on the detector. For acid-coated particles, the diameter of reaction spots on the detectors was about three times the originally generated particle size, and the height of reaction spots was about one third of the original particle size, showing good linear correlations.

Two collection systems, i.e., electrostatic precipitator (EPS) and diffusion sampler (DS) were modified or developed to collect iron nanofilm detector samples. The deposition efficiencies of ESP and DS were both calibrated and determined in laboratory experiments. For ESP, the deposition efficiency of ESP at 5000 voltage with a flow rate of  $0.3 \text{ L min}^{-1}$  was determined to be  $86 \pm 11\%$  for 102 nm PSL,  $80 \pm 16\%$  for 46 nm PSL, and  $74 \pm 19\%$  for 30 nm PSL standards, respectively. The smaller the particle is, the lower its collection efficiency in ESP. For DS, The stepwise deposition efficiency of particles in each size decreased with the increase in transport distance from the inlet and also decreased with the increase in sampling flow rate. The stepwise diffusive deposition efficiency of particles at the different detector locations in DS was calibrated respectively by the semi-empirical equations which were obtained from the combination of theoretical calculation and experimental data.

After calibration, field sampling campaigns were conducted at Mt. Tai Mo Shan (the rural site) and Hung Hom (the urban site) to collect samples onto iron nanofilm detectors by both EPS and DS. After exposure, the iron nanofilm detector surface was scanned topographically by an atomic force microscope (AFM) to view and enumerate the reaction sites. Quantitative approach was established for the calculation of number concentration and size distribution of ambient acidic and total aerosols based on the AFM results. Then the total UFPs concentrations (acidic + non-acidic) were quantified from the detector samples exposed in both EPS and DS, and these values were validated by the total UFPs concentrations measured by the SMPS+CPC. As such, the AUFPs quantified from the detector samples exposed in ESP and DS respectively was validated in field measurements. The calculated results showed good agreements with total number concentrations and average geometric mean diameter of UFPs measured by SMPS+CPC system ( $p > 0.05$ ). Therefore, it is reasonable to assume that the number concentration and size distribution of AUFPs estimated by ESP and DS methods were reliable.

During the field measurements, the abundance of acidic ultrafine particles was determined at two sites. We found remarkable differences in the AUFPs number levels between the rural and the urban sites. At the urban site, the level of AUFPs was almost 5-7 times that at the rural site. And AUFPs counted for more fractions of PN concentrations (32.5 - 42.9%) in urban area than that (21.1 - 30.1%) in rural area, indicating the primary emissions had an important contribution to the increased AUFPs concentration in urban area. The mean UFPs and AUFPs number concentrations at these two sites were all higher in

NPF events than those in non-NPF events, indicating the new particle formation played an important role in the increased AUFPs concentration.

Finally, to investigate the sources and potential formation mechanisms of ultrafine particles during the field measurements at the rural and urban sites, particle number size distributions were measured along with meteorological parameters and gaseous pollutants. The NPF events were observed on 12 out of 35 days at Mt.TMS and 7 out of 30 days at HH during the intensive sampling sessions. At the Mt. TMS site, the diurnal variation of nucleation mode particle number concentration ( $N_{\text{nuc}}$ ) showed a significant contribution of NPF to elevated  $N_{\text{nuc}}$  via photochemical reactions. While at the HH site, the diurnal variation analysis indicated that  $N_{\text{nuc}}$  was influenced by primary emissions in early morning and at night, and was attributed to the NPF at noon. Weather conditions with strong solar radiation, high wind speed, low RH, and low condensation sink were found to be favorable for the NPF in the atmosphere of both rural and urban areas. In rural area, it was found that the formation rate of 5.5 nm particle had a power-law dependence on sulfuric acid concentration, with the typical power between 1 and 2, and the contribution of sulfuric acid vapor to the particle growth rate ranged from 9.2% to 52.5% on these NPF event days. Beside sulfuric acid vapor, monoterpenes were identified as the most important BVOC species related to the particle growth. Differently, the NPF events occurred at the urban site showed power-law correlations with  $\text{H}_2\text{SO}_4$  vapor concentrations but with the exponents larger than 2. It indicated different mechanisms of NPF at these two sites, and probably more complicated formation processes at the urban site than at the rural site. In addition, 4 nucleation mode particle burst events were identified

during the 30-day sampling campaign at the urban site. The  $N_{\text{nuc}}$  in the burst events had close correlation with  $\text{NO}_x$  and  $\text{SO}_2$ , implying that combustion sources with high sulfur-containing fuel might be the dominant emissions of the nucleation mode particles. Weather conditions with low wind, high RH and low temperature/solar radiation were often observed in these burst events. The calm wind was not beneficial to the dispersion of nucleation mode particles directly emitted from the combustion sources, whereas the high RH and low temperature enhanced the nucleation and condensation of the gaseous precursors emitted from the combustion sources to form nucleation mode particles.

In summary, a novel method using iron nanofilm detector to effectively quantify the number concentration of ambient acidic ultrafine particles was developed. Two collection systems, i.e., ESP and DS were modified or developed. The systematic and quantitative approach for the measurement of AUFPs using the detector samples collected by ESP and DS was established. The results of field measurements suggested that ESP and DS with the iron nanofilm detectors could be reliable tools to effectively measure the number concentration and size distribution of airborne AUFPs. The understanding of sources and formation of ultrafine particles at the rural and urban areas was significantly improved. The findings of this study indicated that most acidic particles in the atmosphere were ultrafine particles and relatively fresh, and new particle formation had a significant influence on the abundance of acidic particles in rural area. Fewer new particle formation events were observed in urban area mainly due to higher concentrations of pre-existing large surface area particles in urban area. The primary emissions from combustion sources

might have more important contribution to the level of acidic particle numbers in urban area.

## **8.2 Suggestions for future research**

### **8.2.1 Further data analysis and validation**

To further assess the reliability and efficiency of the detector method, and to more accurately quantify the number concentrations of acidic ultrafine particles in the atmosphere of Hong Kong, apart from the sampling campaigns at Mt. TMS and Hung Hom, we also conducted field sampling campaigns at two other sites, i.e., a residential/commercial site at Tung Chung (TC) and a background site at Hok Tsui (HT). Tung Chung (TC) site (22°16'60 N, 113°57'0 E), is a residential/commercial area situated on the north-western coast of Lantau Island in Hong Kong, just to the east of Tai O and south of Hong Kong International Airport at Chek Lap Kok. It is a relatively new town, but adjacent to the highway and railway lines that connect the airport with other islands of Hong Kong. The field measurement at the TC site was carried out for one month in warm season (02 August 2011 - 31 August 2011) and one month in cold season (08 November 2011- 15 December 2011). Hok Tsui (HT) site (22.21°N, 114.26°E) - a background site, is the Hong Kong Polytechnic University's atmospheric research station located in the southeastern tip of Hong Kong Island. Field measurement at the HT site was conducted simultaneously with the field measurements at the TC site for one month in warm season (02 August 2011 - 31 August 2011) and one month in cold season (08 November 2011- 15 December 2011). Moreover, sampling campaigns at the HH site were conducted again in another warm season (16

September 2011 - 12 October 2011) and another cold season (23 December 2011- 20 January 2012). In total, 304 ESP detector samples and 369 DS detector samples were collected from these field campaigns, i.e., 144 DS detectors at the TC site, 64 ESP and 72 DS detectors at the HT site, and 240 ESP and 153 DS detectors at the HH site.

Since a large number of detector samples were collected, further analysis to investigate the full contamination profiles of acidic ultrafine particles across the Hong Kong's territories would be carried out. In addition, NPF events at these different sampling locations should be studied in-depth to obtain the full picture of the nucleation and growth processes in Hong Kong region. The variations of number concentration and size distribution of AUFPs during the NPF events should be investigated and combined with meteorological parameters and gaseous pollutants for better understanding of the mechanisms of acidic particle formation.

### **8.2.2 Further development of the method**

Although AFM method is a promising technique for effective measurement of nano-scaled aerosol particles, the AFM instrument is expensive and bulky for in-situ applications. Hence, developing a method which can be widely used with low cost but high reliability will be a big challenge. The Quartz Crystal Microbalance (QCM) technique as a nanogram-resolution mass-sensing technique could be a proper choice. In order to measure the acidic UFP number concentrations in the atmosphere, special coating on the surface of the QCM sensor needs to be developed to enhance the adhesive force of acidic UFPs on electrodes. When ambient aerosol classified into each single

size range is concentrated and deposited onto the coated QCM sensor, the total mass of the sensing system will increase, causing the resonance frequency drop of the QCM sensor. The frequency shift is more prominent if there are more aerosol particles on the electrodes. The relation between the resonant frequency QCM sensors and mass loading can be calculated, and subsequently the particle number concentration can be determined.

In addition, we can try to find and utilize a color reagent which is very sensitive to the acidic particles to distinguish the acidic particles from non-acidic ones. Then much cheaper optical microscopy can replace the expensive AFM for fast color analysis. However, the particle size limit of this method needs to be evaluated and improved in order to make it suitable for the measurement of ultrafine size particles.

## References

- Abt, E., Suh, H.H., Catalano, P., and Koutrakis, P., 2000. Relative contribution of outdoor and indoor particle sources to indoor concentrations. *Environmental Science & Technology* 34, 3579- 3587.
- Alam, A., Shi, J. P., and Harrison, R. M., 2003. Observations of new particle formation in urban air. *Journal of Geophysical Research— Atmosphere* 108, 4093-4107.
- Amdur M O and Chen L C. 1989. Furnace-generated acid aerosols: Speciation and pulmonary effects. *Environmental Health Perspectives*, 79:147-150.
- Anastasio, C., Martin, S.T., 2001. Atmospheric nanoparticles. In: Banfield, J.F., Navrotsky, A. (Eds.), *Nanoparticles and the Environment*; Mineralogical Society of America 44, 293-349.
- Andersen, J.Z., Olsen, S.T., Andersen, K.K., et.al, 2010. Association between short-term exposure to ultrafine particles and hospital admissions for stroke in Copenhagen, Denmark. *European Heart Journal* 31(16), 2034-2040
- Anttila, T., Kerminen, V., 2003. Condensational growth of atmospheric nuclei by organic vapours. *Journal of Aerosol Science* 34, 41- 61.
- Arnold, F., Pirjola, L., Aufmhoff, H., Schuck, T., Lähde, T., Hämeri, K., 2006. First gaseous sulfuric acid measurements in automobile exhaust: implications for volatile nanoparticle formation. *Atmospheric Environment* 40, 7097-7105.
- Asmi, E., Kivekäs, N., Kerminen, V.-M., Komppula, M., Hyvärinen, A.-P., Hatakka, J., Viisanen, Y., and Lihavainen, H., 2011. Secondary new particle formation in Northern Finland Pallas site between the years 2000 and 2010. *Atmospheric Chemistry and Physics* 11, 12959-12972, doi:10.5194/acp-11-12959-2011.
- Ayers, G. P., and Gras, J. L., 1991. Seasonal relationship between cloud condensation nuclei and aerosol methanesulphonate in marine air. *Nature* 353(6347), 834-835.
- Bae, M.-S., Schwab, J.J., Hogrefe, O., Frank, B.P., Lala, G.G., and Demerjian, K.L., 2010. Characteristics of size distributions at urban and rural

- locations in New York. *Atmospheric Chemistry and Physics* 10, 4521-4535.
- Benson, D. R., Erupe, M. E., and Lee, S.-H., 2009. Laboratory measured H<sub>2</sub>SO<sub>4</sub>-H<sub>2</sub>O-NH<sub>3</sub> ternary homogeneous nucleation rates: Initial observations. *Geophysical Research Letters* 36, L15818, doi:10.1029/2009GL038728, 2009.
- Benson, D. R., Markovich, A., Al-Refai, M., and Lee, S.-H.: A Chemical Ionization Mass Spectrometer for ambient measurements of Ammonia. *Atmospheric Measurement Techniques* 3, 1075- 1087, doi:10.5194/amt-3-1075-2010, 2010.
- Berghmans, P., Bleux, N., Int Panis, L., Mishra, V. K., Torfs, R., and Van Poppel, M., 2009. Exposure assessment of a cyclist to PM<sub>10</sub> and ultrafine particles. *Science of The Total Environment* 407(4), 1286-1298.
- Bigg, E. K., Ono, A., Williams, A. J., 1974. Chemical tests for individual submicron aerosol particles. *Atmospheric Environment* 8, 1-13.
- Birmili, W. and Wiedensohler, A., 2000. New particle formation in the continental boundary layer: Meteorological and gas phase parameter influence, *Geophysical Research Letters* 27, 3325- 3328.
- Birmili, W., Berresheim, H., Plass-Dülmer, C., Elste, T., Gilge, S., Wiedensohler, A., and Uhrner, U., 2003. The Hohenpeissenberg aerosol formation experiment (HAFEX): A long term study including size-resolved aerosol, H<sub>2</sub>SO<sub>4</sub>, OH, and monoterpenes measurements. *Atmospheric Chemistry and Physics* 3, 361- 376.
- Bonn, B. and Moortgat, G. K., 2002. New particle formation during  $\alpha$ - and  $\beta$ -pinene oxidation by O<sub>3</sub>, OH and NO<sub>3</sub>, and the influence of water vapour: particle size distribution studies. *Atmospheric Chemistry and Physics* 2, 183- 196.
- Bonn, B., and Moortgat, G. K., 2003. Sesquiterpene ozonolysis: Origin of atmospheric new particle formation from biogenic hydrocarbons. *Geophysical Research Letters*, 30(11).
- Boy, M. and Kulmala, M., 2002. Nucleation events in the continental boundary layer: Influence of physical and meteorological parameters. *Atmospheric Chemistry and Physics* 2, 1- 16.

- Boy, M., Kulmala, M., Ruuskanen, T. M., Pihlatie, M., Reissell, A., Aalto, P.P., Keronen, P., Dal Maso, M., Hellen, H., Hakola, H., Janson, R., Hanke, M., and Arnold, F., 2005. Sulphuric acid closure and contribution to nucleation mode particle growth. *Atmospheric Chemistry and Physics* 5, 863- 878.
- Boy, M., Rannik, Ü., Lehtinen, K. E. J., Tavainen, V., Hakola, H., and Kulmala, M., 2003. Nucleation events in the continental boundary layer: Long-term statistical analyses of aerosol relevant characteristics. *Journal of Geophysical Research— Atmosphere* 108(D21), 4667, doi:10.1029/2003JD003838.
- Bräuner, E. V., Forchhammer, L., Møller, P., Simonsen, J., Glasius, M., Wählin, P., Raaschou-Nielsen, O., and Loft, S., 2007. Exposure to ultrafine particles from ambient air and oxidative stress- induced DNA damage. *Environmental Health Perspectives* 115, 1177- 1182.
- Buonanno, G., Ficco, G., and Stabile, L., 2009. Size distribution and number concentration of particles at the stack of a municipal waste incinerator. *Waste Management* 29,749-755.
- Burtscher, H., 2005. Physical characterization of particulate emissions from diesel engines: a review. *Aerosol Science & Technology* 36, 896-932.
- Bzdek, B. R., Pennington, M. R., and Johnston, M. V., 2012. Single particle chemical analysis of ambient ultrafine aerosol: A review. *Journal of Aerosol Science* 52, 109-120.
- Casati, R., Scheer, V., Vogt, R., Benter, T., 2007. Measurement of nucleation and soot mode particle emission from a diesel passenger car in real world and laboratory in situ dilution. *Atmospheric Environment* 41, 2125-2135.
- Charron, A., and Harrison, R.M., 2003. Primary particle formation from vehicle emissions during exhaust dilution in the road side atmosphere. *Atmospheric Environment* 37, 4109-4119.
- Chen, L.C., Qu, Q.S., Arndur, M.O., Gordon, T., and Fine, J.M., 1992. Effects of fine and ultrafine sulfuric acid aerosols in guinea pig alveolar macrophage: Alterations in macrophage function and intracellular pH. *Toxicology and Applied Pharmacology* 113:109-117.

- Chen, L.C., Wu, C.Y., Qu, Q.S., and Schlesinger, R. B. 1995. Number concentration and mass concentration as determinants of biological response to inhaled irritant particles. *Inhalation Toxicology* 7:577-588.
- Cheng, Y., Ho, K.F., Wu, W.J., Ho, S.H., Lee, S.C, Huang, Y., Zhang, Y.W., Yau, P.Sh., Gao, Y., Chan, C.S., 2012. Real-Time Characterization of Particle-Bound Polycyclic Aromatic Hydrocarbons at a Heavily Trafficked Roadside Site. *Aerosol and Air Quality Research* 12, 1181-1188.
- Cheung, H.C., Morawska, L., and Ristovski, Z.D., 2011. Observation of new particle formation in subtropical urban environment. *Atmospheric Chemistry and Physics* 11, 3823-3833.
- Choosong, T., Hata, M., and Furuuchi, M., 2010. Workplace environment and personal exposure of PM and PAHs to workers in natural rubber sheet factories contaminated by wood burning smoke. *Aerosol Air Quality Research* 10, 8-21.
- Chu, S.-H., 2004. PM<sub>2.5</sub> episodes as observed in the speciation trends network. *Atmospheric Environment* 38, 5237-5246.
- Chuang, H.C., Jones, T., Lung, S.C., and BéruBé. K., 2011. Soot-driven reactive oxygen species formation from incense burning. *Science of the Total Environment* 409, 4781-4787.
- Clarke, A. D., and Kapustin, V. N., 2002. A Pacific aerosol survey. Part I: A decade of data on particle production, transport, evolution, and mixing in the troposphere. *Journal of the Atmospheric Sciences*, 59(3), 363-382.
- Cohen, B. S., Heikkinen, M., Xiong, J. Q., Li, W., and Lippmann, M., 2004a. Field evaluation of nanofilm detectors for measuring acidic particles in indoor and outdoor air. *Research Report. Health Effects Institute* 121: 1-35.
- Cohen, B. S., Heikkinen, M. S., and Hazi, Y., 2004b. Airborne fine and ultrafine particles near the world trade center disaster site. *Aerosol Science and Technology* 38:338-348.
- Cohen, B. S., Li, W., Xiong, J. Q., and Lippmann, M., 2000. Detecting H<sup>+</sup> in ultrafine ambient aerosol using iron nano-film detectors and scanning probe microscopy. *Applied Occupational and Environmental Hygiene* 15:80-89.

- Cohen, B. S., Sussman, R.G., and Lippmann, M., 1990. Ultrafine particle deposition in a human tracheobronchial cast. *Aerosol Science and Technology* 12:1082-1091.
- Curtius, J., 2006. Nucleation of atmospheric aerosol particles. *Comptes Rendus Physique* 7(9), 1027-1045.
- Dal Maso, M., Kulmala, M., Riipinen, I., Wagner, R., Hussein, T., Aalto, P.P., Lehtinen, K.E.J., 2005. Formation and growth of fresh atmospheric aerosols eight years of aerosol size distribution data from SMEAR II, Hyytiälä, Finland. *Boreal Environmental Research* 10, 323-336.
- Dal Maso, M., Sogacheva, L., Aalto, P. P., Riipinen, I., Komppula, M., Tunved, P., Korhonen, L., Suur-Uski, V., Hirsikko, A., Kurtén, T., Kerminen, V.-M., Lihavainen, H., Viisanen, Y., Hansson, H.-C., and Kulmala, M., 2007 Aerosol size distribution measurements at four Nordic field stations: identification, analysis and trajectory analysis of new particle formation bursts, *Tellus*, 59B, 350- 361.
- Diapouli, E., Chaloulakou, A., and Spyrellis, N., 2007. Levels of ultrafine particles in different microenvironments — Implications to children exposure. *Science of the Total Environment* 388, 128-136.
- Dixkens, J., and Fissan, H., 1999. Development of an Electrostatic Precipitator for Off-Line Particle Analysis. *Aerosol Science and Technology* 30,438 - 453.
- Dockery, D. W., Pope III, C. A., Xu, X., Spengler, J. D., Ware, J. H., Fay, M. E., Ferris, B. G., and Speizer, F. E.,1993. An association between air pollution and mortality in six U.S. Cities. *New England Journal of Medicine* 329, 1753-1759.
- Donaldson, K., Brown, D., Clouter, A., Duffin, R., MacNee, W, Renwick, L., and Stone, V., 2002. The pulmonary toxicology of ultrafine particles. *Journal of Aerosol Medicine— Deposition Clearance and Effects in the Lung* 15, 213- 220.
- Draxler, R.R. and Hess, G.D.,1998. An overview of the HYSPLIT\_4 modelling system for trajectories, dispersion and deposition. *Australian Meteorological Magazine* 47, 295-308.
- Dunn, M.J., Jimenez, J.-L., Baumgardner, D., Castro, T., McMurry, P.H., and Smith, J.N.,2004. Measurements of Mexico City nanoparticle size

- distributions: observations of new particle formation and growth. *Geophysical Research Letters* 31, L10102.
- Edney, E. O., Kleindienst, T. E., Jaoui, M., Lewandowski, M., Offenberg, J. H., Wang, W., and Claeys, M., 2005. Formation of 2-methyltetrols and 2-methylglyceric acid in secondary organic aerosol from laboratory irradiated isoprene/NO<sub>x</sub>/SO<sub>2</sub>/air mixtures and their detection in ambient PM<sub>2.5</sub> samples collected in the eastern United States. *Atmospheric Environment* 39, 5281-5289.
- Eisele, F.L., and McMurry, P.H., 1997. Recent progress in understanding particle nucleation and growth. *The Royal Society* 352, 191- 201.
- Elimelech, M., and O'Meliat, C.R., 1990. Effect of particle size on collision efficiency in the deposition of brownian particles with electrostatic energy barriers. *Langmuir* 6: 1153-1163.
- Fang, G.C., Chang, C.N., Chu, C.C., Wu, Y.S., Fu, P.P.C., Chang, S.C., and Yang, I.L., 2003. Fine (PM<sub>2.5</sub>), Coarse (PM<sub>2.5-10</sub>), and metallic elements of suspended particulates for incense burning at Tzu Yun Yen Temple in central Taiwan. *Chemosphere* 51, 983-991.
- Fang, G.C., Chang, C.N., Wu, Y.S., Yang, C.J., Chang, S.C., and Yang, I.L., 2002. Suspended particulate variations and mass size distributions of incense burning at Tzu Yun Yen temple in Taiwan, Taichung. *Science of the total Environment* 299, 79-87.
- Fernández-Camacho, R., Rodríguez, S., de la Rosa, J., Sánchez de la Campa, A.M., Viana, M., Alastuey, A., and Querol, X., 2010. Ultrafine particle formation in the inland sea breeze airflow in Southwest Europe. *Atmospheric Chemistry and Physics* 10, 9615-9630.
- Gadi, R., Kulshrestha, U.C., Sarkar, A.K., Garg, S.C., and Parashar, D.C., 2003. Emissions of SO<sub>2</sub> and NO<sub>x</sub> from biofuels in India. *Tellus B* 55, 787-795.
- Fissan, H., Otto, E., and Dixkens, J., 1997. Particle transport in sampling lines used in fire detection systems. *Fire Safety Journal* 29, 205-215.
- Flagan, R. C., 2001. Electrical Techniques, in *Aerosol Measurement: Principles, Techniques, and Applications*, P. A. Baron and K. Willeke, ed., John Wiley, New York, 2nd Edition, pp. 537- 568.

- Friedbacher, G., Grasserbauer, M., Meslmani, Y., Klaus, N. Sz and Hignatsberger, M. J., 1995. Investigation of environmental aerosol by atomic-force microscopy. *Analytical Chemistry* 67, 1749-1754.
- Fu, P. Q. and Kawamura, K., 2011. Diurnal variations of polar organic tracers in summer forest aerosols: a case study of a Quercus and Picea mixed forest in Hokkaido, Japan. *Geochemical Journal* 45, 297- 308.
- Gadi, R., Kulshrestha, U. C., Sarkar, A. K., Garg, S. C., and Parashar, D. C., 2003. Emissions of SO<sub>2</sub> and NO<sub>x</sub> from biofuels in India. *Tellus B* 55,787-795.
- Gannet, H., Douglas, H. L., Galina, C., Randolph, D. B., and Christine, W., 2011. Persistent daily new particle formation at a mountain-top location. *Atmospheric Environment* 45, 4111-4115.
- Gao, J., Wang, T., Zhou, X. H., Wu, W. S., and Wang, W. X., 2009. Measurement of aerosol number size distributions in the Yangtze River delta in China:Formation and growth of particles under polluted conditions. *Atmospheric Environment* 43, 829-836.
- Gao, S., Ng, N. L., Keywood, M., Varutbangkul, V., Bahreini, R., Nenes, A., He, J., Yoo, K. Y., Beauchamp, J. L., Hodyss, R. P., Flagan, R. C., and Seinfeld, J. H., 2004. Particle phase acidity and oligomer formation in secondary organic aerosol. *Environmental Science and Technology*, 38, 6582-6589.
- Gaydos, T.M., Stainer, C.O., and Pandis, S.N., 2005. Modeling of insitu ultrafine atmospheric particle formation in the eastern United State. *Journal of Geophysical Research* 110, D07S12.
- Géhin, E., Ramalho, O., and Kirchner, S., 2008. Size distribution and emission rate measurement of fine and ultrafine particle from indoor human activities. *Atmospheric Environment* 42, 8341-8352
- Gerhard, E. R., and Johnson, H. F., 1955. Micro-determination of Sulfuric Acid Aerosol. *Analytical Chemistry* 27, 732.
- González, Y., Rodríguez, S., Guerra García, J.C., Trujillo, J.L., and García, R., 2011. Ultrafine particles pollution in urban coastal air due to ship emissions. *Atmospheric Environment* 45, 4907-4914.

- Griffin, R. J., Cocker III, D. R., Flagan, R. C., and Seinfeld, J. H., 1999. Organic aerosol formation from the oxidation of biogenic hydrocarbons. *Journal of Geophysical Research* 104(D3), 3555- 3567.
- Guo, H., Ding, A. J., Morawska, L., He, C., Ayoko, G., Li, Y. S. and Hung, W. T., 2008. Size distribution and new particle formation in subtropical eastern Australia. *Environmental Chemistry* 56, 382-390,
- Guo, H., Ding, A.J., So, K.L., Ayoko, G., Li, Y.S., and Hung, W.T., 2009. Receptor modeling of source apportionment of Hong Kong aerosols and the implication of urban and regional contribution. *Atmospheric Environment* 43, 1159-1169.
- Guo, H., Morawska, L., He, C., Zhang, Y. L., Ayoko, G., and Cao, M., 2010. Characterization of particle number concentrations and PM<sub>2.5</sub> in a school: influence of outdoor air pollution on indoor air. *Environmental Science and Pollution Research* 176, 1268-1278.
- Gwynn, R. C., and Thurston, G. D., 2001. The burden of air pollution: impacts among racial minorities. *Environmental Health Perspectives* 109 (Suppl 4), 501- 506.
- Hagler, G. S. W., Baldauf, R. W., Thoma, E. D., Long, T. R., Snow, R. F., Kinsey, J. S., Oudejans, L., and Gullett, B. K., 2009. Ultrafine particles near a major roadway in Raleigh, North Carolina: Downwind attenuation and correlation with traffic-related pollutants. *Atmospheric Environment* 43, 229-1234.
- Hamed, A., Joutsensaari, J., Mikkonen, S., Sogacheva, L., Dal Maso, M., Kulmala, M., Cavalli, F., Fuzzi, S., Facchini, M. C., Decesari, S., Mircea, M., Lehtinen, K. E. J., and Laaksonen, A., 2007. Nucleation and growth of new particles in Po Valley, Italy. *Atmospheric Chemistry and Physics* 7, 355- 376.
- Hamed, A., Korhonen, H., Sihto, S.-L., Joutsensaari, J., Järvinen, H., Petäjä, T., Arnold, F., Nieminen, T., Kulmala, M., Smith, J. N., Lehtinen, K. E. J., and Laaksonen, A., 2011. The role of relative humidity in continental new particle formation. *Journal of Geophysical Research* 116.
- Hao, L. Q., Romakkaniemi, S., Yli-Pirilä, P., Joutsensaari, J., Kortelainen, A., Kroll, J. H., Miettinen, P., Vaattovaara, P., Tiitta, P., Jaatinen, A., Kajos, M. K., Holopainen, J. K., Heijari, J., Rinne, J., Kulmala, M., Worsnop, D.

- R., Smith, J. N., and Laaksonen, A., 2011. Mass yields of secondary organic aerosols from the oxidation of  $\alpha$ -pinene and real plant emissions. *Atmospheric Chemistry and Physics* 11, 1367- 1378.
- Hatch, L. E., Creamean, J. M., Ault, A. P., Surratt, J. D., Chan, M. N., Seinfeld, Y., and Prather, K. A., 2011. Measurements of isoprene-derived organosulfates in ambient aerosols by aerosol time-of-flight mass spectrometry - part 1: single particle atmospheric observations in Atlanta. *Environment Science and Technology* 45, 5105-5111,.
- Hattis, D., Abdollahzadeh, S., and Franklin, C.A., 1990. Strategies for testing the "irritation-signaling" model for chronic lung effects of fine acid particles. *Journal of Air and Waste Management Association* 40, 322- 330.
- Hattis, D., Wasson, J.M., Page, G.S., Stern, B., Franklin, C.A., 1987. Acid particles and the tracheobronchial region of the respiratory system: An "irritation-signaling" model for possible health effects. *Journal of the Air Pollution Control Association* 37,1060- 1066.
- Hayashi, H., KOSHI, S., and SAKABE, H.,1961. Determination of Mist Size by Metal Coated Glass Slide. *Bullet of National Institute of Industrial Health* 6, 35.
- Healy, R.M., O'Connor, I.P., Hellebust, S., Allanic, A., Sodeau, J.R., Wenger, J.C., 2009. Characterisation of single particles from in-port ship emissions. *Atmospheric Environment* 43, 6408-6414.
- Heyder, J., Beck-Speier, I., Ferron, G. A., Josten, M., Karg, E., Kreyling, W. G., ... and Schulz, H., 2009. Long-term responses of canine lungs to acidic particles. *Inhalation toxicology* 21(11), 920-932.
- Hinds, W. C., 1999. *Aerosol Technology: Properties, Behavior, and Measurement of Airborne Particles*, 2nd Edition. Wiley, New York.
- Hoek, G., Boogaard, H., Knol, A., de Hartog, J., Slottje, P., and Ayres, J.G., 2010. Concentration response functions for ultrafine particles and all-cause mortality and hospital admissions: results of a European expert panel elicitation. *Environment Science and Technology* 44, 476-482.
- Hoek, G., Kos, G., Harrison, R., de Hartog, J., Meliefste, K., ten Brink, H., Katsouyanni, K., Karakatsani, A., Liangou, M., Kotronarou, A., and Hämeri, K., 2008. Indoor-outdoor relationships of particle number and mass in four European cities. *Atmospheric Environment* 42, 156- 169.

- Hoffmann, T., O'Dowd, C.D., and Seinfeld, J.H., 2001. Iodine oxide homogeneous nucleation: an explanation for coastal new particle production. *Geophysical Research Letters* 28, 1949-1952.
- Hogrefe, O., Lala, G. G., Frank, B. P., Schwab, J. J., and Demerjian, K. L., 2006. Field evaluation of a TSI model 3034 scanning mobility particle sizer in New York city: winter 2004 intensive campaign. *Aerosol Science and Technology* 40, 753-762.
- Holmes, N., 2007. A review of particle formation events and growth in the atmosphere in the various environments and discussion of mechanistic implications. *Atmospheric Environment* 41, 2183-2201.
- Hong Kong Annual Traffic Census 2010 and 2011. Hong Kong Transport Department.
- Horstman, Jr., Sanford, W., and Wagman, J., 1967. Size Analysis of Acid Aerosols by a Metal Film Technique. *American Industrial Hygiene Association Journal* 28(6), 523-530.
- Horvath, H., 2008. Conference on visibility aerosols and atmospheric optics, Vienna September 3-6 2006. *Atmospheric Environment* 42, 2569-2570.
- Huang, P. F., and Turpin, B., 1996. Reduction of sampling and analytical errors for electron microscopic analysis of atmospheric aerosols. *Atmospheric Environment* 30, 4137-4148.
- Iinuma, Y., Müller, C., Böge, O., Gnauk, T., and Herrmann, H., 2007. The formation of organic sulfate esters in the limonene ozonolysis secondary organic aerosol (SOA) under acidic conditions. *Atmospheric Environment* 41, 5571-5583.
- Jang, M. S., Czoschke, N. M., Lee, S., and Kamens, R. M., 2002. Heterogeneous atmospheric aerosol production by acid-catalyzed particle-phase reactions. *Science* 298:814-817.
- Janson, R., Rosman, K., Karlsson, A., and Hansson, H. C., 2001. Biogenic emissions and gaseous precursors to forest aerosols. *Tellus B* 53, 423-440.
- Jeong, C.H., Hopke, P.K., Chalupa, D., and Utell, M., 2004. Characteristics of nucleation and growth events of ultrafine particles measured in Rochester, NY. *Environmental Science & Technology* 38, 1933-1940.

- Jetter, J.J., Guo, Z., McBrian, J.A., Flynn, and M.R., 2002. Characterization of emissions from burning incense. *Science of the Total Environment* 295, 51-67.
- Jimenez, J. L., Canagaratna, M. R., Donahue, N. M., et al., 2009. Evolution of organic aerosols in the atmosphere. *Science* 326, 1525- 1529.
- Joshi, M., Sapra, B. K., Khan, A., Tripathi, S. N., Shamjad, P. M., Gupta, T., and Mayya, Y. S., 2012. Harmonisation of nanoparticle concentration measurements using GRIMM and TSI scanning mobility particle sizers. *Journal of nanoparticle Research* 14, 1-14.
- Kamens, R. M., Zhang, H., Chen, E. H., Zhou, Y., Parikh, H. M., Wilson, R. L., Galloway, K. E., and Rosen, E. P., 2011. Secondary organic aerosol formation from toluene in an atmospheric hydrocarbon mixture: water and particle seed effects. *Atmospheric Environment* 45, 2324- 2334.
- Karasev, V.V., Ivanova, N.A., Sadykova, A.R., Kukhareva, N., Baklanov, A.M., Onischuk, A.A., Kovalev, F.D., Beresnev, S.A., 2004. Formation of charged soot aggregates by combustion and pyrolysis: charge distribution and photophoresis. *Journal of Aerosol Science* 35, 363-381.
- Kerminen, V.-M., Virkkula, A., Hillamo, R., Wexler, A. S., Kulmala, M., 2000. Secondary organics and atmospheric cloud condensation nuclei production. *Journal of Geophysical Research* 105 (D7): 9255-9264.
- Kerminen, V. M., Lehtinen, K. E. J., Anttila, T., and Kulmala, M., 2004. Dynamics of atmospheric nucleation mode particles: a timescale analysis. *Tellus B* 56, 135- 146.
- Kerminen, V.-M., Petäjä, T., Manninen, H. E., et al., 2010. Atmospheric nucleation: highlights of the EUCAARI project and future directions *Atmospheric Chemistry and Physics* 10, 10829- 10848.
- Kerminen, V.M., Pirjola, L., and Kulmala, M., 2001. How significantly does coagulation limit atmospheric particle production? *Journal of Geophysical Research* 106 (D20), 24119- 24125.
- Kiendler-Scharr, A., Wildt, J., DalMaso, M., Hohaus, T., Kleist, E., Mentel, T. F., Tillmann, R., Uerlings, R., Schurr, U., and Wahner, A., 2009. New particle formation in forests inhibited by isoprene emissions. *Nature* 461, 381- 384.

- Kimmel, T. A., Chen, L. C., Bosland, M. C., and Nadziejko, C., 1997. Influence of acid aerosol droplet size on structural changes in the rat lung caused by acute exposure to sulfuric acid and ozone. *Toxicology and applied pharmacology* 144(2), 348-355.
- Kittelson, D. B., 1998. Engine and nanoparticles: a review. *Journal of Aerosol Science* 29, 575-588.
- Kittelson, D.B., Watts, W.F., Johnson, J.P., and Lawson, D.R., 2006. On-road and laboratory evaluation of combustion aerosol - part 2: summary of spark ignition engine results. *Journal of Aerosol Science* 37, 931-949.
- Kivekäs, N., Sun, J., Zhan, M., Kerminen, V.-M., Hyvärinen, A., Komppula, M., Viisanen, Y., Hong, N., Zhang, Y., Kulmala, M., Zhang, X.-C., Deli-Geer, and Lihavainen, H., 2009. Long term particle size distribution measurements at Mount Waliguan, a high-altitude site in inland China. *Atmospheric Chemistry and Physics* 9, 5461-5474.
- Kleinman, M. T., and Phalen, R. F., 2006. Toxicological interactions in the respiratory system after inhalation of ozone and sulfuric acid aerosol mixtures. *Inhalation toxicology* 18(4), 295-303.
- Knutson, E. O., 1999. History of diffusion batteries in aerosol measurement. *Aerosol Science and Technology* 31:83-128
- Komppula, M., Dal Maso, M., Lihavainen, H., Aalto, P. P., Kulmala, M., and Viisanen, Y., 2003. Comparison of new particle formation events at two locations in northern Finland. *Boreal Environmental Research* 8, 395- 404.
- Kuang, C., McMurry, P.H., McCormick, A.V., Eisele, F.L., 2008. Dependence of nucleation rates on sulfuric acid vapor concentration in diverse atmospheric locations. *Journal of Geophysical Research* 113, D10209.
- Kulmala, M., and Kerminen, V., 2008. On the formation and growth of atmospheric nanoparticles. *Atmospheric Research* 90, 132-150.
- Kulmala, M., Kontkanen, J., Junninen, H., Lehtipalo, K., Manninen, H. E., Nieminen, T., ... & Worsnop, D. R., 2013. Direct observations of atmospheric aerosol nucleation. *Science* 339(6122), 943-946.
- Kulmala, M., Vehkamäki, H., Petaja, T., Dal Maso, M., Lauri, A., Kerminen, V.-M., Birmili, W., McMurry, P.H., 2004a. Formation and growth rates of ultrafine particles: a review of observations. *Journal of Aerosol Science* 35, 143-176.

- Kulmala, M., Laakso, L., Lehtinen, K. E. J., Riipinen, I., Dal Maso, M., Anttila, T., Kerminen, V.-M., Hörrak, U., Vana, M., and Tammet, H., 2004b: Initial steps of aerosol growth. *Atmospheric Chemistry and Physics* 4, 2553-2560.
- Kulmala, M., Lehtinen, K., and Laaksonen, A., 2006. Cluster activation theory as an explanation of the linear dependence between formation rate of 3 nm particles and sulphuric acid concentration. *Atmospheric Chemistry and Physics* 6, 787-793.
- Kulmala, M., Dal Maso, M., Makela, J. M., Pirjola, L., Vakeva, P., Aalto, P., Miikkulainen, K., Hameri, and O'Dowd, C. D., 2001. On the formation, growth and composition of nucleation mode particles. *Tellus B* 53, 479-490.
- Kulmala, M., Petäjä, T., Mönkkönen, P., Koponen, I. K., Dal Maso, M., Aalto, P. P., Lehtinen, K. E. J., and Kerminen, V.-M., 2005. On the growth of nucleation mode particles: source rates of condensable vapour in polluted and clean environments. *Atmospheric Chemistry and Physics* 5, 409- 416.
- Kulmala, M., Pirjola, U., and Makela, J. M., 2000. Stable sulphate clusters as a source of new atmospheric particles. *Nature* 404 (6773), 66- 69.
- Kumar, P., Pirjola, L., Ketzel, M., and Harrison, R.M. 2013. Nanoparticle emissions from 11 non-vehicle exhaust sources - a review. *Atmospheric Environment* 67, 252- 277.
- Kumar, P., Robins, A., Vardoulakis, S., and Britter, R., 2010. A review of the characteristics of nanoparticles in the urban atmosphere and the prospects for developing regulatory controls. *Atmospheric Environment* 44, 5035-5052.
- Kurtén, T., Noppel, M., Vehkamäki, H., Salonen, M., and Kulmala, M., 2007. Quantum chemical studies of hydrate formation of H<sub>2</sub>SO<sub>4</sub> and HSO<sub>4</sub><sup>-</sup>. *Boreal Environmental Research* 12, 431- 453,.
- Laakso, L., Mäkelä, J. M., Pirjola, L., Kulmala, M., 2002. Model studies on ion-induced nucleation in the atmosphere. *Journal of Geophysical Research*, 107 D20 4427.
- Laakso, L., Petäjä, T., Lehtinen, K., Kulmala, M., Paatero, J., Hörrak, U., Tammet, H., Joutsensaari, J., 2004. Ion production rate in a boreal forest

- based on ion particle and radiation measurements. *Atmospheric Chemistry and Physics* 4, 1933-1943
- Laaksonen, A., Kulmala, M., O'Dowd, C. D., et al., 2008. The role of VOC oxidation products in continental new particle formation. *Atmospheric Chemistry and Physics* 8, 2657-2665.
- Lee, S. C., and Wang, B., 2004. Characteristics of emissions of air pollutants from burning of incense in a large environmental chamber. *Atmospheric Environment* 38, 941-951.
- Lee, S.C., and Wang, B., 2006. Characteristics of emissions of air pollutants from mosquito coils and candles burning in a large environmental chamber. *Atmospheric Environment* 40, 2128-2138.
- Lee, Y., Lee, H., Kim, M., Choi, C. Y., and Kim, J., 2008. Characteristics of particle formation events in the coastal region of Korea in 2005. *Atmospheric Environment* 42, 3729- 3739, 2008.
- Li, Y.J., Cheong, G., Lau A.P., and Chan, C.K., 2010a. Acid-catalyzed particle-phase reactions of limonene and terpineol and their impacts on gas-to-particle partitioning in the formation of organic aerosols". *Environment Science and Technology* 44, 5483-5489.
- Li, H., Han, Z., Cheng, T., Du, H., King, L., Chen, J., Zhang, R., and Wang, W., 2010b. Agricultural fire impacts on the air quality of shanghai during summer harvest time. *Aerosol Air Quality Research* 10, 95-101.
- Li, N., Sioutas, C., Cho, A., Schmitz, D., Misra, C., Sempf, J., Wang, M., Oberley, T., Froines, J., and Nel, A., 2003. Ultrafine particulate pollutants induce oxidative stress and mitochondrial damage. *Environmental Health Perspective* 111, 455- 460.
- Lingard, J.J.N., Agus, E.L., Young, D.T., Andrews, G.E., and Tomlin, A.S., 2006. Observations of urban airborne particle number concentrations during rush-hour conditions: analysis of the number based size distributions and modal parameters. *Journal of Environmental Monitoring* 8, 1203-1218.
- Lioy, P. J, Waldman, J. M., 1989. Acidic sulfate aerosols: characterization and exposure. *Environment Health Perspectives* 79, 15-34.
- Lippmann, M., 1989. Progress prospects and research needs on the health effects of acid aerosols. *Environment Health Perspectives*, 79:203-205.

- Lippmann, M., 2000. Environmental toxicants: human exposures and their health effects--Sulfur oxides: acidic aerosols and SO<sub>2</sub>. New York, John Wiley and Sons: 771-809.
- Lipsky, E.M., and Robinson, A.L., 2006. Effects of dilution on fine particle mass and partitioning of semivolatile organics in diesel exhaust and wood smoke. *Environment Science & Technology* 40, 155-162.
- Liu, S., Hu, M., Wu, Z. J., Wehner, B., Wiedensohler, A., and Cheng, Y. F., 2008. Aerosol number size distribution and new particle formation at a rural/coastal site in Pearl River Delta (PRD) of China. *Atmospheric Environment* 25, 6275- 6283.
- Lodge, J.P., and Havlik, B.R., 1960. Evaporated metal films as indicators of atmospheric pollution. *International journal of air and water pollution* 3, 249.
- Mäkelä, J. M., Dal Maso, M., Pirjola, L., Keronen, P., Laakso, L. et al., 2000. Characteristics of the atmospheric particle formation events observed at a boreal forest site in southern Finland. *Boreal Environment Research* 5, 299- 313.
- Malm, W.C., and Day, D.E., 2001. Estimates of aerosol species scattering characteristics as a function of relative humidity. *Atmospheric Environment* 35, 2845-2860.
- Mamane, Y., 1977. A quantitative method for the detection of individual submicron sulfate particles[D]:[Ph.D.]. USA:Pennsylvania State University.
- Manoukian, A., Quivet, E., Temime-Roussel, B., Nicolas, M., Maupetit, F., and Wortham, H., 2013. Emission characteristics of air pollutants from incense and candle burning in indoor atmospheres. *Environmental Science and Pollution Research* 20, 4659-4670.
- Marti, J. J., R. J. Weber, P. H. McMurry, F. Eisele, D. Tanner, and Jefferson, A., 1997. New particle formation at a remote continental site: assessing the contributions of SO<sub>2</sub> and organic precursors. *Journal of Geophysical Research* 102, 6331- 6339.
- McFiggans, G., 2005. Atmospheric science: Marine aerosols and iodine emissions. *Nature*, 433(7026), E13-E13.

- McGranahan, G., and Murray, F., 2003. Air pollution and health in rapidly developing countries. Stockholm Environment Institute, Earthscan publications Ltd., p. 30-31.
- McGraw, R., and Zhang, R., 2008. Multivariate analysis of homogeneous nucleation rate measurements: Nucleation in the p-toluic acid/sulfuric acid/water system. *The Journal of Chemical Physics* 128, 064508.
- McMurry, P.H., Kuang, C.A., Smith, J.N., Zhao, J., and Eisele, F., 2011. Atmospheric New Particle Formation: Physical and Chemical Measurements. *Aerosol Measurement*, John Wiley & Sons, Inc., 681-695.
- Mikkonen S., Romakkaniemi S., Smith J.N., Korhonen H., Petäjä T., Plass-Duelmer C., Boy M., McMurry P.H., Lehtinen K.E.J., Joutsensaari J., Hamed A., Mauldin III R.L., Birmili W., Spindler G., Arnold F., Kulmala M. and Laaksonen A., 2011. A statistical proxy for sulphuric acid concentration. *Atmospheric Chemistry and Physics* 11, 11319- 11334.
- Modini, R., Ristovski, Z., Johnson, G. R., He, C.R., Surawski, N., Morawska, L., Suni, T., and Kulmala, M., 2009. New particle formation and growth at a remote, sub-tropical coastal location. *Atmospheric Chemistry and Physics* 9, 7607-7621.
- Molnar, P., Janhall, S., et al., 2002. Roadside measurements of fine and ultrafine particles at a major road north of Gothenburg. *Atmospheric Environment* 36 (25), 4115- 4123.
- Morawaska, L., Ristovski, Z., Jayaratne, E. R., Keogh, D. U., Ling, X., 2008. Ambient nano and ultrafine particles from motor vehicle emissions: Characteristics, ambient processing and implications on human exposure. *Atmospheric Environment* 42, 8113-8138.
- Morawska, L., Bofinger, N.D., Kocis, D., Nwankwoala, A., 1998a. Submicrometer and supermicrometer particles from diesel vehicle emissions. *Environmental Science and Technology* 32 (14), 2033-2042.
- Morawska, L., Thomas, S.B., Bofinger, N.D., Wainwright, D., Neale, D., 1998b. Comprehensive characterization of aerosols in a subtropical urban atmosphere: particle size distribution and correlation with gaseous pollutants. *Atmospheric Environment* 32, 2467-2478.

- Morawska, L., Moore, M. R., and Ristovski, Z. D., 2004. Health impacts of ultrafine particles. Canberra (Australia): Australian Department of the Environment and Heritage.
- Musialik-Piotrowska, A., Kordylewski, W., Ciolek, J., Moscicki, K., 2010. Characteristics of air pollutants emitted from biomass combustion small retort boiler. *Environment Protection Engineering* 36, 123-131.
- Napierska, D., Thomassen, L. C. J., Rabolli, V., Lison, D., Gonzalez, L., Kirsch-Volders, M., Martens, J. A., and Hoet, P.H., 2009. Size-Dependent Cytotoxicity of Monodisperse Silica Nanoparticles in Human Endothelial Cells. *Small* 5, 846- 853.
- NARSTO, 2003. Particulate Matter Science for Policy Makers: A NARSTO Assessment. In: McMurry, P., Shepher, M., Vicker, J. (Eds.), EPRI, Palo Alto, CA, USA.
- Neitola, K., Asmi, E., Komppula, M., Hyvarinen, A.P., Raatikainen, T., Panwar, T.S., Sharma, V.P., and Lihavainen, H., 2011. New particle formation infrequently observed in Himalayan foothills e why? *Atmospheric Environment* 11, 8447-8458.
- Nieminen, T., Lehtinen, K. E. J., and Kulmala, M., 2010. Sub-10 nm particle growth by vapor condensation - effects of vapor molecule size and particle thermal speed. *Atmospheric Chemistry and Physics* 10, 9773-9779.
- Nilsson, E.D., and Kulmala, M., 1998. The potential for atmospheric mixing processes to enhance the binary nucleation rate. *Journal of Geophysical Research* 103 (D1),1381- 1389.
- O'Dowd, C.D., Hämeri, K., Makela, J.M., Vakeva, M., Aalto, P.P., de Leeuw, G., Kunz, G.J., Becker, E., Hansson, H.C., Allen, A.G., Harrison, R.M., Berresheim, H., Geever, M., Jennings, S. G., and Kulmala, M., 2002a. Coastal new particle formation: Environmental conditions and aerosol physicochemical characteristics during nucleation bursts. *Journal of Geophysical Research* 107 8107 doi:8110,1029/2001JD000 206.
- O'Dowd, C.D., Hämeri, K., Mäkelä, J.M., Pirjola, L., Kulmala, M., Jennings, S.G., et al., 2002b. A dedicated study of new particle formation and fate in the coastal environment PARFORCE: overview of objectives and achievements. *Journal of Geophysical Research* 107 D19 8108.

- Oberdörster, G., Finkelstein, J.N., Johnson, C., Gelein, R., Cox, C., Baggs, R., and Elder, A.C.P., 2000. Acute Pulmonary Effects of Ultrafine Particles in Rats and Mice. Research Report 96. Health Effects Institute, Cambridge MA.
- Oberdörster, G., Oberdörster, E., and Oberdörster, J., 2005. Nanotoxicology: an emerging discipline evolving from studies of ultrafine particles. *Environmental Health Perspectives* 113, 823- 839.
- Oberdörster, G., Sharp, Z., Atudorei, V., Elder, A., Gelein, R., Kreyling, W., and Cox, C., 2004. Translocation of inhaled ultrafine particles to the brain. *Inhalation Toxicology* 16, 437- 445.
- O'Dowd, C. D., and Hoffmann, T., 2006. Coastal new particle formation: A review of the current state-of-the-art. *Environmental Chemistry* 2(4), 245- 255.
- O'Dowd, C. D., Facchini, M. C., Cavalli, F., Ceburnis, D., Mircea, M., Decesari, S., et al., 2004. Biogenically driven organic contribution to marine aerosol. *Nature* 431(7009), 676-680.
- Paasonen, P., Nieminen, T., Asmi, E., Manninen, H. E., Petäjä, T., Plass-Dülmer, C., Flentje, H., Birmili, W., Wiedensohler, A., Hörrak, U., Metzger, A., Hamed, A., Laaksonen, A., Facchini, M. C., Kerminen, V.-M., and Kulmala, M., 2010. On the roles of sulphuric acid and low-volatility organic vapours in the initial steps of atmospheric new particle formation. *Atmospheric Chemistry and Physics* 10, 11223-11242.
- Park, K., Park, J., Kwak, J., Cho, G., and Kim, J., 2008. Seasonal and diurnal variations of ultrafine particle concentration in urban Gwangju, Korea: Observation of ultrafine particle events. *Atmospheric Environment* 42, 788-799.
- Pathak, R. K., Louie, P. K. K., and Chan, C. K., 2004. Characteristics of aerosol acidity in Hong Kong. *Atmospheric Environment* 38, 2965-2974.
- Pathak, R. K., Yao, X. H., Alexis, K. H., and Chan, C. K., 2003. Acidity and concentrations of ionic species of PM<sub>2.5</sub> in Hong Kong. *Atmospheric Environment* 37, 1113- 1124.
- Petäjä, T., Mauldin, R.L., Kosciuch, E., McGrath, J., Nieminen, T., Paasonen, P., Boy, M., Adamov, A., Kotiaho, T., and Kulmala, M., 2009. Sulfuric

- acid and OH concentrations in a boreal forest site. *Atmospheric Chemistry and Physics* 9, 7435-7448.
- Pirjola, L., and Kulmala, M., 2001. Development of particle size and composition distributions with a novel aerosol dynamics model. *Tellus B* 53, 491- 509.
- Pirjola, L., Kulmala, M., Wilck, M., Bischoff, A., Stratmann, F., and Otto, E., 1999. Formation of Sulphuric Acid Aerosols and Cloud Condensation Nuclei: An Expression for Significant Nucleation and Model Comparison. *Journal of Aerosol Science*, 30(8), 1079-1094.
- Pohjola, M., Pirjola, L., et al., 2003. Modelling of the influence of aerosol processes for the dispersion of vehicular exhaust plumes in street environment. *Atmospheric Environment* 37 (3), 339- 351.
- Pope, C.A., Burnett, R.T., Thun, M.J., Calle, E.E., Krewski, D., Ito, K., 2002. Lung cancer cardiopulmonary mortality and long-term exposure to fine particulate air pollution. *The Journal of the American Medical Association* 287, 1132-1141.
- Pope, C. A., Thun, M. J., Namboodiri, M. M., Dockery, D. W., Evans, J. S., Speizer, F. E., and Heath Jr., C. W., 1995. Particulate air pollution as a predictor of mortality in a prospective study of U.S. adults. *American Journal of Respiratory and Critical Care Medicine* 151, 669-674.
- Qian, S., Sakurai, H., and McMurry, P.H., 2007. Characteristics of regional nucleation events in urban East St. Louis. *Atmospheric Environment* 41, 4119-4127.
- Radojević, M. and Harrison, R.M., 1992. *Atmospheric acidity: sources, consequences, and abatement*. Environmental management series published by Elsevier science publisher Ltd.
- Raes, F., Van Dingenen, R., Cuevas, E., Van Velthoven, P. F., and Prospero, J. M., 1997. Observations of aerosols in the free troposphere and marine boundary layer of the subtropical Northeast Atlantic: Discussion of processes determining their size distribution. *Journal of Geophysical Research- Atmospheres* (1984- 2012), 102(D17), 21315-21328.
- Ramgolam, K., Chevaillier, S., Marano, F., Baeza-Squiban, A., and Martinon, L., 2008. Proinflammatory effect of fine and ultrafine particulate matter

- using size-resolved urban aerosols from Paris. *Chemosphere* 72,1340-1346.
- Riipinen, I., Sihto, S.L., Kulmala, M., Arnold, F., Dal Maso, M., Birmili, W., Saarnio, K., Teinila, K., Kerminen, V.M., Laaksonen, A., Lehtinen, K.E.J., 2007. Connections between atmospheric sulphuric acid and new particle formation during QUEST III-IV campaigns in Heidelberg and Hyytiälä. *Atmospheric Chemistry and Physics* 7, 1899-1914.
- Riipinen, I., Pierce, J. R., Yli-Juuti, T., Nieminen, T., Häkkinen, S., Ehn, M., Junninen, H., Lehtipalo, K., Petäjä, T., Slowik, J., Chang, R., Shantz, N. C., Abbatt, J., Leaitch, W. R., Kerminen, V.-M., Worsnop, D. R., Pandis, S. N., Donahue, N. M., and Kulmala, M., 2011. Organic condensation: a vital link connecting aerosol formation to cloud condensation nuclei (CCN) concentrations. *Atmospheric Chemistry and Physics* 11, 3865-3878.
- Rinne, J., Bäck, J., and Hakola, H., 2009. Biogenic volatile organic compound emissions from the Eurasian taiga: current knowledge and future directions. *Boreal Environmental Research* 14(4), 807-826.
- Ristovski, Z., Morawska, L., et al., 1998. Submicrometer and supermicrometer particulate emission from spark ignition vehicles. *Environmental Science and Technology* 32, 3845- 3852.
- Rodríguez, S., and Cuevas, E., 2007. The contributions of “minimum primary emissions” and “new particle formation enhancements” to the particle number concentration in urban air. *Journal of Aerosol Science* 38, 1207-1219.
- Rodríguez, S., Van Dingenen, R., Putaud, J.-P., Martins-Dos Santos, S., and Roselli, D., 2005. Nucleation and growth of new particles in the rural atmosphere of Northern Italy -relationship to air quality monitoring. *Atmospheric Environment* 39, 6734- 6746.
- Ronald, E.W., and Lawrence, J.F., 1995. Health effects of acid aerosols. *Water Air and Soil Pollution* 85, 177-188.
- Ronald, J. F., Allan, L. L., and John W. W., 1983. Electron microscopy of acidic aerosols collected over the northeastern United States. *Atmospheric Environment* 8, 1545-1561.

- Rose, D., Wehner, B., Ketzler, M., Engler, C., Voigtländer, J., Tuch, T., and Wiedensohler, A., 2006. Atmospheric number size distributions of soot particles and estimation of emission factors. *Atmospheric Chemistry and Physics* 6, 1021-1031.
- Sakurai, H., Tobias, K., Park, D., Zarling, K.S., Docherty, D., Kittelson, D.B., McMurry, P.H., and Zeimann, P.J., 2003. On-line measurements of diesel nanoparticle composition and volatility. *Atmospheric Environment* 37, 1199-1210.
- Schlatter, J., 2006. Comparison of Grimm and TSI Condensation Particle Counters, 10 ETH-Conference on Combustion Generated Particles, August 21 - 23.
- Schlesinger, R.B., 1989. Factors affecting the response of lung clearance system to acid: aerosols role of exposure concentration, exposure time, and relative acidity. *Environmental Health Perspectives* 79, 121- 126.
- Schlesinger, R. B., and Cassee, F., 2003. Atmospheric secondary inorganic particulate matter: the toxicological perspective as a basis for health effects risk assessment. *Inhalation toxicology*, 15(3), 197-235.
- Schwartz, J., 2001. Air pollution and blood markers of cardiovascular risk. *Environmental Health Perspective* 109 (Suppl. 3), 405- 409.
- Scott, W.D., and Cattell, F.C.R., 1979. Vapor pressure of ammonium sulfates. *Atmospheric Environment* 13, 307- 317.
- Seinfeld, J.H., and Pandis, S.N., 2006. *Atmospheric Chemistry and Physics, from Air Pollution to Climate Change*. John Wiley, New York, 1203 pp.
- Semmler, M., Mann, E. K., Rička, J., and Borkovec, M., 1998. Diffusional deposition of charged latex particles on water-solid interfaces at low ionic strength. *Langmuir* 14, 5127-5132.
- Shen, X.J., Sun, J.Y., Zhang, Y.M., Wehner, B., Nowak, A., Tuch, T., Zhang, X.C., Wang, T.T., Zhou, H.G., Zhang, X.L., Dong, F., Birmili, W., and Wiedensohler, A., 2011. First long-term study of particle number size distributions and new particle formation events of regional aerosol in the North China Plain. *Atmospheric Chemistry and Physics* 11, 1565-1580.
- Shi, J. P., Evans, D. E., Khan, A.A., and Harrison, R.M., 2001. Sources and concentration of nanoparticles (less than 10nm diameter) in the urban atmosphere. *Atmospheric Environment* 35, 1193-1202.

- Shi, J.P., and Harrison, R.M., 1999. Investigation of ultrafine particle formation during diesel exhaust dilution. *Environmental Science and Technology* 33, 3730- 3736.
- Shi, Q., Sakurai, H., and McMurry, P. H., 2002. Measurement of St. Louis aerosol size distributions: Observation of particle events, 21st Annual AAAR Conference, October 7 - 11, Charlotte, North Carolina.
- Sihto, S.L., Kulmala, M., Kerminen, V.M., Dal Maso, M., Petäjä, T., Riipinen, I., Korhonen, H., Arnold, F., Janson, R., Boy, M., Laaksonen, A., Lehtinen, and K.E.J., 2006. Atmospheric sulphuric acid and aerosol formation: Implications from atmospheric measurements for nucleation and early growth mechanisms. *Atmospheric Chemistry and Physics* 6, 4079- 4091.
- Sioutas, C., Delfino, R.J., and Singh, M., 2005. Exposure assessment for atmospheric ultrafine particles (UFPs) and implications in epidemiologic research. *Environmental Health Perspectives* 113 (8), 947- 955.
- Sipilä, M., Berndt, T., Petäjä, T., Brus, D., Vanhanen, J., Stratmann, F., Patokoski, J., Mauldin III, R. L., Hyvärinen, A.-P., Lihavainen, H., and Kulmala, M., 2010. The role of sulfuric acid in atmospheric nucleation. *Science* 327, 1243- 1246.
- Smith, J. N., Barsanti, K. C., Friedli, H. R., Ehn, M., Kulmala, M., Collins, D. R., ... & McMurry, P. H., 2010. Observations of ammonium salts in atmospheric nanoparticles and possible climatic implications. *Proceedings of the National Academy of Sciences*, 107(15), 6634-6639.
- Smith, J. N., Dunn, M. J., VanReken, T. M., Iida, K., Stolzenburg, M. R., McMurry, P. H., & Huey, L. G., 2008. Chemical composition of atmospheric nanoparticles formed from nucleation in Tecamac, Mexico: Evidence for an important role for organic species in nanoparticle growth. *Geophysical Research Letters*, 35(4).
- So, K. L., Guo, H., and Li, Y. S., 2007. Long-term variation of PM<sub>2.5</sub> levels and composition at rural, urban, and roadside sites in Hong Kong: Increasing impact of regional air pollution. *Atmospheric Environment* 41, 9427-9434.

- Soderholm, S. C., 1979. Diffusion Measurements of Aerosols. Thesis [PH.D.]—The University of Rochester. Source: Dissertation Abstracts International, Volume: 40-01, Section: B, page. 0304
- Sohaebuddin, S. K., Thevenot, P. T., Baker, D., Eaton, J. W., and Tang, L., 2010. Nanomaterial cytotoxicity is composition, size, and cell type dependent. *Particle and Fibre Toxicology* 7, 22.
- Solomon, P. A., Hopke, P. K., Froines, J., and Scheffe, R., 2008. Key scientific findings and policy and health-relevant insights from the U.S. Environmental Protection Agency's Particulate Matter Supersites Program and related studies: an integration and synthesis of results. *Journal of the Air & Waste Management Association* 58, S-3- S-92.
- Stanier, C.O., Khlystov, A.Y., and Pandis, S.N., 2004a. Ambient aerosol size distributions and number concentrations measured during the Pittsburgh Air Quality Study (PAQS). *Atmospheric Environment* 38 (20), 3275-3284.
- Stanier, C.O., Khlystov, A.Y., and Pandis, S.N., 2004b. Nucleation events during the Pittsburgh air quality study:description and relation to key meteorological gas phase and aerosol parameters. *Aerosol Science and Technology* 38, 253-264.
- Stölzel, M., Breitner, S., Cyrus, J., Pitz, M., Wölke, G., Kreyling, W., Heinrich, J., Wichmann, H.E., and Peters, A., 2007. Daily mortality and particulate matter in different size classes in Erfurt, Germany. *Journal of Exposure Science and Environmental Epidemiology* 17, 458-467.
- Stolzenburg, M.R., McMurry, P.H., 1991. An ultra aerosol condensation nucleus counter. *Aerosol Science and Technology* 14, 48-65.
- Thurston, G.D., Ito, K., Hayes, C.G., Bates, D.V., and Lippmann, M., 1994. Respiratory hospital admissions and summertime haze air pollution in Toronto, Ontario: consideration of the role of acid aerosols. *Environmental Research* 65, 271-290.
- Thurston, G.D., 2000. Particulate matter and sulfate: evaluation of current California air quality standards with respect to protection of children. Prepared for California Air Resources Board (CARB) and California Office of Environmental Health Hazard Assessment (OEHHA), pp. 29-36.

- Tsai, Y.I., 2005. Atmospheric visibility trends in an urban area in Taiwan 1961 -2003. *Atmospheric Environment* 39, 5555-5567.
- Tunved, P., Hansson, H.-C., Kerminen, V.-M., Ström, J., Dal Maso, M., Lihavainen, H., Viisanen, Y., Aalto, P. P., Komppula, M., and Kulmala, M., 2006. High natural aerosol loading over boreal forests. *Science* 312, 261- 263.
- U.S.EPA, 1996. Air quality for particulate matter, Vols. I, II, III, EPA/600/P-95/001aF, EPA/600/P-95/001bF, EPA/600/P-95/001cF.
- U.S.EPA, 2007. Nanotechnology White Paper. Report EPA 100/B-07/001. US Environmental Protection Agency, Washington DC 20460, USA.
- Ulrich, F., Olf, H., Stefan, R., Uwe, S., Michael, B., Ulrike, D., Ursula, K., and Irina, L., 2011. Respiratory effects of indoor particles in young children are size dependent. *Science of The Total Environment* 409, 1621-1631.
- Utell, M. J., Morrow, P. E., and Hyde, R. W., 1982. Comparison of normaland asthmatic subjects response to sulphate pollutant aerosols. *Annals of Occupational Hygiene* 26, 691- 697.
- Vakkari, V., Laakso, H., Kulmala, M., Laaksonen, A., Mabaso, D., Molefe, M., Kgabi, N., and Laakso, L., 2011. New particle formation events in semi-clean South African savannah. *Atmospheric Chemistry and Physics* 11, 3333-3346.
- Van der Hagen, M., and Järnberg, J., 2009. 140. Sulphuric, hydrochloric, nitric and phosphoric acids.
- Vehkamäki, H., Kulmala, M., Napari, I., Lehtinen, K.E.J, Timmreck, C., Noppel, M., Laaksonen, A., 2002. An improved parameterization for sulfuric acid water nucleation rates for tropospheric and stratospheric conditions. *Journal of Geophysical Research*, 107, 4622-4632.
- Vehkamäki, H., Dal Maso, M., Hussein, T., Flanagan, R., Hyvärinen, A., Lauros, J., Merikanto, P., Mönkkönen, M., Pihlatie, K., Salminen, K., Sogacheva, L., Thum, T., Ruuskanen, T. M., Keronen, P., Aalto, P. P., Hari, P., Lehtinen, K. E. J., Rannik, Ü, and Kulmala, M., 2004. Atmospheric particle formation events at Värriö measurement station in Finnish Lapland 1998-2002. *Atmospheric Chemistry and Physics* 4, 2015- 2023.

- Wahlin, P., Palmgren, F., Dingenen, R.V., 2001. Experimental studies of ultrafine particles in streets and the relationship to traffic. *Atmospheric Environment* 35, S63-S69.
- Wallace, L.A., Howard-Reed, C., 2002. Continuous monitoring of ultrafine fine and coarse particles in a residence for 18 months in 1999-2000. *Journal of the Air and Waste Management Association* 52, 828-844.
- Wallace, L.A., Ott, W., 2011. Personal exposure to ultrafine particles. *Journal of Exposure Science and Environmental Epidemiology* 21, 20-30.
- Wallace, L.A., Wang, F., Howard-Reed, C., Persily, A., 2008. Contribution of gas and electric stoves to residential ultrafine particle concentrations between 2 and 64nm: size distributions and emission and coagulation rates. *Environment Science and Technology* 42, 8641-8647.
- Waller, R.E., 1963. Acid Droplets in Town Air. *International journal of air and water pollution* 7, 733.
- Wang, S.C., Flagan, R.C., 1989. Scanning Electrical Mobility Spectrometer[M]. Division of Engineering and Applied Science California Institute of Technology Pasadena CA 91125, 138-178.
- Wang, T., Guo, H., Blake, D. R., Kwok, Y. H., Simpson, I. J., and Li, Y. S., 2005. Measurements of trace gases in the inflow of South China Sea background air and outflow of regional pollution at Tai O, southern China. *Journal of atmospheric chemistry* 52, 295-317.
- Wang, Y., Zhu, Y., Salinas, R., Ramirez, D., Karnae, S., John, K., 2008. Roadside measurements of ultrafine particles at a busy urban intersection. *Journal of the Air and Waste Management Association* 58, 1449-1457.
- Wang, Z.B., Hu, M., Yue, D.L., Zheng, J., Zhang, R.Y., Wiedensohler, A., Wu, Z.J., Nieminen, T., Boy, M., 2011. Evaluation on the role of sulfuric acid in the mechanisms of new particle formation for Beijing case. *Atmospheric Chemistry and Physics* 11, 12663-12671.
- Weber, R.J., McMurry, P.H., Mauldin, L., Tanner, D.J., Eisele, F.L., Brechtel, F.J., Kreidenweis, S.M., Kok, G. L., Schillawski, R.D., and Baumgardner, D., 1998. A study of new particle formation and growth involving biogenic and trace gas species measured during ACE1. *Journal of Geophysical Research*, 103:16385-16396,

- Weber, R., Marti, J., McMurry, P., Eisele, F., Tanner, D., and Jefferson, A., 1997. Measurements of new particle formation and ultrafine particle growth rates at a clean continental site. *Journal of Geophysical Research* 102(D4), 4375-4386.
- Weber, R.J., McMurry, P.H., Mauldin, R.L., Tanner, D.J., Eisele, F.L., Clarke, A.D., and Kapustin, V.N., 1999. New particle formation in the remote troposphere: A comparison of observations at various sites. *Geophysical Research Letters* 26, 307-310.
- Weber, R.J., Moore, K., Kapustin, V., Clarke, A., Mauldin, R. L., Kosciuch, E., Cantrell, C., Eisele, F., Anderson, B., and Thornhill, L., 2001. Nucleation in the equatorial Pacific during PEM-Tropics B: enhanced boundary layer H<sub>2</sub>SO<sub>4</sub> with no particle production, *Journal of Geophysical Research—Atmospheres* 106 (D23), 32767- 32776.
- Wehner, B., Birmili, W., et al., 2002. Particle number size distributions in a street canyon and their transformation into the urban-air background: measurements and a simple model study. *Atmospheric Environment* 36 (13), 2215- 2223.
- Wehner, B., Philippin, S., Wiedensohler, A., Scheer, V., and Vogt, R., 2004. Variability of non-volatile fractions of atmospheric aerosol particles with traffic influence. *Atmospheric Environment* 38, 6081-6090.
- Wehner, B., Uhrner, U., von Löwis, S., Zallinger, M., and Wiedensohler, A., 2009. Aerosol number size distributions within the exhaust plume of a diesel and a gasoline passenger car under on-road conditions and determination of emission factors. *Atmospheric Environment* 43, 1235-1245.
- Westerdahl, D., Wang, X., Pan, X., and Zhang, K., 2009. Characterization of on-road vehicle emission factors and microenvironmental air quality in Beijing, China. *Atmospheric Environment* 43, 697-705.
- Wichmann, H. E., Spix, C., Tuch, T., Wolke, G., Peters, A., Heinrich, J., Kreyling, W.G., and Heyder, J., 2000. Daily mortality and fine and ultrafine particles in erfurt, Germany Part I: role of particle number and particle mass. *Health Effects Institute* 98, 5- 86.
- Wiedensohler, A., Chen, Y. F., Nowak, A., et al., 2009. Rapid aerosol particle growth and increase of cloud condensation nucleus activity by

- secondary aerosol formation and condensation: A case study for regional air pollution in northeastern China. *Journal of Geophysical Research*, 114 D00G08.
- Wiedensohler, A., Lütke-meier, E., Feldpausch, M., Helsper, C., 1986. Investigation of the bipolar charge distribution at various gas conditions. *Journal of Aerosol Science* 17, 413-416.
- Woo, K. S., Chen, D. R., Pui, D. Y. H., and McMurry, P. H., 2001. Measurement of Atlanta aerosol size distributions: Observations of ultrafine particle events. *Aerosol Science and Technology* 34(1), 75- 87.
- Wright, M., Fewes, A., Keitch, P., and Henshaw, D., 2007. Small-ion and nano-aerosol production during candle burning size and concentration profile with time. *Aerosol Science and Technology* 41, 475-484.
- Wu, Z. J., Hu, M., Lin, P., Liu, S., Wehner, B., and Wiedensohler, A., 2008. Particle number size distribution in the urban atmosphere of Beijing, China. *Atmospheric Environment* 42, 7967- 7980.
- Wyzga, R. E., and Folinsbee, L. J., 1995. Health effects of acid aerosols. *Water, Air, and Soil Pollution* 85,177-188.
- Xia, L.P., and Shao, Y. P., 2005. Modelling of traffic flow and air pollution emission with application to Hong Kong Island. *Environmental Modelling & Software* 20, 1175-1188.
- Yang, K. M., Chung, J. Y., Hsieh, M. F., and Lin, D. S., 2007. Apparent Topographic Height Variations Measured by Noncontact Atomic Force Microscopy. *Japanese Journal of Applied Physics* 46, 4395.
- Yang, W.H., Lee, Y.C., Zwang, F.C., and Don, S.C., 2001. Investigation of waste gas pollution from joss paper incineration and the associated pollution control, Published by the Bureau of Citizen Affair Management, Taipei City Government, Taiwan.
- Yao, X.H, Lau, N.T, Fang, M., and Chan, C.K., 2005. Real-time observation of the transformation of ultrafine atmospheric particle modes. *Aerosol Science and Technology* 39, 831-841.
- Yao, X.H., Ling, T.Y., Fang, M., and Chan, C.K., 2007. Size dependence of in situ pH in submicron atmospheric particles in Hong Kong. *Atmospheric Environment* 41, 382-393.

- Yao, X., Choi, M. Y., Lau, N. T., Arthur Lau, P.S., Chan, C.K., and Fang, M., 2010. Growth and shrinkage of new particles in the atmosphere in Hong Kong, *Aerosol Science and Technology* 44, 639-650
- Yli-Juuti, T., Nieminen, T., Hirsikko, A., Aalto, P. P., Asmi, E., Hörrak, U., Manninen, H. E., Patokoski, J., Dal Maso, M., Petäjä, T., Rinne, J., Kulmala, M., and Riipinen, I., 2011. Growth rates of nucleation mode particles in Hyytiälä during 2003- 2009: variation with particle size, season, data analysis method and ambient conditions. *Atmospheric Chemistry and Physics* 11, 12865- 12886.
- Yu, F.Q., 2010. Ion-mediated nucleation in the atmosphere: Key controlling parameters, implications, and look-up table. *Journal of Geophysical Research* 115, D03206, doi:10.1029/2009JD012630.
- Yue, D. L., Hu, M., Wu, Z. J., Wang, Z. B., Guo, S., Wehner, B., Nowak, A., Achtert, P., Wiedensohler, A., Jung, J. S., Kim, Y. J., and Liu, S. H., 2009. Characteristics of aerosol size distributions and new particle formation in the summer in Beijing. *Journal of Geophysical Research* 114, D00G12.
- Zelikoff, J. T., Frampton, M. W., Morrow, M. D. C. P. E., Sisco, M., Tsai, Y., Utell, M. J., and Schlesinger, R. B., 1997. Effects of inhaled sulfuric acid aerosols on pulmonary immunocompetence: A comparative study in humans and animals. *Inhalation Toxicology* 9(8), 731-752.
- Zhang, K.M., and Wexler, A.S., 2002. A hypothesis for condensation of fresh atmospheric nuclei. *Journal of Geophysical Research* 107 D21:4577.
- Zhang, Q., Stanier, C.O., Canagaratna, M.R., Jayne, J.T., Worsnop, D.R., Pandis, S.N., Jimenez, J.L., 2004a. Insights into chemistry of nucleation bursts and new particle growth events in Pittsburgh based on aerosol mass spectrometry. *Environmental Science and Technology* 38, 4797-4809.
- Zhang, R., Suh, I., Zhao, J., Zhang, D., Fortner, E. C., Tie, X., Molina, L. T., and Molina, M. J., 2004b. Atmospheric new particle formation enhanced by organic acids. *Science* 304, 1487-1490.
- Zhang, R.Y., Alexei, F.K., Joakim, P., Zhang, D., Xue, H.X., McMurry, P.H., 2008. Variability in morphology hygroscopicity and optical properties of soot aerosols during atmospheric processing. *Proceedings of the National Academy of Sciences* 30, 10291-10296.

- Zhang, Q. F., and Zhu, Y. F., 2010. Measurements of ultrafine particles and other vehicular pollutants inside school buses in South Texas. *Atmospheric Environment* 44:253-261.
- Zhang, R., Khalizov, A., Wang, L., Hu, M., and Xu, W. (2011). Nucleation and growth of nanoparticles in the atmosphere. *Chemical Reviews*, 112(3), 1957-2011
- Zhu, Y., Fung, D. C., Kennedy, N., Hinds, W.C., and Eiguran-Fernandez, A., 2008. Measurements of ultrafine particles and other vehicular pollutants inside a mobile exposure system on Los Angeles freeways. *Journal of the Air & Waste Management Association* 58(3), 424- 434.